ENHANCEMENT OF ROLL MANEUVERABILITY USING POST-REVERSAL DESIGN

A Thesis
Presented to
The Academic Faculty

by

Wei-En Li

In Partial Fulfillment
of the Requirement for the Degree
Doctor of Philosophy in the
School of Aerospace Engineering

Georgia Institute of Technology
August 2009

ENHANCEMENT OF ROLL MANEUVERABILITY USING POST-REVERSAL DESIGN

Approved by:

Professor Dewey H. Hodges, Advisor
Committee Chair
School of Aerospace Engineering
Georgia Institute of Technology

Professor J. V. R. Prasad
School of Aerospace Engineering
Georgia Institute of Technology

Professor Olivier A. Bauchau
School of Aerospace Engineering
Georgia Institute of Technology

Professor David M. Goldsman
School of Industrial and Systems Engineering
Georgia Institute of Technology

Professor Marilyn J. Smith
School of Aerospace Engineering
Georgia Institute of Technology

Date Approved: June 18, 2009

To my parents and my elder sister and brother

ACKNOWLEDGEMENTS

I would like to express my greatest appreciation to all who have given me assists while I was studying here.

First and the most, I would like to express my sincere gratitude to my advisor, Professor Dewey H. Hodges, for his continuous support and invaluable guidance ever since I came to Georgia Institute of Technology. No matter how many questions I asked him, he was always willing to give me direction, even explaining the details for me. Without his assistance, I would never be able to complete this research. I really learned a lot under Dr. Hodges' supervision, and will never forget the work experiences with him.

Next, I would like to thank Professor Olivier A. Bauchau. He always treated me friendly and showed his enthusiasm to help me on my research. His fantastic teaching gave me a shock when I first learned a course in a foreign country, so I always enjoyed his lecture pretty much.

Also, I am grateful to Professor Marilyn J. Smith for her unselfish help. Her systematic and brilliant way of thinking has influenced me a lot. She impressed me with her great ideas and provided a wealth of knowledge relevant to this dissertation.

Special thanks to Professor J. V. R. Prasad and Professor David Goldsman for being my thesis committee members and helping me to improve my dissertation with their valuable advice and suggestions.

I would also like to show my deep appreciation to Dr. Jieun Ku, who taught me ANSYS and VABS, Dr. Jielong Wang, Dr. Haiying Liu, Changkuan Ju, and Afifa A. Zaki, who assisted me to learn DYMORE, and Jimmy Ho, who spent lots of time discussing my research with me and made me get more familiar with XFOIL. Without their

generous helps and knowledgeable comments, I would not have been able to complete this work.

Thanks to Dr. Chang-Yong Lee, Dr. Samer A. Tawfik, Dr. Chongseok Chang, Dr. Leihong Li, Huimin Song for their friendship to share their knowledge and time in enlightening discussion during the graduate study.

I am also grateful to my dear friends, Yu-Yun Tsai, Chi-Ti Hsieh, Chih-Ching Chiou, Chien-Chun Liu, Shu-Chen Chiang, Shang-Feng Yang, and Daniel Miau, who gave me strongest support and took care of me since I came to US. You made my life colorful when I studied here. I am so lucky to know you all.

Lastly and most of all, I am extremely grateful to my family who always cheer me up during hard times. Without your lovely support, I could not even come to study here. You know my dream for studying abroad, and that are you who make my dream come true. Thanks! One day I will let you be proud of me!

Good research always opens the door for others to do more research.

Dr. Dewey H. Hodges

TABLE OF CONTENTS

LIST OF TABLES

LIST OF FIGURES

NOMENCLATURE

Symbol

a	lift-curve slope
a_j^r	induced inflow expansion coefficients
b	airfoil semichord
b_j^r	induced inflow expansion coefficients
c	chord
c_d	sectional drag coefficient
c_l	sectional lift coefficient
c_{l_α}	linear sectional lift-curve slope
c_{l_β}	linear sectional lift-curve slope with respect to aileron deflection
c_m	sectional moment coefficient
c_{m_0}	sectional cambered moment coefficient
$c_{m_{ac}}$	sectional moment coefficient at aerodynamic center
c_{m_β}	linear sectional moment-curve slope with respect to aileron deflection
d	number of semichords flap hinge lies aft of midchord
e	offset of elastic axis to aerodynamic center
h	motion of reference point in Theodorsen theory
j	polynomial number
k	rotational spring constant
l	wingspan

m	sectional mass
n	expansion index
n_s	factor of safety
p	roll rate
q	dynamic pressure
$\bar{q}$	nondimensional dynamic pressure
q_D	divergence dynamic pressure
q_R	reversal dynamic pressure
r	effective moment arm
$\bar{r}$	blade radial coordinate nondimensionalized on rotor radius
s	offset of shear center to elastic axis
t	airfoil thickness
$\bar{t}$	nondimensional time
w	normal component of induced inflow, positive downward
x, y, z	local axis system of the wing
AR	aspect ratio
C_L	lift coefficient
C_{L_α}	linear lift-curve slope with respect to angle of attack
C_{L_β}	linear lift-curve slope with respect to aileron deflection
C_{M_β}	moment-curve slope with respect to aileron deflection
D	drag
EI	bending stiffness
G	the ratio of the force on an object to its weight

GJ	torsional stiffness
I	mass moment of inertial
K	bending-torsion coupling stiffness
L	lift
$\overline{L}$	nondimensional total lift
L_a	generalized airloads for aileron
L_b	length of bracket
L_c	generalized airloads for leading-edge control surface
L_n	generalized airloads
L_{rigid}	total lift for rigid wing
L_{span}	length of wingspan
L_{total}	total lift
L_W	generalized airloads for main wing
M	moment
M^e	rolling moment caused by elastic twist
M^p	rolling moment caused by roll rate
M^β	rolling moment caused by aileron deflection
M_a	generalized pitching moment for aileron
M_{ac}	moment about the aerodynamic center
M_c	generalized pitching moment for leading-edge control surface
M_r	rolling-moment of a flying aircraft
M_x	rolling-moment of a flying aircraft
M_y	pitching-moment of a flying aircraft

M_z	yawing-moment of a flying aircraft
M_∞	freestream Mach number
$M_{elastic}$	bending moment of the root for elastic wing
M_{rigid}	bending moment of the root for rigid wing
M_W	generalized pitching moment for main wing
R_e	Reynolds number
S	planform area
T	twisting moment
U	freestream velocity
U_n	Chebyshev polynomials of second kind
V_∞	freestream speed
subscript *1,2,3*	local axis system of the wing
subscript *f*	parameters for trailing-edge flap
α	angle of attack
α_0	zero lift angle of attack
α_r	rigid angle of attack
$\overline{\alpha}_r$	nondimensional rigid angle of attack
β	aileron deflecting angle
β_a	mean magnitude of the two ailerons' deflection for a rolling aircraft
β_p	Prandtl-Glauert compressibility correction factor, $\beta_p = \sqrt{1 - M_\infty^2}$
γ	shear strain
γ_b	bound vorticity on airfoil
η	aileron effectiveness

θ	elastic twist
κ	nondimensional bending-torsion coupling stiffness
κ_1, κ_2	generalized strains
λ	induced flow due to other vorticity
μ	viscosity
ν	induced flow to the shed wake
ξ	dummy integration variable
ρ	air density
φ	control surface deflecting angle
ψ	azimuthal location of reference blade
Γ	total bound vorticity
$\Psi_j^r(\bar{r})$	general expansion functions
ΔP	pressure differebce across airfoil

Abbreviation

deg	degree
AAW	active aeroelastic wing
AFW	Active flexible wing
CFD	computational fluid dynamics
NACA	National Advisory Committee for Aeronautics

SUMMARY

This dissertation consists of three main parts. The first part is to discuss aileron reversal problem for a typical section with linear aerodynamic and structural analysis. The result gives some insight and ideas for this aeroelastic problem. Although the aileron in its post-reversal state will work the opposite of its design, this type of phenomenon as a design root should not be ruled out on these grounds alone, as current active flight-control systems can compensate for this. Moreover, one can get considerably more (negative) lift for positive flap angle in this unusual regime than positive lift for positive flap angle in the more conventional setting. This may have important implications for development of highly maneuverable aircraft.

The second part is to involve the nonlinear aerodynamic and structural analyses into the aileron reversal problem. Two models, a uniform cantilevered lifting surface and a rolling aircraft with rectangular wings, are investigated here. Both models have trailing-edge control surfaces attached to the main wings. A configuration that reverses at a relatively low dynamic pressure and flies with the enhanced controls at a higher level of effectiveness is demonstrated. To evaluate how reliable for the data from XFOIL, the data for the wing-aileron system from advanced CFD codes and experiment are used to compare with that from XFOIL.

To enhance rolling maneuverability for an aircraft, the third part is to search for the optimal configuration during the post-reversal regime from a design point of view. Aspect ratio, hinge location, airfoil dimension, inner structure of wing section, composite skin, aeroelastic tailoring, and airfoil selection are investigated for cantilevered wing and rolling aircraft models, respectively. Based on these parametric structural designs as well

as the aerodynamic characteristics of different airfoils, recommendations are given to expand AAW flight program.

CHAPTER I

INTRODUCTION

1.1 Motivation

The concept of using the post-reversal regime to enhance the roll performance of wings operating at high dynamic pressure is proposed. The notion of getting higher lift from a reversed control surface is not new. In the helicopter industry, there is one category of main rotor pitch control called “active servo flaps,” where auxiliary airfoil sections located after of the trailing edge of the main blades as adopted by Kaman [65, 114]. The Kaman servo-flap rotor is designed to operate in the post-reversal regime in order to greatly increase the effectiveness of the trailing-edge flap. Of course, for the helicopter application there is no problem with having to control the blade at the point of reversal since that occurs at a lower rotor angular speed when the aircraft is still on the ground. At the University of Maryland, much work has been devoted to the development of smart trailing-edge flaps to improve rotor performance [15, 59, 60, 63, 113]. Also, many researchers have employed active-control and smart-material concepts to investigate aeroelastic problems for rotors with trailing-edge flaps in the early 2000’s [41, 107, 108].

The only fixed-wing application known to date is the Active Aeroelastic Wing (AAW) program, which indeed intended to address this design concept. The idea of AAW technology initially came from Rockwell International Corporation’s concept named the Active Flexible Wing (AFW). In the early 1980's, multi-point tactical fighter aircraft designs were being developed by design teams for Advanced Tactical Fighter (ATF)

program proposals. During this period, the Active Flexible Wing concept was originated to solve the aeroelastic control reversal problem inherent at several design points including the subsonic, transonic, and supersonic regimes [87, 116, 117]. Rockwell conducted a conceptual design study which applied the concept of AFW to an ATF class, supersonic cruise fighter. The concept exploited wing flexibility to provide weight savings and improved aerodynamic performance. Weight savings were realized via a flexible wing and no horizontal tail. In an AFW wing design, large amounts of aeroelastic twist provide improved maneuver aerodynamics at several design points. However, degraded roll performance (in the form of aileron reversal) over a significant portion of the flight envelope is a direct result of large amounts of twist in the wing. In a typical aircraft design, a differential horizontal tail control would be added to provide acceptable roll performance. Instead of this, in an AFW design, multiple leading- and trailing-edge wing control surfaces are used in various combinations [3], up to and beyond reversal, to provide enhanced roll performance. Although AAW/AFW Technology has been demonstrated through analysis and wind tunnel modeling in the early 1990's, an application of the technology in full scale flight utilizing a current high performance jet fighter is required to mature the basic technology and provide aircraft designers with the confidence to use the technology in future designs. Full scale flight is required to achieve the necessary values of Reynolds numbers, high angles of attack, and high *G* maneuvering effects. Full-scale flight is also required to demonstrate the effectiveness of AAW Technology to the flight vehicle users.

During 1995, a flight research initiative was established to flight test some of the fundamental aspects of AAW Technology [86]. With this initiative, the process had begun to define detailed requirements, available flight approaches, and suitable flight

vehicles to host AAW research. Since the goal of this program was to generate full scale flight data that demonstrates and measures the physics of AAW in a low cost, effective manner, the aircraft candidates which appear to have the best cost/benefit combination in terms of modification, operation, and potential for research data were the current military light weight fighter aircraft. The F-16 and the F/A-18 were chosen as host aircraft for AAW technology, as both of them have supersonic capability and wing planforms and control surfaces which appear amenable to a modification to permit an AAW flight experiment. In the late 1990's, AAW modification design studies had been conducted to identify potential modifications to both the F/A-18 and the F-16 that make each of these aircraft suitable as AAW research testbeds. The major one of the candidate aircraft testbeds is F/A-18, and its wing has an aspect ratio of 4.0. The aileron's horizontal hinge for F/A-18 is located at 75% chord, and the main wing has 13.25-foot chord at the wing root and 5.51-foot chord at the wing tip.

The above studies also identified the AAW characteristics that could be flight tested using these aircraft and the costs of aircraft modification, flight planning and testing. However, it was unable to achieve its objective because the wing stalled before it would actually reverse. Another mitigating factor was that it relied on a retrofit to an existing aircraft rather than an optimized design from scratch. Also, it should be noted that there were leading-edge control devices to make certain the wing was never without the means to be controlled while reversal occurred.

The main shortcoming of AAW flight research program can be overcome by abandoning the linear analysis methodology. Instead, a program is proposed to investigate post-reversal behavior of high-aspect-ratio wings with geometrically-exact structural nonlinearities [37, 80, 82, 83, 84] and an appropriate level of aerodynamic

nonlinearities [30, 58, 104]. This should go a long way toward definitively answering the question of whether or not the objective of improving roll performance can be achieved. The starting point would be the simplest case: a high-aspect-ratio cantilevered wing modeled with geometrically-exact composite beam theory (Hodges 2006) [46] and a static stall model for the aerodynamics [72, 95]. To fully describe the aerodynamic characteristics of an airfoil, both pre-stall and post-stall regime need to be considered [75, 88]. In addition, the approaches need to be incorporated with the stall model for the wing with trailing-edge control surfaces [26, 27]. If there is a configuration that reverses at a relatively low dynamic pressure and flies with the enhanced (though backward) controls at a higher level of effectiveness than can be achieved in with the conventional sign of controls, the attention will be turned to (a) beefing up the aerodynamic model, say building up a full range of look-up table by using a panel method code (XFOIL); and (b) studying the optimal design by varying some specific structural parameters to improve the effectiveness. The nonlinearities are important [9, 29, 76, 81] because stall was recorded as having taken place. To achieve angles of attack sufficiently large to have stall, large deflections need also to be included.

1.2 Reviews of Previous Work

Rolling maneuvers for aircraft are conventionally performed by deflecting the trailing-edge control surfaces of the wings antisymmetrically, which means increasing lift on one wing while decreasing lift on the other. This is an effective technique for the generation of rolling moment for an aircraft operating in a low dynamic pressure environment where the wings are essentially “rigid”. However, during the rolling

maneuver at high dynamic pressure where the deformation of the wing is significant, the flap angle, β, by deflecting control surface on a flexible wing changes the effective camber which induces a nose-down pitching moment, that twists the wing nose down and tends to decrease lift and in turn reduce the roll rate of the aircraft. As dynamic pressure increases, a point is reached where roll reversal occurs.

One way to improve the roll performance of the aircraft is to maximize the aileron reversal dynamic pressure. This corresponds to maximize the speed at which the aileron ceases to provide additional lift. Gomes and Suleman [42] tried to maximize the aileron reversal speed of a wing torsion box by reinforcing its upper skin. Chen et al. [24] optimized the roll rate by replacing the existing wing spars with an adaptive-structure. Rather than the traditional stiffening of wings to avoid encountering the roll reversal dynamic pressure, wing flexibility was used as an asset rather than an impediment to be overcome. Khot, Eastep, Kolonay [52, 53], and Appa [51] examined the technique for augmenting the aileron to increase the roll rate of a high performance aircraft at high dynamic pressures for enhancement of the rolling maneuver. The flexible wing was re-twisted and re-cambered to counteract the detrimental twisting moment produced by the aileron rotation to achieve recovery of rolling moment lost by the detrimental twisting in a high dynamic pressure environment. A method for prescribing the antisymmetric wing twists and camber distribution by reversing the twist and camber resulting from the use of aileron only was described. Rather than using an aileron system to achieve an aerodynamic rolling moment, Khot et al. [50, 54, 55, 56] used elastic wing twist and camber to achieve a specified roll rate at all dynamic pressures. The elastic twist and camber is achieved by providing a system of actuating elements distributed within the internal substructure of the wing to provide control forces. The modal approach was used

to develop equilibrium equations for the steady roll maneuver of a wing subjected to aerodynamic loads and actuating forces.

One of the main elements of the flexible wing concept is rolling moment control achieved by the elastic wing twist and camber. This has been investigated previously with an internal actuation scheme [7, 8, 44, 61, 103], multiple external aerodynamic control surfaces [73, 74], and strain actuated adaptive wings [14, 43, 62]. The internal actuation scheme of the mission adaptive wing did achieve aerodynamic benefits through contoured control surface deformation, but the complexity and weight penalty of the actuation system rendered the design impractical. The active flexible wing technique using multiple control surfaces does achieve the proper elastic wing twist for the required rolling moment and results in a decrease of structural weight by relaxing wing stiffness requirements, but the potential for an aerodynamic penalty exists. Recent developments in smart materials for controlling aircraft structural deformation make it possible to achieve the proper elastic wing twist for control of roll, but large actuation strains are required for aeroelastic control of realistic wings.

The use of multiple control surfaces to affect roll trim of aircraft was investigated by Andersen, Forster, Kolonay, and Eastep [3]. Their work gave deeper insights into the favorable synergy that can be created by a combination of leading- and trailing-edge controls. They noted that the unfavorable aeroelastic twist that can lead to trailing-edge control surface reversal can be offset by a leading-edge control surface. In their work, the finite element method was used to calculate structural deformation caused by steady aerodynamic input forces, which were generated by a linear panel method. Values of control surface effectiveness, calculated from the flexible rolling moment stability derivatives, were used to determine which control surfaces are most effective in

achieving a desired roll maneuver. The roll trim equation of motion was solved for multiple control surface deflections using an iterative technique that minimizes the control effort to achieve a specified roll rate. The results showed that utilization of leading-edge control surfaces can be effectively employed to affect aircraft trim across a wide range of dynamic pressures. Roll trim can be achieved using multiple control surfaces with smaller deflections than those needed with only a single surface. Work then followed by Dowell, Bliss, and Clark [28], was illustrated the concept of the favorable effect of a leading-edge control surface by an appropriate choice of the ratio of leading- to trailing-edge control surface rotations. This work was based on two simple models, an airfoil and a flexible wing of a rolling aircraft. Furthermore, Tang, Li, and Dowell [110, 111] built up an experimental rolling wing-fuselage model for wing tunnel test to assess the above theoretical results.

The concept of using the post-reversal regime to enhance the roll performance of wings operating at high dynamic pressure had been assessed in the Active Aeroelastic Wing program. AAW was intended to take use of wing flexibility to enhance the rolling maneuverability of aircrafts, but parts of the analyses are limited to be linear. Active Aeroelastic Wing Technology is a multidisciplinary, synergistic technology that integrates air vehicle aerodynamics, active control, and structures advanced technology together to maximize air vehicle performance. The technology uses wing aeroelastic flexibility for a net benefit and takes advantage of high aspect ratio, thin, swept fighter wings that are aeroelastically deformed into shapes for optimum performance. Many designers contributed to the applications of AAW technology. Mavris, Flick, and Love [70] incorporated multidisciplinary design optimization and response surface methods to characterize wing weight as a function of wing geometry. Zink et al. [119, 120]

demonstrated a process by which some of the benefits associated with AAW technology can be quantified over the wing geometry design space, so that future conceptual designers may make the best use of this technology. Boehm et al. [18] conducted a series of analyses to determine the effect of deflections of individual control surfaces on rolling moment, hinge moments, aeroelastic twist distribution, and shear, bending, and torsion load distribution for each of the anticipated flight research conditions. Their results are part of a complete set of linear aeroelastic response predictions of the AAW flight research vehicle. This effort had helped to identify specific cases to be studied with higher fidelity analysis methods, and the data is being used to help guide the wind tunnel and flight test portions of the AAW program. Ultimately, the correlated data from analyses, wind tunnel tests, and flight tests will serve as a reference for designers in future applications of AAW. In addition, recent work by Yurkovich [118] showed that aileron reversal and control surface effectiveness can be affected by suitably determining the size and location of the wing control surfaces. His study demonstrated the analytical process that was used to integrate AAW technology into a variable area, co-planar wing, morphing aircraft. However, the AAW flight research program was unable to achieve its objective because the wing stalled before it would actually reverse [45, 85, 107, 112]. Research between 1995 and 2005 on the Active Aeroelastic Wing by the Air Force and NASA has reported difficulties achieving reversal for the configuration under consideration. Flow separation brought on by high effective camber is evidently a factor. Another mitigating factor was that it relied on a retrofit to an existing aircraft rather than the detail analyses and the optimized design from scratch. Also, it should be noted that there were leading-edge control devices to make certain the wing was never without the means to be controlled. Finally, there is no published work discussing this issue with

aerodynamic and structural nonlinearities.

1.3 Objective

The main idea for this research comes from AAW flight program. This Program tried to design the aircraft to operate during post-reversal regime. Although the aileron will now work the opposite of the usual way at most of the operational speeds of the aircraft, this type of design can make the aircraft get considerably more (negative) lift for positive flap angle in this unusual regime than positive lift for positive flap angle in the more conventional setting. This may have important implications for development of highly maneuverable aircraft. Unfortunately, it was unable to achieve its objective because the wing stalled before it would actually reverse for some conditions. The primary objective of the present work is to demonstrate that a configuration that reverses at a relatively low dynamic pressure and flies with the enhanced controls at a higher level of effectiveness than can be achieved with the conventional sign of controls does indeed exist. The second objective is to search for a configuration in the post-reversal regime that enhances roll maneuverability from design point of view. Although the models here is not approaching the completeness for AAW flight program, the conclusions should be able to shed some light on the AAW flight program based on a systematic investigation of the relevant variables.

1.4 Present Approach

First of all, an introduction to aileron reversal for a typical section with linear

aerodynamic and structural analysis is given in Chapter 2. The result gives some insight and ideas for this aeroelastic problem. The next step is to involve the nonlinear aerodynamic and structural analyses into the aileron reversal problem. Chapter 3 introduces the tools used for the nonlinear analyses herein. Then in Chapter 4, two models, lifting surface and rolling aircraft, are investigated through DYMORE, which is a finite element based tool for analysis of nonlinear flexible multibody systems. After identifying a configuration that reverses at a relatively low dynamic pressure and flies with the enhanced controls at a higher level of effectiveness than can be achieved with the conventional sign of controls, more advanced aerodynamic models are used to investigate it. Next, Chapter 5 compared and verified the results between different aerodynamic models for some specific cases to make certain the models and results are reliable. To enhance rolling maneuverability for an aircraft, the last and most important step is to search for the better configuration during the post-reversal regime from design point of view. Some parametric designs are taken in Chapter 6, that include aspect ratio, hinge locations, airfoil dimension, wing section inner design, composite skin, aeroelactic tailoring, and airfoil selection. The aileron effectiveness is defined as how much rolling moment can be generated for the cantilevered wing model and how much roll rate can be generated for the rolling aircraft model, respectively. Comparisons are made between these design parameters to discuss the possibilities of enhancing rolling maneuverability for an aircraft.

CHAPTER II

LINEAR ANALYSIS FOR AILERON REVERSAL

2.1 System Model

Usually people address roll performance in terms of aileron reversal. Therefore, the problem of aileron reversal for the wind-tunnel type models is considered in [47]. Most of equations and figures here are taken from Ref. [47] with permission. An airfoil equipped with an aileron can get additional lift from deflecting the aileron downwards. However, the flow on the aileron also generates a moment that tends to pitch the airfoil nose down. If the support allows this nose-down pitch, then lift is reduced. For this reason the torsional flexibility of an elastic wing causes a similar reduction in lift. At high speeds, the former effect, a positive and purely aerodynamic lift, may be overpowered by the latter, a negative and aeroelastic lift. This loss of aileron effectiveness is a consequence of the elastic properties of the wing and is dependent on the flight condition. The primary danger posed by the loss of control effectiveness is that the pilot cannot control the aircraft in the usual way. There are additional concerns for aircraft, the missions of which depend on their being highly maneuverable. For example, when control effectiveness is lost, the pilot of a fighter aircraft may not be able to count on the aircraft's ability to avoid destruction by a missile. The phenomenon about the loss of control effectiveness and eventual reversal is discussed.

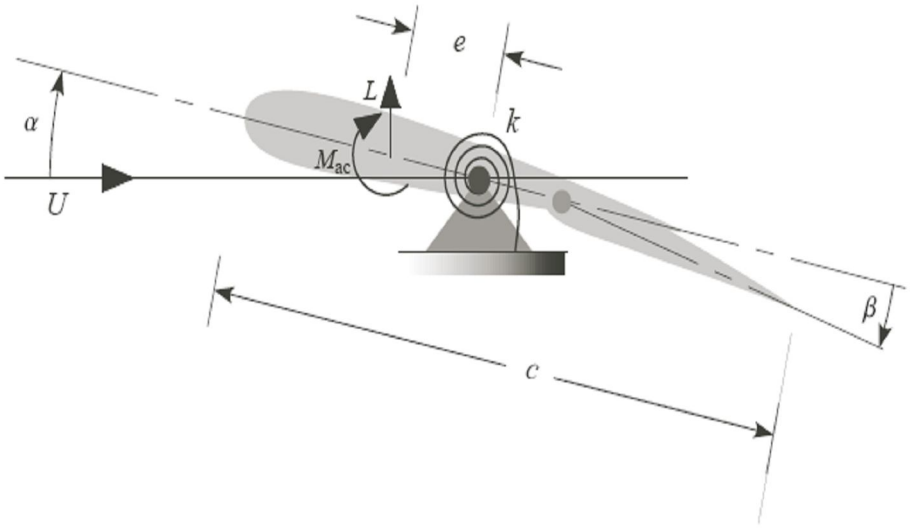

Figure 2.1: Two-dimensional typical section with aileron in a wind tunnel quoted from Ref. [47]

To this end, consider the typical airfoil section with a trailing-edge flap, shown in Figure 2.1. The wing is pivoted and restrained by a rotational spring with spring constant k, and the aileron deflection angle β can be arbitrarily set by the flight control system. The chord of this section is denoted by c, and e represents the distance between the aerodynamic center and the pivot. With the freestream velocity, U, suppose the model has angle of attack, α, aerodynamic lift, L, at the aerodynamic center and moment, M_{ac}, about the aerodynamic center. Now one may write equations of equilibrium for the system.

2.2 Theoretical Derivation

Suppose the pivot is the locus of the center of gravity, then gravity can be neglected to illustrate this phenomenon, and the weight is not shown in the figure. Moment

equilibrium for this system about the pivot requires that

$$M_{ac} + eL = k\theta \tag{1}$$

If the support is rigid, the angle of attack will be α_r, which is referred to as the rigid angle of attack and is positive nose-up. The elastic pitch angle is denoted by θ, which is also positive nose-up. Thus, the total angle of attack is

$$\alpha = \alpha_r + \theta \tag{2}$$

The lift and pitching moment for a two-dimensional wing can be written as

$$\begin{aligned} L &= q_\infty S c_l \\ M_{ac} &= q_\infty c S c_{m_{ac}} \end{aligned} \tag{3}$$

which S is the planform area. For a given flap angle ($\beta \neq 0$), the effective camber of the airfoil changes, and both lift and pitching moment change in turn. For a linear theory, both α and β should be small angles, so that

$$\begin{aligned} c_l &= c_{l_\alpha}\alpha + c_{l_\beta}\beta \\ c_{m_{ac}} &= c_{m_0} + c_{m_\beta}\beta \end{aligned} \tag{4}$$

Assume a symmetric airfoil, so that $c_{m_0} = 0$; $c_{m_\beta} < 0$ because of the nose-down pitching moment due to positive flap angles (deflecting downwards).

Substituting Eqns. (3) into Eqn. (1) and making use of Eqns. (2) and (4), θ will be

$$\theta = \frac{qS\left[ec_{l_\alpha}\alpha_r + \left(ec_{l_\beta} + cc_{m_\beta}\right)\beta\right]}{k - eqSc_{l_\alpha}} \tag{5}$$

Because of the support flexibility in pitch (represented here by the rotational spring), θ is a function of β. Substituting Eqn. (5) back into Eqns. (3) and (4), one obtains an expression for the aeroelastic lift

$$\overline{L} = \frac{L_{total}}{L_{rigid}} = \frac{\left[1 + \frac{c_{l_\beta}\beta}{c_{l_\alpha}\alpha_r}\left(1 + \frac{cqSc_{l_\alpha}c_{m_\beta}}{kc_{l_\beta}}\right)\right]}{1 - \frac{eqSc_{l_\alpha}}{k}} \tag{6}$$

The lift is a function of β in two counteracting ways from the two terms in the coefficient of β. Ignoring the effect of the denominator for the time being, the first term in the numerator that multiplies β is purely aerodynamic and leads to an increase in lift with β, because of a change in the effective camber. The second term is aeroelastic. Because of $c_{m_\beta} < 0$, as β is increased, the effective change in the camber also induces a nose-down pitching moment that, due to the flexibility of the support, tends to decrease θ. Consequently, the net lift generation is decreased. At low speed, the purely aerodynamic increase in lift is larger than the aeroelastic decrease in lift, so that the lift indeed increases with β. However, as dynamic pressure increases, the aeroelastic effect becomes stronger; and there is a point at which the net rate of change of lift with respect to β vanishes so that

$$\frac{\partial L}{\partial \beta} = 0 \tag{7}$$

Thus, the dynamic pressure at which the reversal occurs is

$$q_R = -\frac{kc_{l_\beta}}{cSc_{l_\alpha}c_{m_\beta}} \tag{8}$$

Obviously, a stiffer k gives a higher reversal speed, and a torsionally rigid wing will not undergo reversal. For dynamic pressures above q_R (but still below the divergence dynamic pressure), a positive flap angle will actually decrease the lift.

Note that the dynamic pressure at which divergence occurs can be found by setting the denominator of Eqn. (6) equal to zero, which yields

$$q_D = \frac{k}{eSc_{l_\alpha}} \tag{9}$$

A positive β could increase the lift, decrease the lift, or not change the lift at all, depending on the flight condition. The aileron lift effectiveness, η, can be thought of as the aeroelastic change in lift per unit change in β divided by the change in lift per unit change in β that would result are the airfoil not allowed to pitch; that is,

$$\eta = \frac{\dfrac{\partial L}{\partial \beta}_{elastic}}{\dfrac{\partial L}{\partial \beta}_{rigid}} \tag{10}$$

Using the above, the aileron lift effectiveness is

$$\eta = \frac{1 - \dfrac{q}{q_R}}{1 - \dfrac{q}{q_D}} \tag{11}$$

which implies that the airfoil will remain divergence-free, and control effectiveness will not be lost as long as $q < q_D \leq q_R$. Obviously, if the support are rigid, both q_D and q_R become infinite and $\eta = 1$. The model's physical and geometric features have clear implications for elastic wings.

Thinking unconventionally for the moment, supposing that $q_R << q_D$, this will result in aileron reversal at a low speed. Although the aileron will disobey the usual way at most of the operational speeds of the aircraft, this type of design should not be ruled out on these grounds alone. Active flight-control systems can certainly compensate for this. Moreover, one can get considerably more lift for negative β during post-reversal regime than positive lift for positive β in the more conventional setting. This may have important implications for development of highly maneuverable aircraft.

2.3 Chapter Summary

Chapter 2 of this dissertation is an introduction to the aileron reversal problem. Up to now, the aeroelastic analyses have focused on rigid wings with a flexible support. These idealized configurations do give some insight into the aeroelastic stability and response, but practical analyses must take flexibility of the lifting surface into account. That being the case, Chapter 4 will address flexible wings, albeit with simplified structural representation. Two cases will be investigated: a uniform cantilevered lifting surface and a rolling aircraft with uniform wings, respectively. But before that, Chapter 3 details the proposed nonlinear approaches and tools for the aileron reversal problem. To more accurately predict reversal phenomenon and aeroelastic instability, both structural and aerodynamic nonlinearities are involved into the analyses.

CHAPTER III

TOOLS FOR NONLINEAR ANALYSES

3.1 VABS

VABS is a tool based on the variational asymptotic beam sectional analysis that is developed using a generalized Vlasov theory for composite beams with arbitrary geometric and material sectional properties. Hodges [46] initiated the idea to use the variational asymptotic method to perform the cross-sectional analysis for a general composite beam. This tool rigorously splits the geometrically-nonlinear, three-dimensional elasticity problem into a linear, two-dimensional, cross-sectional analysis and a nonlinear, one-dimensional, beam analysis. The developed theory is implemented into VABS, a general-purpose, finite-element based beam cross-sectional analysis code. The geometry of NACA 0009 airfoil is first built up in ANSYS, and then the section can be meshed through VABS-ANSYS macros. Note that the mesh size can be controlled either explicitly, by providing desired line divisions, or by changing the global size of mesh in the “vabsinp.mac” macro. Here 3-noded triangular elements are used to compose the mesh. With the meshed geometry, VABS is then used to generate the beam properties for such kind of wing section to be used in DYMORE. Furthermore, with the stress resultants and the moment resultants, VABS can calculate the nodal solutions for the stress model. The capability to recover 3-D stresses is used to check if the structures can sustain the resulting airloads during post-reversal regime, especially for the wing root.

3.2 Nonlinear Aerodynamics

3.2.1 Experimental Data

In the aerospace industry, wind-tunnel investigations of wing characteristics are made before airplanes are successfully flown and still constitute an important phase of aerodynamic testing. Until recently wing characteristics are usually obtained from tests of models of finite aspect ratio. The development of wing theory led to the concept of wing-section characteristics that are derived from data obtained from tests of finite-aspect-ratio wings. These derived data are then used to predict the characteristics of wings of different plan forms. The systematic investigations in the NACA variable-density wind tunnel are examples of this type of investigation. This method of testing is hampered by the difficulties of obtaining full-scale values of the Reynolds number and sufficiently low air-stream turbulence to duplicate flight conditions properly without excessive cost for equipment and models. Other difficulties are experienced in properly correcting the data for the support tares and interference effects and in deriving the section characteristics from tests of models necessarily having varied span-load distributions and tip effects.

In order to avoid some of these difficulties and to permit testing of models those are large relative to the size of the wind tunnel, two-dimensional testing equipment is built by the NACA. The NACA two-dimensional low-turbulence pressure tunnel provides facilities for testing wing sections in two-dimensional flow at large Reynolds numbers in an air stream of very low turbulence, approaching that of the atmosphere. The wing-section data provided by Abbott and Von Doenhoff [1] are obtained from tests in this tunnel.

This tunnel has a test section 3 feet wide and 7.5 feet high and is capable of operation

at pressures up to 10 atmospheres. The usual models are of 2-foot chord and completely span the 3-foot width of the test section. The lift is measured by integration of pressures representing the reaction on the floor and ceiling of the tunnel. The drag is obtained from wake-survey measurements, and the pitching moments are measured directly by a balance. Wing-section characteristics can be obtained from such measurements with a high degree of accuracy.

The usual tests are made over a range of Reynolds numbers from 3 to 9 million and at Mach numbers less than about 0.17. This range of Reynolds numbers covers the range where large-scale effects are usually experienced between the usual low-scale test data and the large-scale flight range. Application of these wing-section data to the prediction of the characteristics of wings of finite span depends on the adequacy of three-dimensional wing theory. Note that these data are not applicable at high speeds where compressibility effects become important.

3.2.2 XFOIL

XFOIL is a panel method code developed by Drela [31, 33] from Massachusetts Institute of Technology. It is an interactive program for the design and analysis of subsonic isolated airfoils. The first version of XFOIL was available in 1986. The main goal of XFOIL is to combine the speed and accuracy of high-order panel methods with the new fully-coupled viscous/inviscid interaction method used in the transonic airfoil/cascade analysis/design code “ISES” developed by Drela and Giles [33, 39]. The code uses a conservative finite-volume streamline grid Euler formulation to represent the outer flow, and a two-equation dissipation integral formulation to represent the viscous layers. The viscous and inviscid flows are fully coupled through the displacement

thickness. Then the entire discrete equation set, including the viscous and transition formulations, is solved as a fully coupled nonlinear system by a global Newton method. In addition, XFOIL allows ones to do geometric design about the models through direct method implemented in the code for airfoil design. Therefore, XFOIL is a good option for the initial analyses which need large amount of aerodynamic data rapidly. For a detailed description of XFOIL, see Appendix A.

In this dissertation, XFOIL is selected as the major tool to get the approximated wing-section aerodynamic characteristics, such as lift, moment, and drag coefficients, for certain Reynolds numbers and Mach numbers with viscous effects. Each airfoil with deflected trailing edge is modeled as single section in XFOIL. Through the capabilities of ISES code, the section can be modified by interactive specification of new geometric parameters such as hinge locations, aileron deflection, and airfoil dimension. To improve the accuracy of the analysis, the demonstration must be taken relative to the data provided by Abbott and Von Doenhoff [1].

To compare the aerodynamic data generated from XFOIL with the experimental data of Abbott and Von Doenhoff [1], a Mach number of 0.1 and Reynolds number of 3 million are applied. The lift coefficients for symmetrical airfoil sections calculated using XFOIL agree well with those in Abbott and Von Doenhoff [1], and there is only 2% error for XFOIL's results relative to the data in Ref [1]. Note that with increasing thickness of airfoil, XFOIL's result has more error. From Figures 3.1, 3.2, and 3.3, not only the data points but the trends from negative to positive angles of attack are in good agreement. The lift-curve slopes agree well, and there is only 2.5% error for XFOIL's results relative to the data in Ref [1]. XFOIL's result has 6.5% error relative to the data in Ref [1] for the cambered airfoil, NACA 4415. Compared Figures 3.3 and 3.4, XFOIL can predict the

performance of symmetrical airfoil better. In Figures 3.4 and 3.5, although there are small differences beyond the stall angles of attack, the results are acceptable.

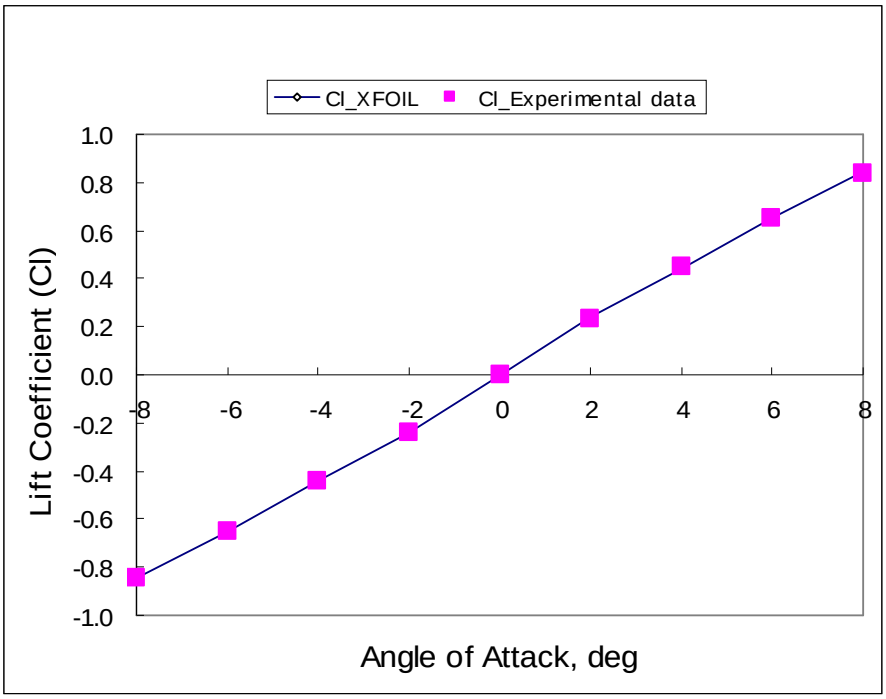

Figure 3.1: Validations for lift coefficient (NACA 0006)

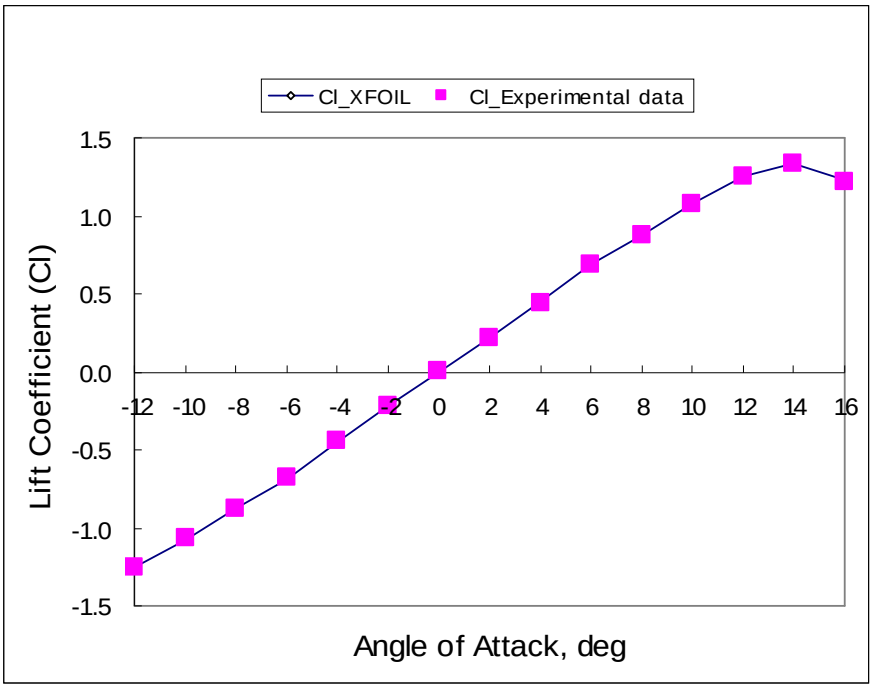

Figure 3.2: Validations for lift coefficient (NACA 0009)

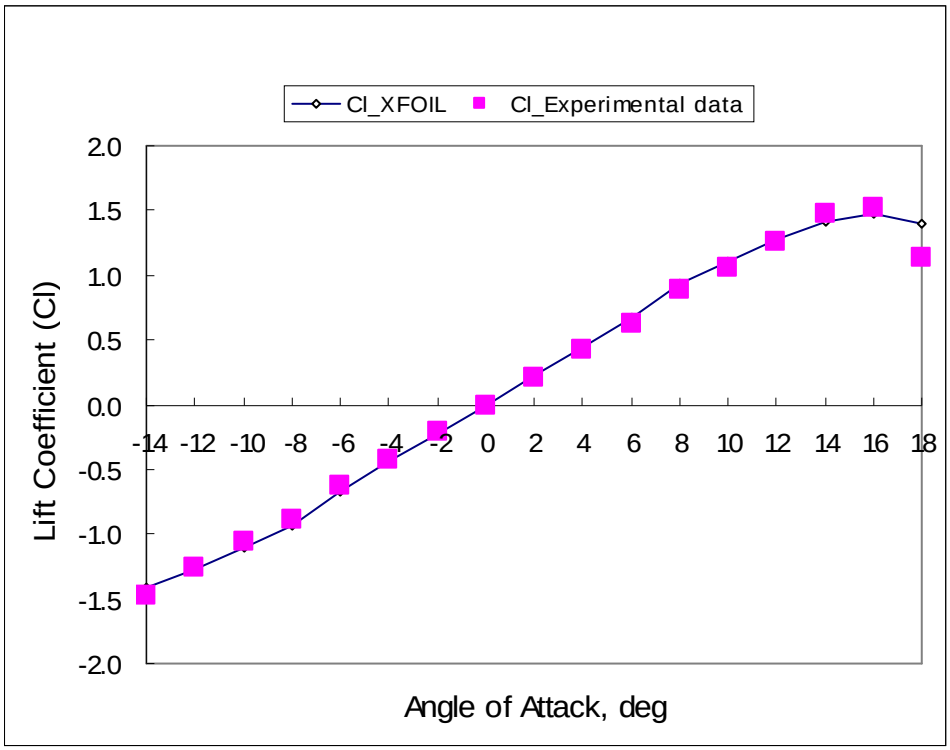

Figure 3.3: Validations for lift coefficient (NACA 0012)

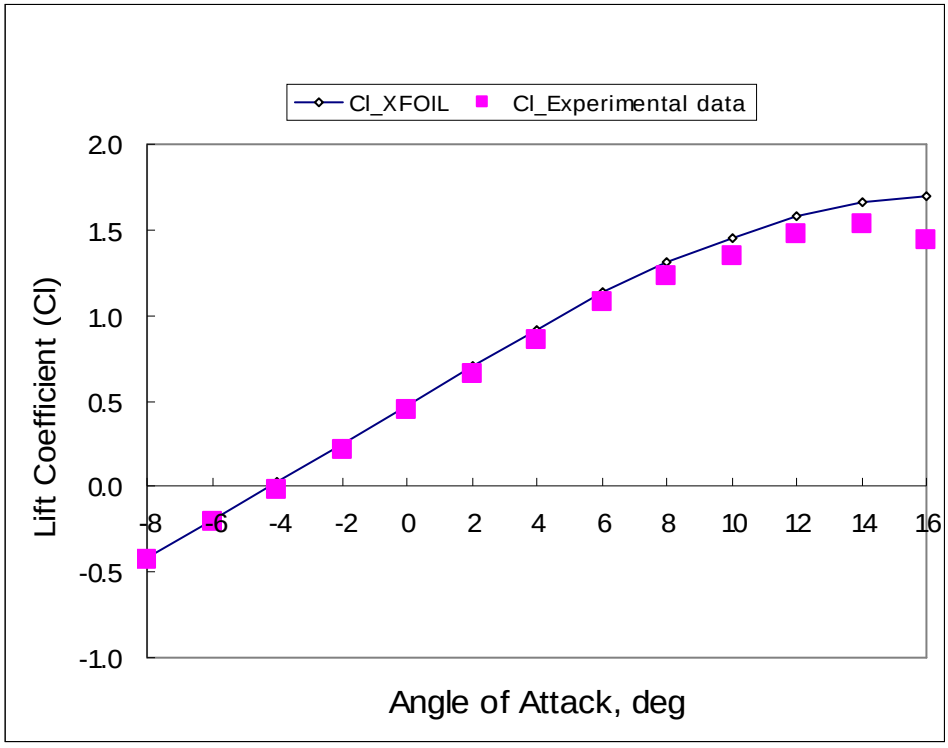

Figure 3.4: Validations for lift coefficient (NACA 4412)

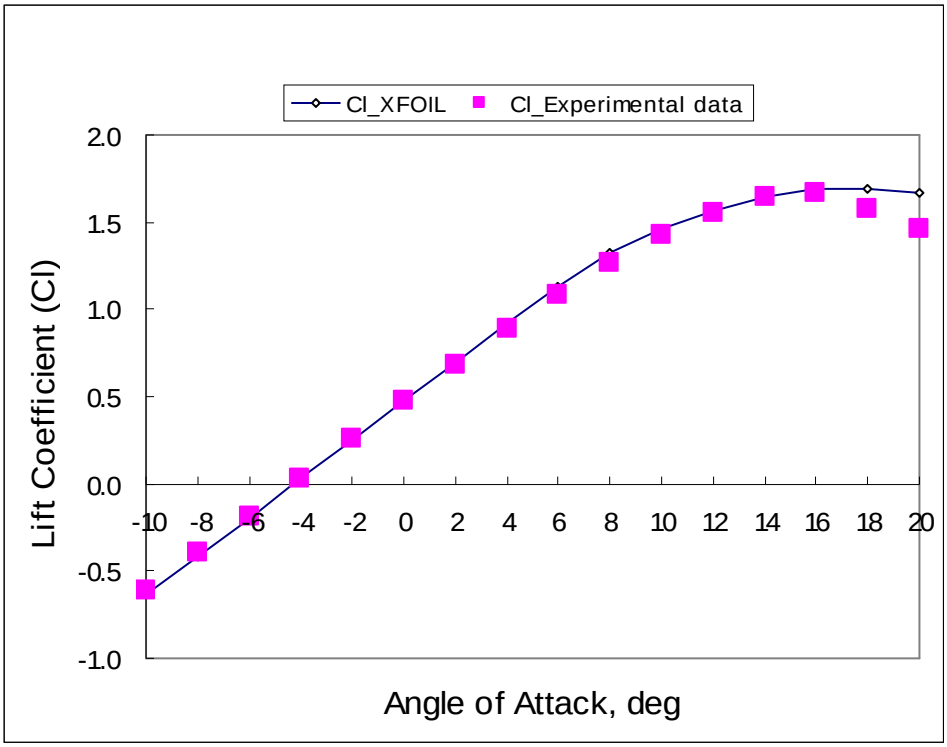

Figure 3.5: Validations for lift coefficient (NACA 4415)

Similarly, for moment coefficient about the quarter-chord, XFOIL's data has good agreement with the results provided by Abbott and Von Doenhoff [1], in the linear regime. Because the moment coefficients about the quarter-chord for symmetric airfoil sections approach to zero, it is very difficult to tell the difference between XFOIL and experimental data. Therefore, the moment coefficients for cambered airfoil sections are compared herein. For cambered airfoil sections, there is 10% error for the results relative to the data recorded in Ref [1] (see Figures 3.6 and 3.7), and the trend after stall is not captured. Since most of airfoil computations used in this dissertation are based on the NACA 0009 airfoil, the results with 2.5% error relative to experimental data are acceptable, and especially capturing the trends before stall is the main purpose.

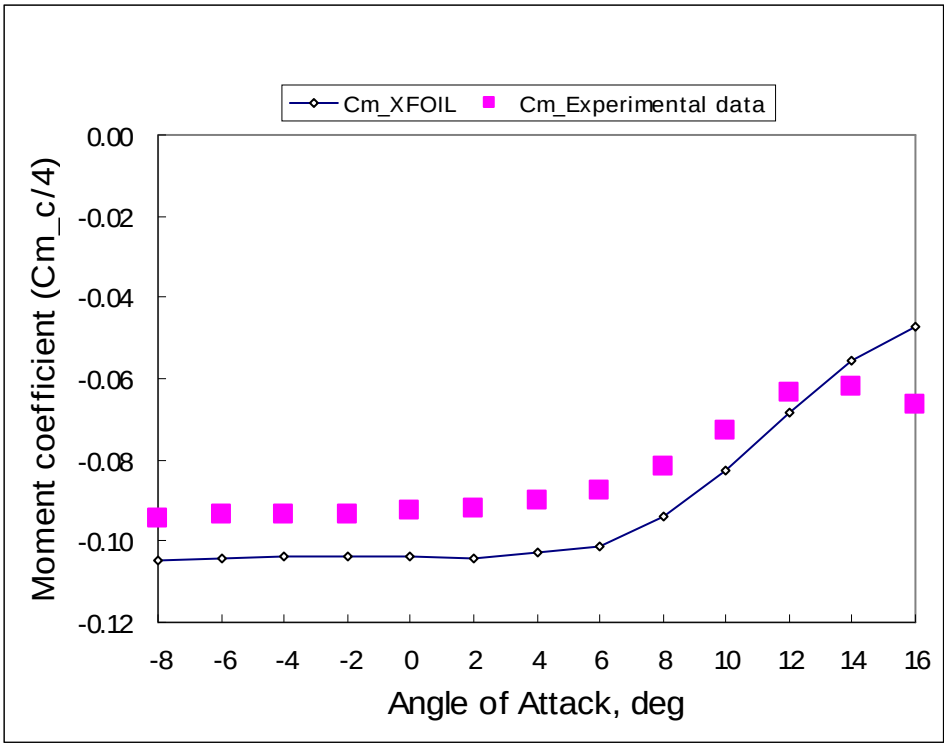

Figure 3.6: Validations for moment coefficient about the quarter-chord (NACA 4412)

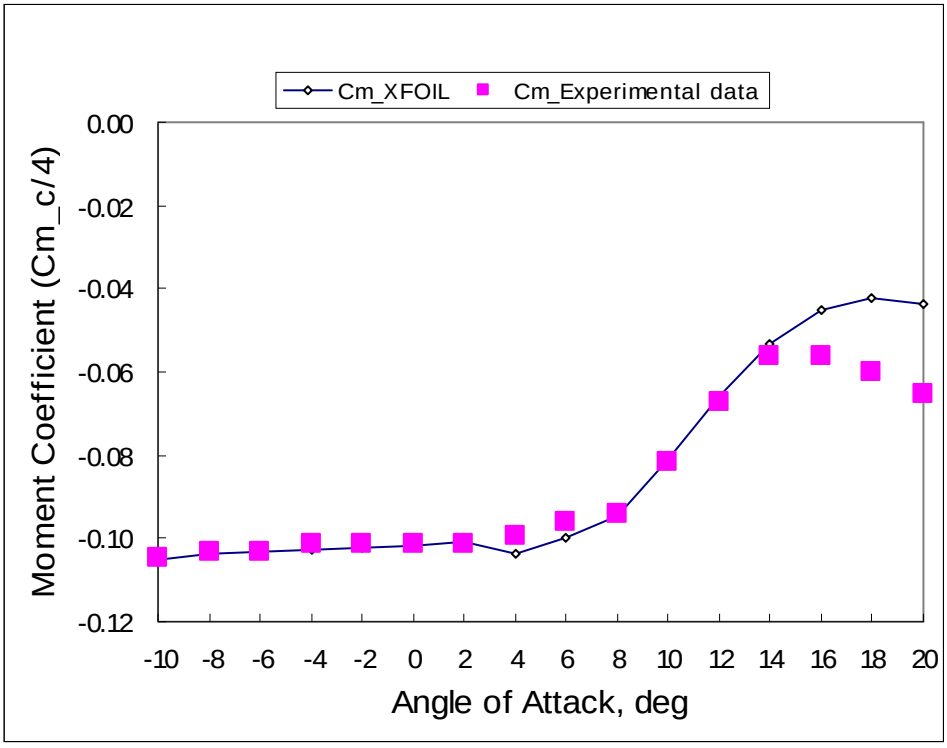

Figure 3.7: Validations for moment coefficient about the quarter-chord (NACA 4415)

3.3 Nonlinear Aeroelasticity–DYMORE

3.3.1 Introduction

The structural models are built through a finite element based, multibody dynamics analysis tool, called DYMORE. Multibody dynamics analysis is originally developed for modeling mechanisms with simple tree-like topologies composed of rigid bodies, but the methodology has considerably evolved to the point where it can handle nonlinear flexible systems with arbitrary topologies. It is now widely used as a fundamental design tool in many areas of mechanical engineering, such as the automotive, railroad, and aerospace industries. In the automotive industry, for example, multibody dynamics analysis is routinely used for optimizing vehicle ride qualities, a complex multidisciplinary task that involves the simulation of many different sub-components. The success of multibody dynamics analysis tools stems from their flexibility: a given mechanism can be modeled by an idealization process that identifies the mechanism components from within a large library of elements implemented in the code. The element library in DYMORE involves structural elements: rigid bodies, composite capable beams and shells, and joint models. Rigid body and beam models are fundamental elements of aircraft multibody models. Shells models can be used for more advanced analyses as well. All these elements are characterized by the presence of displacement and rotational fields that are referred to a single inertial. Arbitrarily large displacements and finite rotations are treated exactly.

Beams are typically used for modeling wings but can also be useful for representing flaps. Here the wings of either the cantilevered wing model or rolling aircraft model are modeled with beam elements. In view of the increasing use of composite materials in aircraft structures, the ability to model components made of laminated composite materials is getting important. Specially, it must be possible to represent shearing

deformation effects, the offset of the center of mass and of the shear center from the beam reference line, and all the elastic couplings that can arise from the use of tailored composite materials.

A distinguishing feature of multibody systems is the presence of a number of joints that impose constraints on the relative motion of the various bodies of the system. Most joints used for practical applications can be modeled in terms of the so called “lower pairs” [6]: the revolute, prismatic, screw, planar, cylindrical, and spherical joints, depicted in Figure 3.8. Mechanically actuated control surfaces are easily modeled with the help of lower pair joints. If two bodies are rigidly connected to one another, their six relative motions, three displacements and three rotations, must vanish at the connection point. If one of the lower pair joints connects two bodies, one or more relative motions will be allowed. Table 3.1 defines the six lower pairs in terms of the relative displacement and rotation components that can be either free or constrained to a null value.

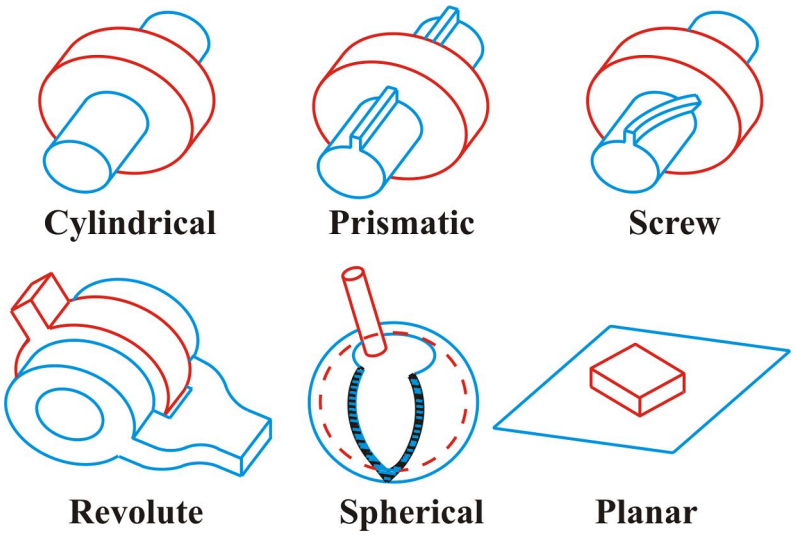

Figure 3.8: The six lower pairs quoted from Ref. [57]

Table 3.1: Definition of the six lower pair joints quoted from Ref. [57]. For the screw joint, p is the screw pitch.

	Relative Displacements			**Relative Rotations**		
Joint Type	d_1	d_2	d_3	θ_1	θ_2	θ_3
Revolute	No	No	No	No	No	Yes
Prismatic	No	No	Yes	No	No	No
Screw	No	No	$= p\theta_3$	No	No	Yes
Planar	Yes	Yes	No	No	No	Yes
Cylindrical	No	No	Yes	No	No	Yes
Spherical	No	No	No	Yes	Yes	Yes

The explicit definition of the relative displacements and rotations in a joint as additional unknown variables represents an important implementation. First of all, it allows the introduction of generic spring and damper elements in the joints, as usually required for the modeling of realistic configurations. Second, the time histories of joint relative motions can be driven according to suitably specified time functions. In the models of this dissertation, for instance, the ailerons setting can be obtained by prescribing the time history of the relative rotation at the corresponding joints.

3.3.2 Airtable

To simulate aerodynamic nonlinearities, a full range of angles of attack, i.e. $-180^\circ \le \alpha \le 180^\circ$, look-up tables with aerodynamic data must be built up. The airfoil data set consists of lift, drag, and pitching moment coefficient tables. Each coefficient table defines the corresponding aerodynamic coefficients as a function of Mach number

and angle of attack by means of a double entry table. To generate these airtables, the viscous analysis of XFOIL is used to provide aerodynamic coefficients. Data are obtained varying Reynolds number, angle of attack, and flap angle. The limitations of the boundary-layer analysis to moderately separated conditions at stall and the potential flow model to the linear regime suggest that post-stall corrections are needed. The simple approximations as Eqns. (12) described in Ref. [64] are implemented here. They are based on empirical observation of airfoils at extreme angles of attack measured by Critzos et al. [25], and only the case of static stall is considered. All measurements are at low Mach numbers. The angle of attack is defined as the angle between zero-lift line and relative wind vector. Thus, the post-stall lift, moment, and drag coefficients are given in terms of the current and zero-lift angles of attack, α and α_0 respectively. Note that the zero-lift angle of attack for NACA 0009 is zero.

$$\begin{aligned} c_l &= 1.175\sin 2(\alpha - \alpha_0) \\ c_m &= -0.5\sin(\alpha - \alpha_0) + 0.11\sin 2(\alpha - \alpha_0) \\ c_d &= 1.135 - 1.05\cos 2(\alpha - \alpha_0) \end{aligned} \tag{12}$$

The angle from zero-lift corresponding to the onset of stall for an airfoil of given thickness is nearly invariant with respect to its camber. The stall angle is assumed to be $+/-12^\circ$ based on the data in Ref. [1] for the NACA 0009 airfoil. Therefore, aerodynamic coefficients for the specific geometry of an airfoil in XFOIL, such as an airfoil with a deflected trailing edge, are used to establish the airtable within the linear regime, and Eqns. (12) is used to generate the data outside the linear regime.

3.3.3 Inflow Model

The inflow element is a component of the aerodynamic model in DYMORE that computes the dynamic inflow field generated by the unsteady circulation at the airstation associated with the inflow disk. The induced flow model is based on the work of Peters and his co-workers for two-dimensional [94] and three-dimensional problems [91, 92]. Peters and Karunamoorthy show that a Glauert expansion of inflow states could be used to derive a set of ordinary differential state equations in which the states represented inflow distributions. From their results, for a thin airfoil with trailing-edge flap, the lift and pitching moment for the main wing can be derived from the total airloads and airloads for the flap. The relation is listed below,

$$\begin{aligned} L_W &= -\left(L_0 + L_a\right) \\ M_W &= \frac{b}{2} L_0 + bL_1 + \frac{b}{2}\left(2 + d\right)L_a - M_a \end{aligned} \tag{13}$$

where L_a and M_a are generalized lift and pitching moment for aileron; L_0 and L_1 are expansions of generalized airloads.

Traditionally, there are leading-edge control devices to ensure that the wing is never without the means to be controlled after aileron reversal. Much work in AAW program has been done to enhance roll performance by combining leading- and trailing-edge wing control surfaces [3]. Based on this idea, the relation between the main wing and leading-edge control surface is derived here as below,

$$\begin{aligned} L_W &= -\left(L_0 + L_c\right) \\ M_W &= \frac{b}{2} L_0 + bL_1 - \frac{bd}{2} L_c - M_c \end{aligned} \tag{14}$$

where L_c and M_c are generalized lift and pitching moment for leading-edge control surface.

To investigate the influence of leading-edge control surfaces for the aeroelastic

reversal problem more clearly, a simple case of the thin airfoil with both leading- and trailing-edge control surfaces is showed as following. In Peters' finite state inflow model for two-dimensional thin airfoil [89, 93], the theoretical airloads equations are derived from the following equations:

The non-penetration condition:

$$\bar{v} = u_0 \partial h/\partial x + \partial h/\partial t + v_0 + v_1 x/b - \lambda \tag{15}$$

The induced flow due to bound vorticity:

$$\bar{v} = \frac{-1}{2\pi} \int_{-b}^{b} \frac{\gamma_b(\xi, t)}{x - \xi} d\xi \tag{16}$$

The pressure-vorticity equation:

$$\Delta P = \rho u_0 \gamma_b + \rho \int_{-b}^{x} \partial \gamma_b / \partial t d\xi \tag{17}$$

The induced flow due to other vorticity:

$$\partial \lambda/\partial t + u_0 \partial \lambda/\partial x = \frac{1}{2\pi} \frac{d\Gamma/dt}{b - x} + \bar{u}_0 \partial \xi/\partial x \tag{18}$$

The total bound vorticity on the airfoil:

$$\Gamma \equiv \int_{-b}^{b} \gamma_b dx \tag{19}$$

For the case of thin airfoil with both leading- and trailing-edge control surfaces as Figure 3.9, assume both control surfaces deflect ϕ degree downwards, i.e. $\phi_a = \phi_c = \phi$, and are located at points with the same distance from the mid-chord.

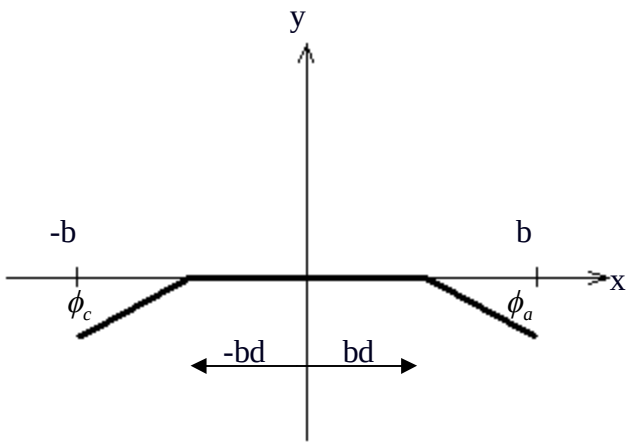

Figure 3.9: Geometry of control surfaces

The generalized airloads for leading- and trailing-edge control surfaces are

$$
\begin{aligned}
L_0^a &= \frac{2\sin\phi_a}{\pi}\left[\frac{\phi_a}{2\sin\phi_a}L_0 + \sum_{k=1}^{\infty}\frac{U_{k-1}}{k}L_k\right] \\
L_1^a &= \frac{\sin\phi_a}{\pi}\left[L_0 + \left(\frac{\phi_a}{\sin\phi_a} + \frac{U_1}{2}\right)L_1 + \sum_{k=2}^{\infty}\left(\frac{U_{k-2}}{k-1} + \frac{U_k}{k+1}\right)L_k\right] \\
L_0^c &= \frac{2\sin\phi_c}{\pi}\left[\frac{\pi-\phi_c}{2\sin\phi_c}L_0 - \sum_{k=1}^{\infty}\frac{U_{k-1}}{k}L_k\right] \\
L_1^c &= \frac{-\sin\phi_c}{\pi}\left[L_0 + \left(\frac{\phi_c-\pi}{\sin\phi_c} + \frac{U_1}{2}\right)L_1 + \sum_{k=2}^{\infty}\left(\frac{U_{k-2}}{k-1} + \frac{U_k}{k+1}\right)L_k\right]
\end{aligned}
\tag{20}
$$

where U_n is Chebyshev polynomials of second kind; the airloads for main wing are

$$
\begin{aligned}
L_W &= -(L_0 + L_c + L_a) \\
M_W &= \frac{b}{2}L_0 + bL_1 - \frac{bd}{2}L_c + \frac{b}{2}(2+d)L_a - M_c - M_a
\end{aligned}
\tag{21}
$$

assuming

$$
\begin{aligned}
L_a &= -L_0^a \\
M_a &= bL_1^a - \frac{b}{2}(1+d)L_0^a \\
L_c &= -L_0^c \\
M_c &= bL_1^c + \frac{b}{2}(1+d)L_0^a
\end{aligned}
\tag{22}
$$

Obviously, after substituting Eqns. (20) and (22) into Eqn. (21), both lift and pitching moment for main wing will be cancelled out. Although it is a simple case of a thin airfoil with multiple control surfaces, it did show the benefit to add the leading-edge control surface to compensate the loss of control effectiveness. Especially when the vehicle is operated close to reversal speed, leading-edge control surfaces are useful devices to replace ailerons to control the vehicle. This may have important implications for development of highly maneuverable aircraft. Indeed, many efforts have been contributed to AAW flight research program [3].

In this dissertation, Peters' 3D inflow model [91, 92] is implemented in DYMORE to compute the dynamic inflow field generated by the unsteady circulation at the airstation associated with the inflow disk. "DYNAMIC_INFLOW" is set as the inflow type in DYMORE for all the models herein, which means the inflow model is based on the theory for unsteady flow over a circular disk with a pressure jump across that disk. The induced flow distribution can be represented in an analogous expansion to that used for pressure in terms of a harmonic variation in azimuth and arbitrary radial distribution functions Ψ_j^r

$$w(\bar{r},\psi,\bar{t}) = \sum_{r=0}^{\infty} \sum_{j=r+1,r+3,\ldots}^{\infty} \Psi_j^r(\bar{r}) \left[a_j^r(\bar{t}) \cos(r\psi) + b_j^r(\bar{t}) \sin(r\psi) \right] \tag{23}$$

where the set of radial expansion function, the $\Psi_j^r(\bar{r})$, must be linearly independent and complete for a given harmonic *r*. The a_j^r, and b_j^r are induced flow expansion coefficients and can be regards as the time-dependent states of the induced-flow model. Here "6" is set as the number of inflow modes in DYMORE input to determine the number of harmonics for the states used for the solution over the inflow disk. When this

number is used, DYMORE automatically uses “28” states of inflow model to compute the pressure difference for each airstation over the inflow disk. The choice of this number and location of the airstations of the associated lifting lines will greatly affect the accuracy and efficiency of the solution. Ten airstations are used in all the models associated with the number of modes, “6”, in this dissertation.

3.3.4 Results for Uniform Lifting Surface without Aileron

To verify the practicality of the aeroelastic model built using DYMORE, consider an unswept uniform elastic lifting surface as illustrated in Figure 3.10. The lifting surface is modeled as a beam and is presumed to be built in at its root ($y = 0$, to represent attachment to a wind-tunnel wall or a fuselage) and free at its tip ($y = \ell$). The y-axis corresponds to the elastic axis, which may be defined as the line of effective shear centers, assumed here to be straight. For isotropic beams, a transverse force applied at any point along this axis will result in bending with no elastic torsional rotation about the axis. This axis is also the axis of twist in response to a pure twisting moment applied to the wing. Because the primary concern here is the determination of the airload distributions, the only elastic deformation that will influence these loads is twist about the elastic axis.

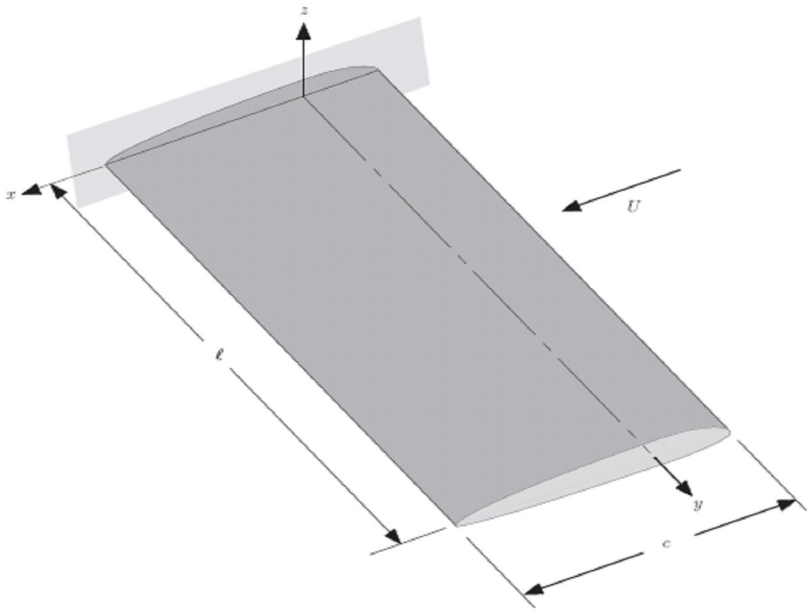

Figure 3.10: Uniform unswept cantilevered lifting surface quoted from Ref. [47]

According to Ref. [47], the divergence dynamic pressure for a cantilevered wing is given by

$$q_D = \frac{GJ}{eca}\left(\frac{\pi}{2l}\right)^2 \tag{24}$$

This result is for strip theory aerodynamics, i.e. without 3D effects. For a 10-foot wingspan, 1-foot chord, quarter-foot offset from aerodynamic center to elastic axis, constant lift-curve slope 6.211, and given torsional stiffness 24,370 lb-ft^2, the theoretical result for divergence dynamic pressure is 387.23 lb/ft^2. A cantilevered wing model is set up in DYMORE, and a schematic of which is shown as Figure 3.11. To involve Peters' 3D inflow model in DYMORE, wings on both sides of a clamp need to be established because the inflow model simulate 3D induced flow around a disk. Note that 6 is set as the number of inflow modes in the analysis, which means 28 states of the induced-flow expansion over the disk are automatically used in DYMORE. In Figure 3.11, the pink

surface is the wing on the right hand side of the clamp, and that is the object to be evaluated for wing divergence. The results with and without 3D effects (tip loss and 3D inflow) are shown in Table 3.2.

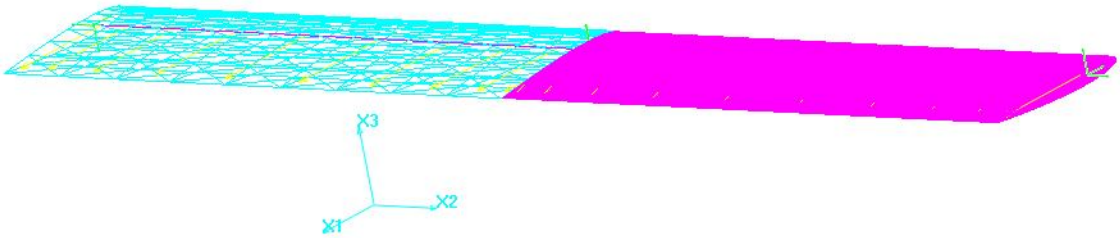

Figure 3.11: DYMORE simulation for uniform unswept cantilevered lifting surface

Table 3.2: DYMORE results for uniform unswept cantilevered lifting surface

	Theory	**DYMORE**	
		Without 3D effects	**With 3D effects**
Divergence Dynamic Pressure (lb/ft^2)	387.23	387.66	416.70

Obviously, the result with 3D effects is higher than the theoretical result, which is less conservative herein. To check tip rotation of the wing, the operating dynamic pressure is normalized by divergence dynamic pressure such as $\bar{q} = q/q_D$. Since the aeroelastic instability will result in a catastrophic failure, which people try to avoid, the behavior of tip twist angle versus non-dimensional dynamic pressure up to 80% divergence is reported in Table 3.3.

Table 3.3: DYMORE results of tip rotation for $\alpha = 1^\circ$

Non-dimensional Dynamic Pressure $\bar{q}$	0	0.1	0.2	0.3	0.4	0.5	0.6	0.7	0.8
Tip Twist Angle (deg)	0	0.07	0.13	0.20	0.26	0.31	0.37	0.42	0.42

3.4 Chapter Summary

This chapter introduces the tools used for the nonlinear analyses. That are XFOIL, a panel method code, and DYMORE, a finite element based multibody dynamic code. Using XFOIL and with the auxiliary experimental data, aerodynamic nonlinearities are involved in nonlinear aeroelastic model built in DYMORE. This is the main approach in this dissertation to implement the idea which is improving roll maneuverability by using post-reversal design. The aerodynamic data from XFOIL is compared with the experimental data in Section 3.2.1. Results show XFOIL is a reliable tool for this approach, and especially the stall phenomenon is what to avoid. A simple aeroelastic DYMORE model, the uniform lifting surface, is checked for the divergence with theory in Section 3.3.4. DYMORE result has a good agreement with the theoretical calculation for the aeroelastic instability problem. In Chapter 4, an aileron is added in two models, which are uniform cantilevered lifting surface and rolling aircraft with rectangular wings, respectively. The phenomena for reversal and divergence will be discussed and results reported there.

CHAPTER IV

SYSTEM MODELS FOR AEROELASTIC PROBLEMS

4.1 Uniform Lifting Surface with Aileron

4.1.1 Aeroelastic Model

Up to now, the aeroelastic analyses for wing-aileron system have focused on rigid wings with a flexible support. These idealized configurations do give some insight into the aeroelastic stability and response, but practical analyses must take flexibility of the lifting surface into account. That being the case, flexible wings will be addressed in this section, albeit with simplified structural representation.

Consider an unswept uniform elastic lifting surface as illustrated in Figure 4.1. In order to be consistent to the aerodynamic model in XFOIL, the lifting surface with aileron is modeled as a beam and is presumed to be built in at its root ($y = 0$, to represent attachment to a wind-tunnel wall or a fuselage) and free at its tip ($y = \ell$). The y-axis corresponds to the elastic axis, which may be defined as the line of effective shear centers, assumed here to be straight. For isotropic beams, a transverse force applied at any point along this axis will result in bending with no elastic torsional rotation about the axis. This axis is also the axis of twist in response to a pure twisting moment applied to the wing. Because the primary concern here is the determination of the airload distributions, the major one elastic deformation that will influence these loads is twist about the elastic axis.

NACA 0009 airfoil is selected as the wing section of the lifting surface models (same for the wing section of the rolling aircraft models). For the initial analyses, a solid section and isotropic material are used for the wing. DYMORE is used for the multibody

dynamics analysis. This model is an aeroelastic problem dealing with the rectangular planform wing clamped at its mid-point shown as the green point on the left hand side of the wing in Figure 4.1. The wing has a rectangular planform of length L = 15 ft and chord length c = 1 ft. The 15-foot aileron extends along the span of the whole wing, where the hinge location is at 80% chord of the main wing. The structural properties of the cantilevered wing are as follows: bending stiffness, $EI = 2.365\times10^5$, torsional stiffness, $GJ = 2.39\times10^4$ (both in lb-ft^2), mass per unit span, m = 0.0075 (slug/ft), polar moment of inertia, I = 0.0195 (slug-ft). The airfoil quarter-chord and center of mass are located 0.084 ahead and 0.6 ft aft of the wing elastic axis, respectively. The wing span is modeled with cubic beam elements [10, 11].

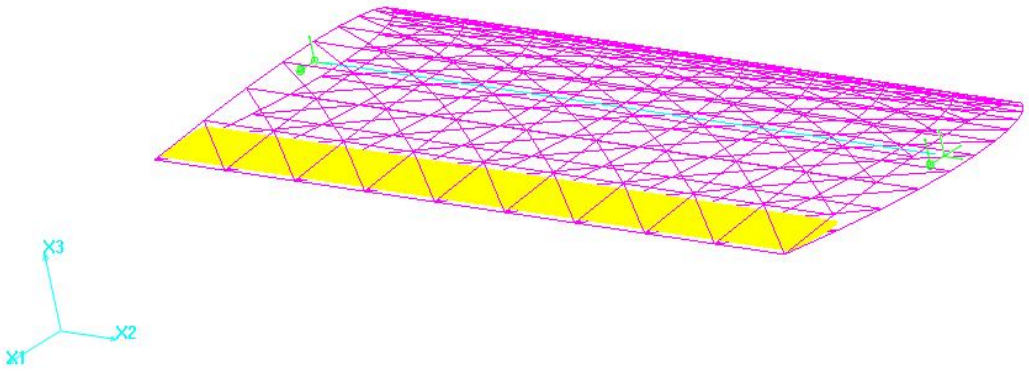

Figure 4.1: Configuration of uniform lifting surface with aileron

4.1.2 Theoretical Results

With the geometry and boundary conditions of the uniform lifting surface as above, one can derive the associated divergence and reversal dynamic pressures. The expression of the divergence dynamic pressure for cantilevered wing [47] is given as follow:

$$q_D = \frac{GJ}{ecc_{l_\alpha}}\left(\frac{\pi}{2\ell}\right)^2 \tag{25}$$

which *e* is the distance from aerodynamic center to elastic axis. Note that the difference between Eqns. (24) and (25) is assuming the sectional lift-curve slope is constant and denoted by "*a*" in Eqn. (24). Here the aerodynamic nonlinearities are involved by building up the look-up airtable in DYMORE, and the sectional lift-curve slope is denoted by "c_{l_α}" instead.

The total lift for the uniform lifting surface is

$$L = qc\ell\left\{c_{l_\alpha}\left[\left(\alpha_{\mathrm{r}} + \overline{\alpha}_{\mathrm{r}}\right)\frac{\tan(\lambda\ell)}{\lambda\ell} - \overline{\alpha}_{\mathrm{r}}\right] + \mathrm{c}_{l_\beta}\beta\right\} \tag{26}$$

which α_{r} is rigid angle of attack [47] from a "rigid" rotation of the surface (plus any built-in twist although none is assumed to exist here), and

$$\lambda^2 \equiv \frac{qcc_{l_\alpha}e}{GJ} \tag{27}$$

so that

$$\overline{\alpha}_r = \frac{cc_{m_\beta}}{ec_{l_\alpha}}\beta + \frac{c_{l_\beta}}{c_{l\alpha}}\beta - \frac{Nmgd}{qcec_{l_\alpha}} \tag{28}$$

From the definition for aileron reversal, that is

$$\frac{\partial L}{\partial \beta} = 0 \Rightarrow \frac{\tan(\lambda\ell)}{\lambda\ell} = \frac{cc_{m_\beta}}{cc_{m_\beta} + ec_{l_\beta}} \tag{29}$$

Substitute the dimensions of the model and the aerodynamic coefficients from running XFOIL, resulting in $\lambda\ell = 1.119$. Thus

$$q_R = \frac{1.119^2 GJ}{cec_{l_\alpha}\ell^2} = \frac{1.25GJ}{cec_{l_\alpha}\ell^2} \tag{30}$$

The reversal dynamic pressure from theoretical calculation is 254.33 lb/ft^2. The

divergence dynamic pressure is 501.14 lb/ft^2 from theoretical calculation. One can see the reversal dynamic pressure is 50% lower than the divergence dynamic pressure. The region between reversal and divergence is called post-reversal regime and will be discussed in this dissertation.

For theoretical calculation, one can consider simple 3D tip effects (tip loss factor equal to 0.97), which means integrating spanwise lift from wing root to 97% span. For aileron reversal, Eqn. (29) becomes

$$\frac{\partial L}{\partial \beta} = 0 \Rightarrow \frac{\tan(\lambda \ell)}{\lambda \ell} = \frac{0.98 cc_{m_\beta} - 0.02 ec_{l_\beta}}{cc_{m_\beta} + ec_{l_\beta}} \tag{31}$$

where $\lambda \ell = 1.160$ for this case. Thus

$$q_R = \frac{1.160^2 GJ}{cec_{l_\alpha} \ell^2} = \frac{1.346 GJ}{cec_{l_\alpha} \ell^2} \tag{32}$$

and the result is reported in Table 4.1. Note that to calculate divergence herein, the same homogeneous torsional equation of equilibrium as 2D theory is used and results in the same expression for divergence as Eqn. (25). Therefore, the same solution of divergence dynamic pressure for simple 3D theory as that for 2D theory is shown in Table 4.1.

4.1.3 Numerical Results

For the DYMORE model, the airtable is built based on the aerodynamic coefficients for the NACA 0009 airfoil using XFOIL and Eqns. (12). XFOIL model is given a flap angle β of 1 degree and a zero rigid angle of attack at the beginning to generate aerodynamic coefficients. Then the data is put in DYMORE for use. The numerical results with and without 3D effects for total lift of the wing versus the dynamic pressure are shown as Figure 4.2. Note that the meaning of “without 3D effects” is there is no

inflow involved and no tip loss is assumed in the model. Instead, tip loss and 28 states of the induced-flow expansion over the disk are used in the model with 3D effects. Extracting the data stored in DYMORE outputs for the point where the net lift becomes negative and calculating the divergence dynamic pressure and reversal dynamic pressure, the results are shown in Table 4.1.

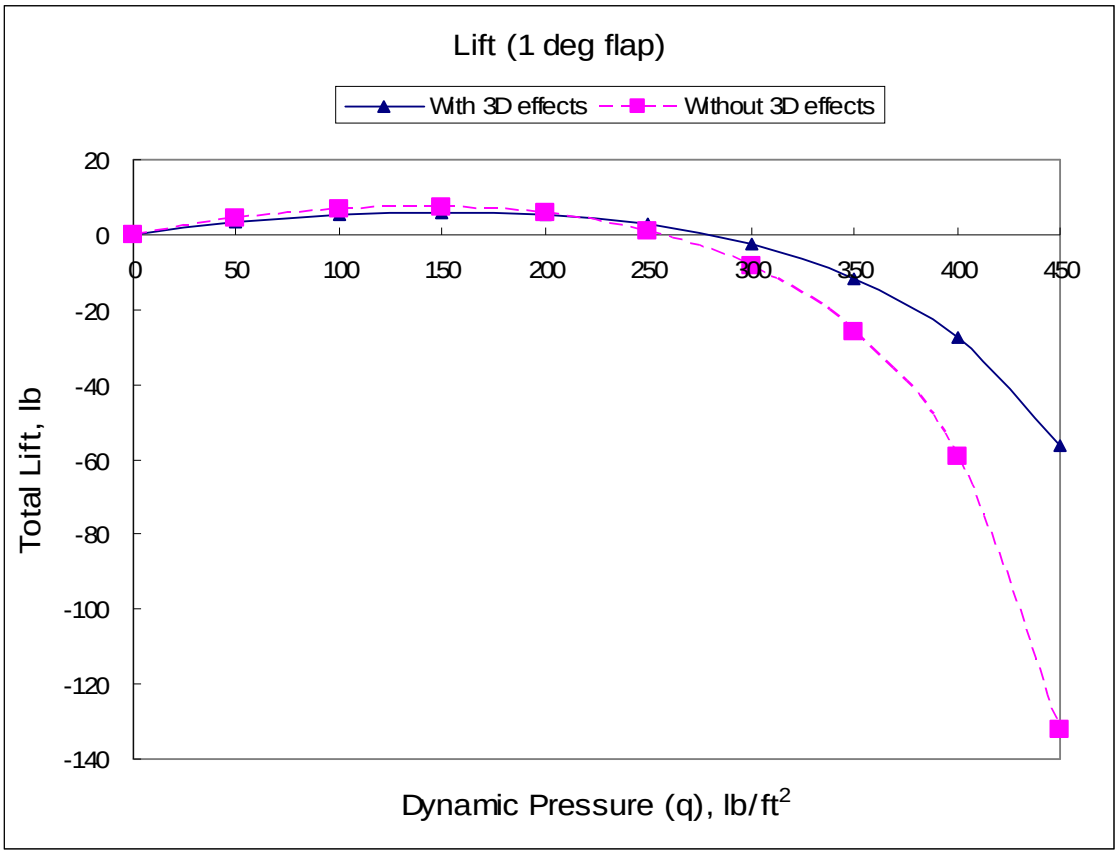

Figure 4.2: Total lift of the wing versus the dynamic pressure

Table 4.1: Comparison between DYMORE and theory

	DYMORE		**Theory**	
Reversal Dynamic Pressure lb/ft^2	With 3D Effects	Without 3D Effects	2D	3D (with tip effects)
	279.68	257.09	254.33	273.31
Divergence Dynamic Pressure lb/ft^2	561.17	505.45	501.14	501.14

Both results for reversal are higher than 2D theory due to the theoretical calculation is less conservative. The model without 3D effects has closer assumptions to the 2D theory, and the reversal dynamic pressure only has 1.1% difference with the theoretical result. For the model with 3D effects, the reversal dynamic pressure is 2.3% higher than that for simple 3D theoretical result (with tip loss), and that because there is some 3D effects, such as inflow velocity, not been considered in 3D theoretical calculation. If the wing is rigid (without flap), the curve will go along the zero axis throughout the whole regime of dynamic pressure. Since the wing is elastic, a small flap angle will make the camber change, and the lift increase. The effective change in the camber also induces a nose-down pitching moment that, due to the flexibility of the wing, tends to decrease angles of attack and decrease the lift in turn. Consequently, the net lift generation is decreased after reversal occurs. The divergence is purely dependent upon the structure, although it is a phenomenon of aeroelastic instability. The divergence without 3D effects agrees with theory well, but that with 3D effects is higher than the theoretical result. That is because the model with 3D effects is more conservative, whereas the tip loss factor is involved. Thus, lower lift is generated at the wing tip and tended to get lower potential to reach the aeroelastic instability in the DYMORE model. Since the model with 3D effects is more physically appropriate, it will be used to investigate the post-reversal regime in the following analyses.

To inspect the control surface effectiveness, the aileron lift effectiveness, η, is defined as the aeroelastic change in lift per unit change in β divided by the change in lift per unit change in β that would result is the wing not flexible in torsion as Eqn. (10). The theoretical derivation for typical section shown as before in Eqn. (11) also can be used,

$$\eta = \frac{1 - \frac{q}{q_R}}{1 - \frac{q}{q_D}}$$

On the other hand, aileron reversal can also be thought as the point where the wing root bending moment vanishes [57]. Indeed, for flying aircraft, aileron reversal occurs while there is not enough antisymmetric bending moments provided for aircraft to do rolling maneuver conventionally. Thus, aileron effectiveness can be defined as

$$\eta = \frac{M_{elastic}}{M_{rigid}} \tag{33}$$

Results recorded in DYMORE are used to present the aileron effectiveness in these three different ways and shown in Figures 4.3 and 4.4. Note that the black dash line represents the aileron effectiveness if the wing is rigid.

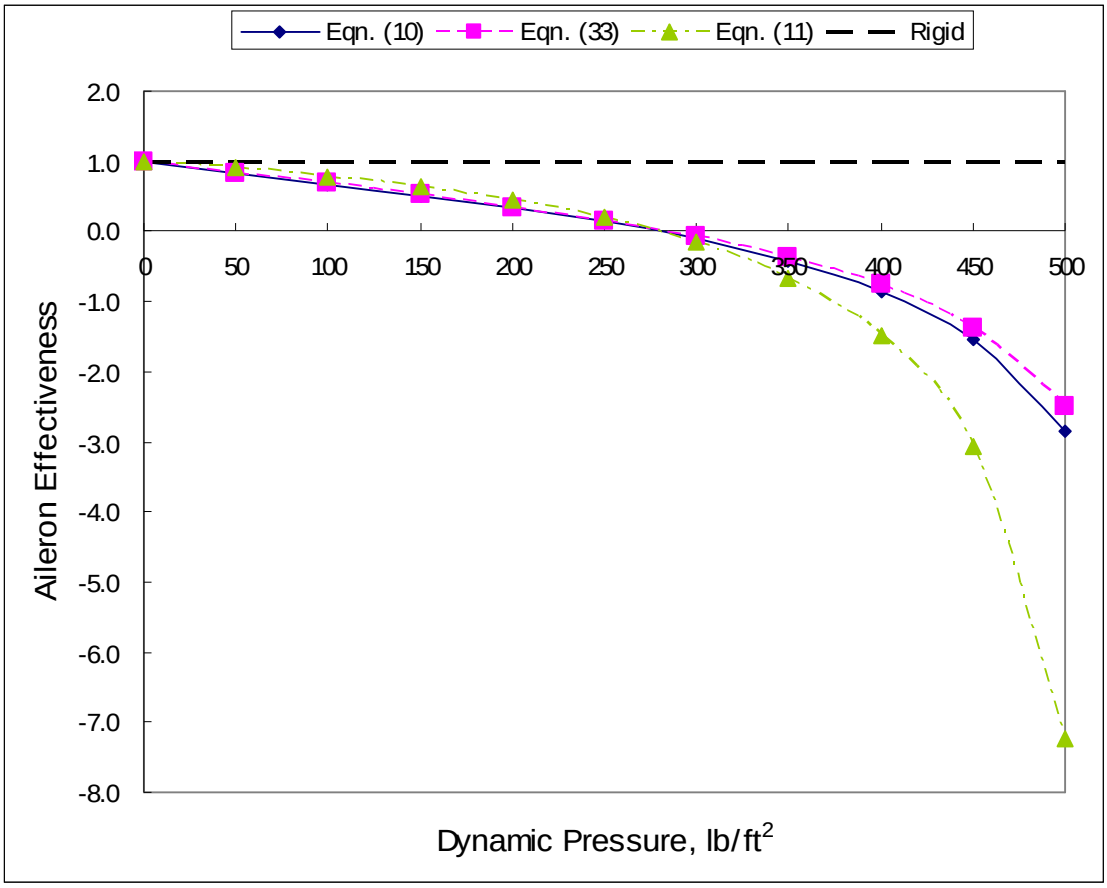

Figure 4.3: Comparisons of aileron effectiveness (with 3D effects)

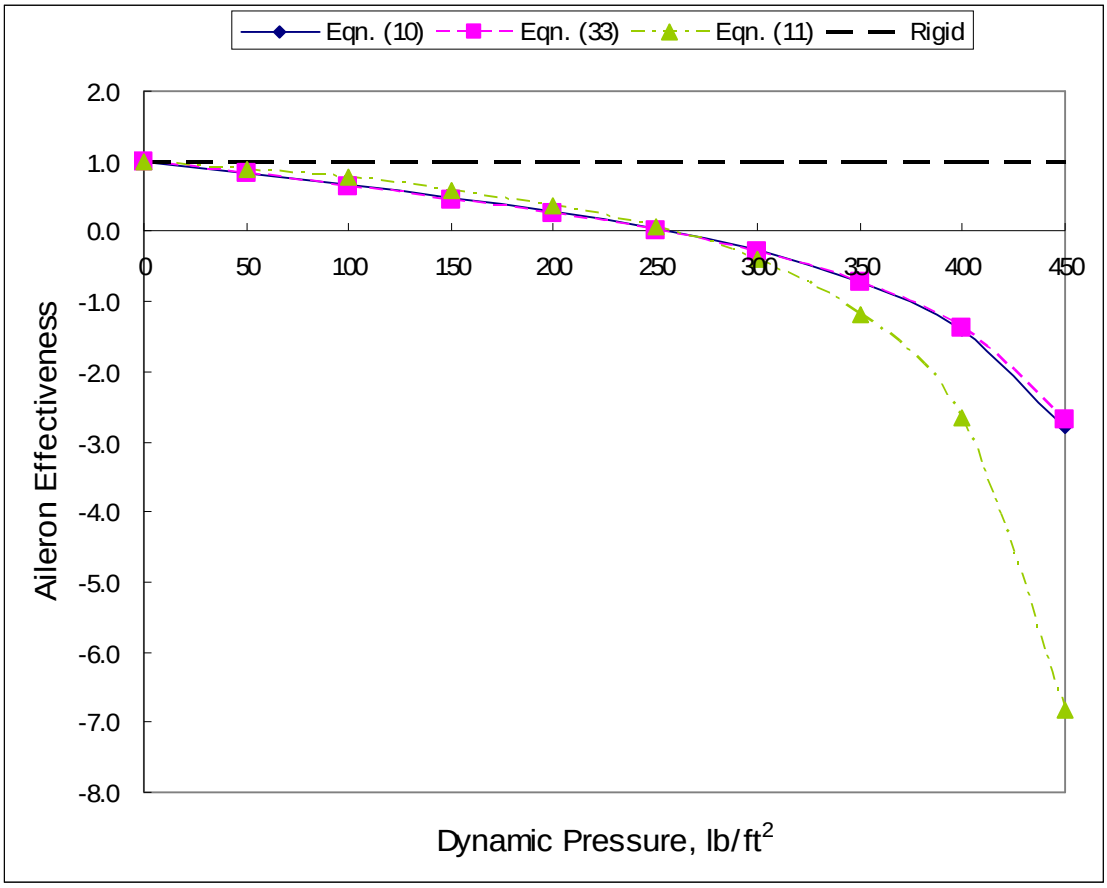

Figure 4.4: Comparisons of aileron effectiveness (without 3D effects)

The results for typical section from theory are less accurate, but it is a good reference to check aileron effectiveness. The results for total lift and root bending moment have good agreements with each other. Now focus on the plot with 3D effects, since the model is more practical and will be used in the following analyses. The result shows there is more than twice aileron effectiveness of rigid wing (though negative). If the high effectiveness happens before wing stall, this phenomenon can be used to develop highly maneuverable aircraft in the future.

To make certain the wing does not encounter stall, it is a good verification to check if the tip rotation is beyond the stall angle of attack during the entire range of operating

dynamic pressure in the above analyses. Indeed, the tip is structurally the most flexible part of the wing. If the tip rotation is not beyond the stall angle of attack, the model will not encounter the stall. Results with and without 3D effects are shown in Figure 4.5.

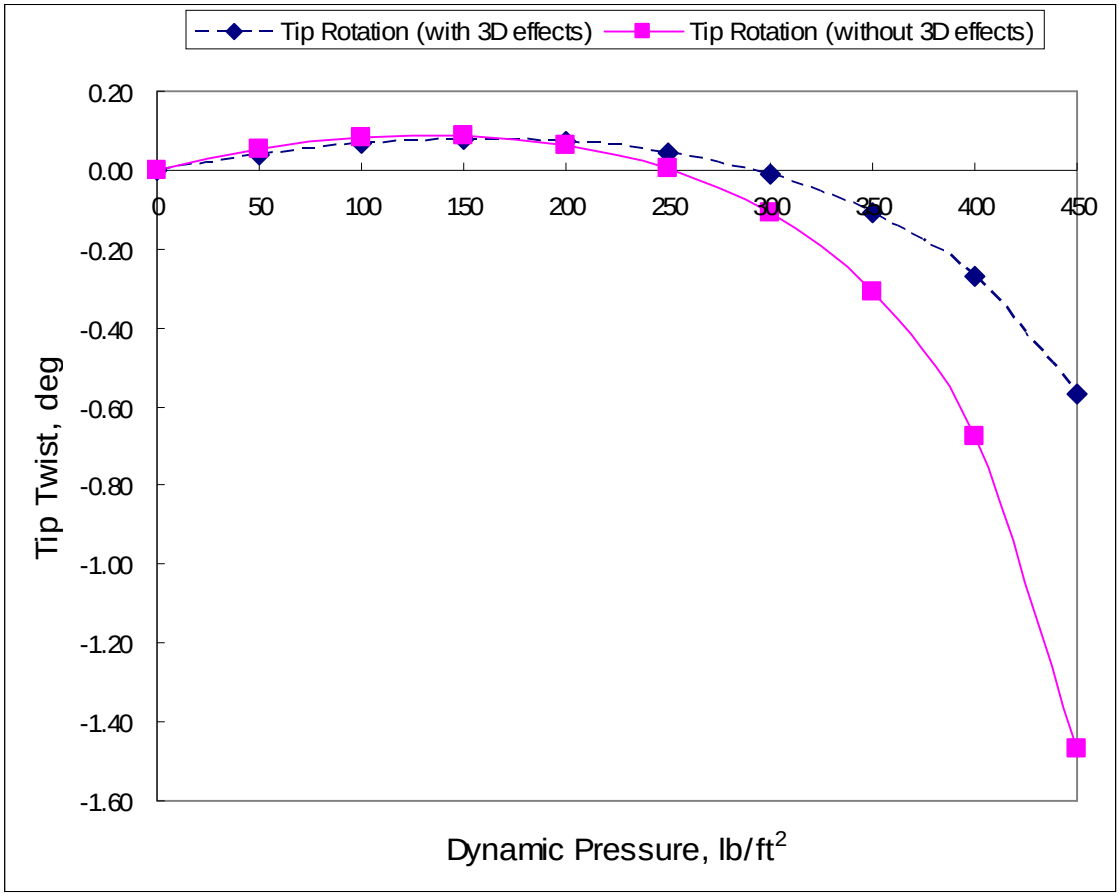

Figure 4.5: Tip Rotation for wing versus operating dynamic pressure

Three conclusions can be made from this plot. First, if the tip loss factor is not involved in the model, the tip rotation is higher than that involving the tip loss, due to more lift generated at the wing tip. This is consistent with the results shown in Figures 4.2 to 4.5. Higher negative lift is generated at the wing tip, and tended to generate higher bending moment at the wing root, and finally resulted in higher negative effectiveness. Next, the trends of the curves are similar to that for total lift. The reversal dynamic

pressure for the model without 3D effects is lower than that with 3D effects, and both of them located in the range from 250 to 300 lb/ft^2, which are consistent with the results shown in Table 4.1. Lastly and most importantly, the tip rotation is sufficiently small and is not beyond the stall angle of attack during the entire range of the operating dynamic pressure. Therefore, there exists a configuration that reverses at a relatively low dynamic pressure and flies with the enhanced controls at a higher level of effectiveness.

The case shown above is the cantilevered wing model given a flap angle β of 1 degree. Results show the model did not encounter stall for such a small aileron deflection. If the aileron deflection becomes sufficiently large, the wing may stall before it will actually reverse. On the other hand, large aileron deflection will influence aeroelastic phenomena as well due to more lift generated and larger flexibility effect. That being the case, the above model with 10-foot span is used to evaluate how aileron deflection affects aeroelastic phenomena and whether or not the wing will encounter stall. Figure 4.6 shows the relation between aeroelastic boundaries and aileron deflection. Note that the dashed lines show the aeroelastic boundaries versus aileron deflection for analytical results. As expected, the difference between numerical and analytical results is more for larger aileron deflection due to nonlinearity. The numerical results are got from a more sophisticated code which can capture more 3D effects. With increasing aileron deflection, the post-reversal regime shrank, and finally this regime is too narrow to address aeroelastic phenomena even though there may be high level of aileron effectiveness existing within it. That being the case, pilots are difficult to control aircraft at such a narrow regime of operating dynamic pressure. Therefore, it is not worthwhile to be investigated about the post-reversal behavior for the aircraft here.

For the cantilevered wing case, large aileron deflection influences divergence

dynamic pressure a lot, but it does not affect reversal dynamic pressure much. That is because effective camber increases with increasing aileron deflection, and tends to increase the lift-curve slope. In the meantime, more lift will be generated based on higher lift-curve slope at certain speed. By reviewing Eqn. (25), divergence dynamic pressure is inversely related to the lift-curve slope. The changes of lift-curve slope can be indirectly translate to the changes of total lift, so the trend for the variation of divergence dynamic pressure with respect to aileron deflection is close the curve shown as Figure 4.7.

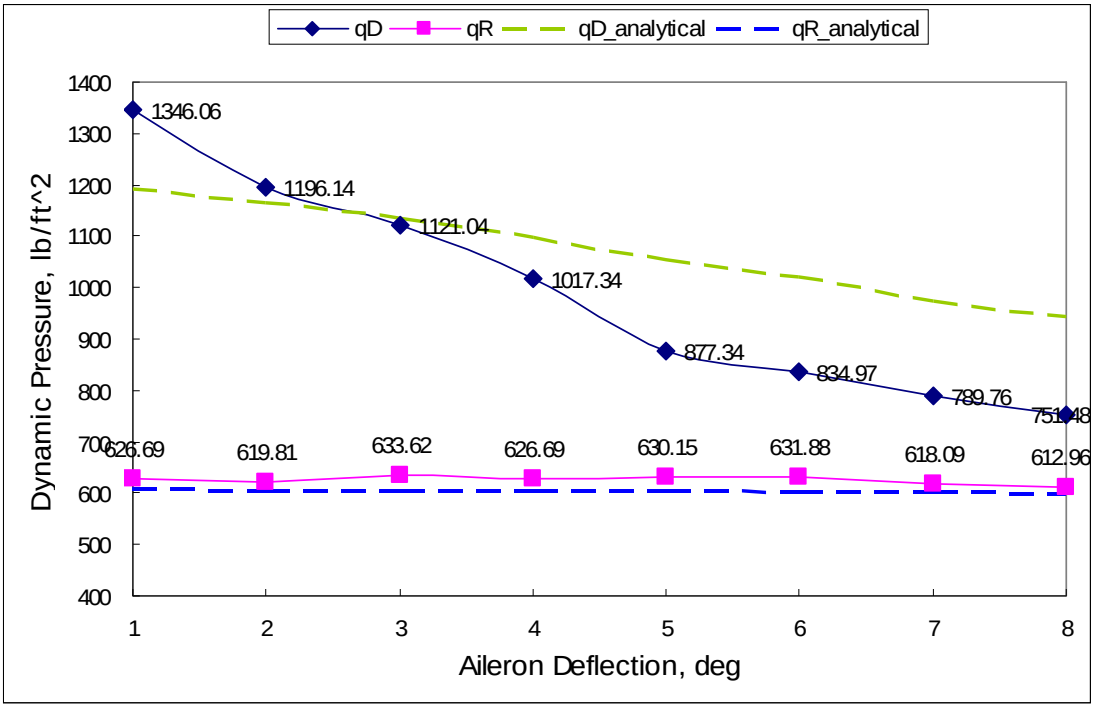

Figure 4.6: Aeroelastic boundaries versus aileron deflection (cantilevered wing)

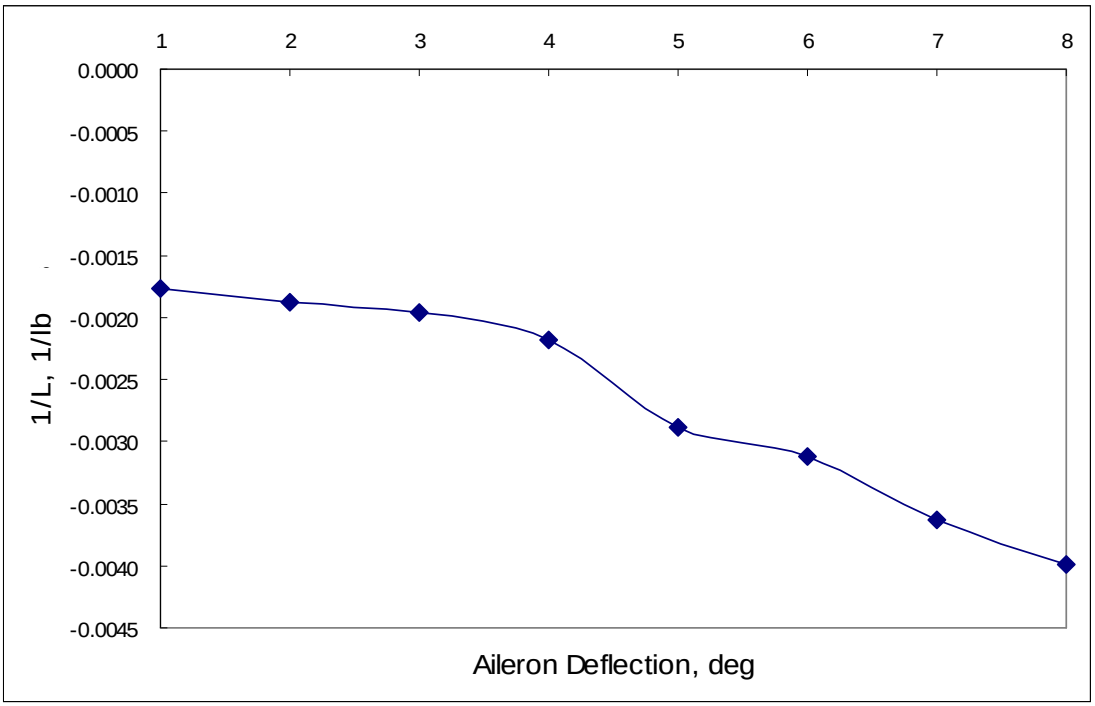

Figure 4.7: Inverse of total lift versus aileron deflection

To check if the wing encountered stall for the two cases, the maximum spanwise tip rotation during the operating dynamic pressure is reported in Figure 4.8. All of them are far below the stall angle of attack for NACA 0009. Therefore, the wing did not stall before it reversed, even after the reversal occurred.

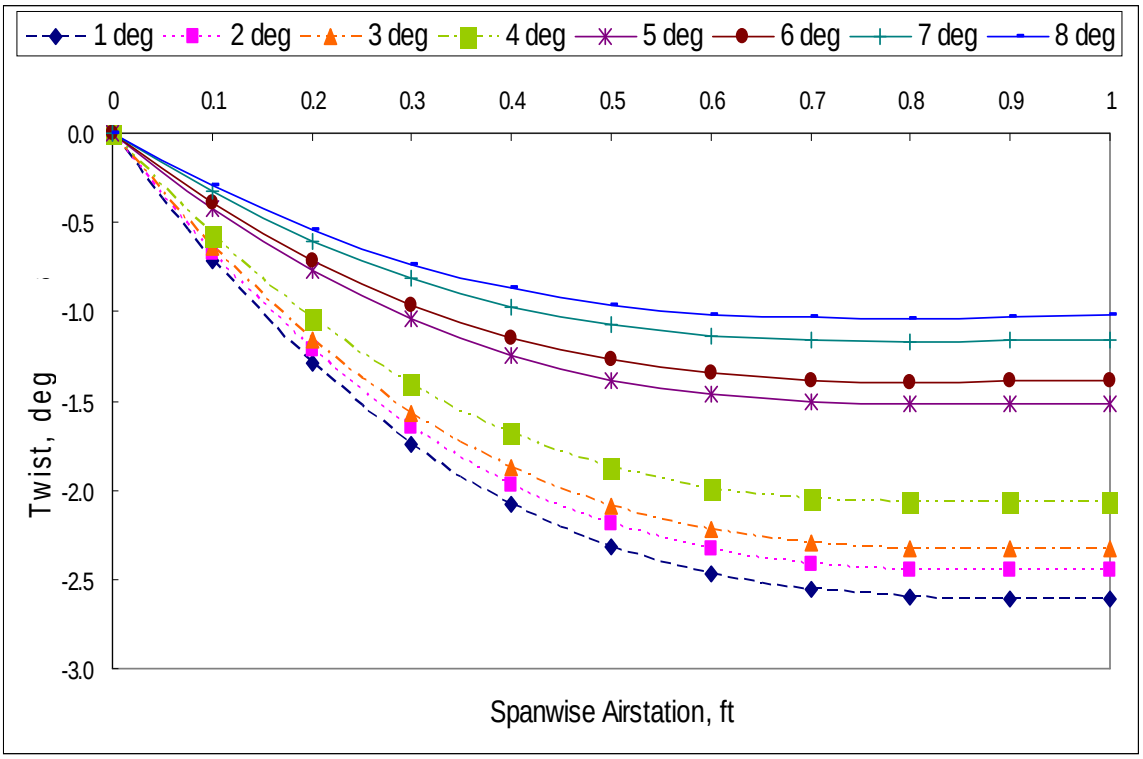

Figure 4.8: Spanwise tip rotation with varying aileron deflection

4.2 Aileron Reversal for a Rolling Aircraft

4.2.1 Aeroelastic Model

So far, aeroelastic analyses for the wing-aileron system have focused on uniform cantilevered lifting surfaces. Practical analyses must take consideration of a complete aircraft in flight, and that requires the vehicle is trimmed for the desired flight condition. That being the case, the complete aircraft with uniform wing-aileron system will be addressed in this section.

Consider an unswept rectangular wing with aileron of a rolling aircraft as illustrated in Figure 4.9. The wings are modeled as a beam and presumed to be built in at their root to represent attachment to a fuselage and free at their tip. The *y*-axis corresponds to the

elastic axis, which may be defined as the line of effective shear centers, assumed here to be straight. Because the primary concern here is determination of the airload distributions, the major elastic deformation that will influence these loads is twist about the elastic axis.

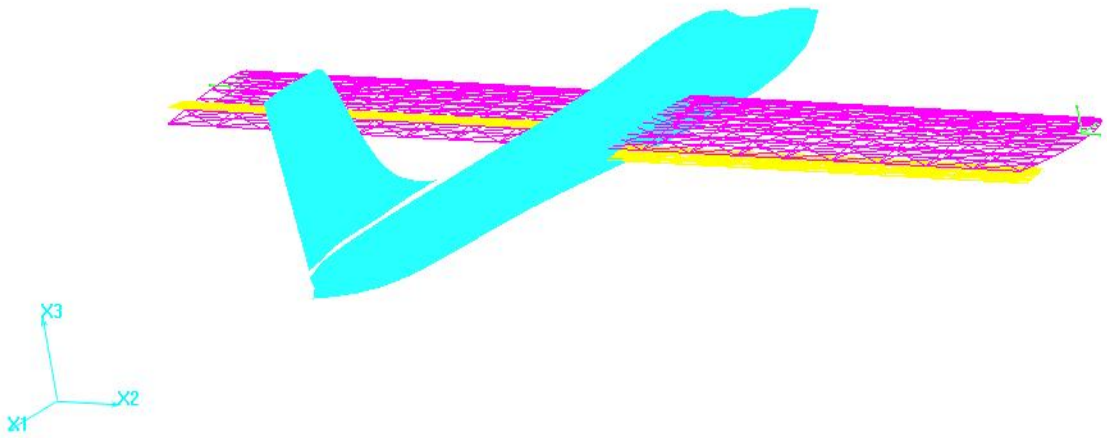

Figure 4.9: Configuration of the wing-aileron system for a rolling aircraft

As before, NACA 0009 airfoil is selected as the wing section of the rolling aircraft models. For the initial analyses, solid wing and isotropic material are used for the wing. DYMORE is used for the multibody dynamics analysis. This model is an aeroelastic problem dealing with the symmetry of a rectangular planform wing clamped at the fuselage of a flying aircraft shown in Figure 4.9. Due to symmetry, a half configuration is described as follows. The wing has a rectangular planform of length L_{span} = 12.5 ft and chord length c = 1 ft. The 12.5-foot aileron extends along the span of the whole wing, where the hinge location is at 80% chord of the main wing. The structural properties of the cantilevered wings are as follows: bending stiffness, $EI = 2.365\times10^5$, torsional stiffness, $GJ = 2.39\times10^4$ (both in lb-ft^2), mass per unit span, m = 0.0075 (slug/ft), polar moment of inertia, I = 0.0195 (slug-ft). The airfoil quarter-chord and center of mass are

located 0.084 ahead and 0.6 ft aft of the wing elastic axis, respectively. For F/A-18, there is total 400 ft^2 of wing area to provide lift to sustain 24,700 lb of empty weight (fuselage is around 10,000 lb). For the model with 25 ft^2 of wing area, the total weight of the fuselage is assumed to be 600 lb herein in order that the resulting lift can sustain the total weight of the aircraft. Note that the wing span is modeled with cubic beam elements [10, 11].

The aerodynamic model combines thin airfoil theory with a three-dimensional dynamic inflow model [91]. The airfoil with deflected trailing edge in XFOIL is used to generate the required aerodynamic coefficients to build up the airtable to be added into this model to specify the lift, drag, and moment coefficient for different Mach numbers and angles of attack. The inflow velocities at each span-wise location are computed using the finite state induced flow model developed by Peters et al. [91, 94]. As before, "6" is set as the number of inflow modes in DYMORE input to determine the number of harmonics for the states used for the solution over the inflow disk. When this number is used, DYMORE automatically uses "28" states of inflow model to compute the pressure difference for each airstation over the inflow disk. Ten airstations are used in all the models associated with the number of modes, "6", herein. Airloads are computed at 10 stations along the wing span, located at the positions corresponding to Gaussian quadrature.

4.2.2 Trim Analysis

Consider the rolling aircraft with unswept rectangular wings, and the roll rate is denoted by *p*. The entire aircraft must be modeled as Figure 4.9, since one wing is moving upward while the other is moving downward. Note that unlike the traditional

approach to achieve the trimmed configuration, the horizontal tail with a stabilizer is not included in the model. Although it is not realistic, the model is sufficient for trim analysis associated with antisymmetric behavior of an aircraft, especially searching for the steady roll rate about the short-term roll is the purpose of this study. The equilibrium equations of an aircraft with rectangular wings can be synthesized by symmetric and antisymmetric components. Aileron deflection primarily results in antisymmetric loadings [17]. Therefore, the problem can be posed in terms of symmetric and antisymmetric parts, and these two parts are not coupled to each other. The antisymmetric part can be treated separately because components that are the same on both sides of the aircraft cancel out in pure roll. For example, in the relation

$$\alpha = \alpha_r(y) + \theta(y) - \frac{py}{U} \tag{34}$$

where y represents spanwise location and the first term is the rigid angles of attack (including wing root's angle of attack and wing's built-in twist), and it can be drop out due to symmetry. The elastic twist of wings and the roll rate are antisymmetric, because θ and β will have the opposite sense across the mid-plane of the aircraft. The last term represents the increment in the angle of attack from the roll rate p. Thus Eqn. (34) becomes

$$\alpha = \theta(y) - \frac{py}{U} \tag{35}$$

The trim equation for a rolling maneuver consists of the wing's equations of equilibrium and the global equilibrium of the aircraft together with the governing equations for the elastic deformation of the wing and the aerodynamic modeling equations [48]. All of them are built into the DYMORE source code to do trim analyses.

Therefore, in light of the above, the force equilibrium applied in the trim analysis

here only includes the component along *z*-axis, which is simply total lift in the *z* direction equal to total weight of an aircraft for level flight

$$\sum F_z = L - W = 0 \tag{36}$$

Note that the components of force equilibrium along *x*- and *y*-axis are not considered in this analysis, which means the following force equilibrium equations are not involved in DYMORE models.

$$\begin{aligned} \sum F_x &= T - D = 0 \\ \sum F_y &= 0 \end{aligned} \tag{37}$$

where T is thrust and D is aerodynamic drag.

In addition, the moment equilibrium applied in the trim analysis here only includes the component along *x*-axis, which is rolling equilibrium equation. For a steady rolling condition resulting from a unit aileron deflection, three rolling moments due to aileron deflection, elastic twist, and roll rate must sum to zero, and that is

$$\sum M_x = M^e + M^\beta + M^p = 0 \tag{38}$$

where M^e represents the rolling moment caused by elastic twist, M^β represents the rolling moment caused by aileron deflection, and M^p represents the rolling moment caused by roll rate. Similarly, the components of moment equilibrium along *y*- and *z*-axis are not considered in this analysis, and they are pitching moment equilibrium and yawing moment equilibrium.

$$\begin{aligned} \sum M_y &= 0 \\ \sum M_z &= 0 \end{aligned} \tag{39}$$

Note that although it is not realistic not to consider all force and moment equations of equilibrium, the model is sufficient for trim analysis associated with searching for the

steady roll rate about the short-term roll.

Assuming there is no structural coupling and using the operator notation, the matrix form of equations for the equilibrium of the wing can be written as

$$\begin{aligned} \{w\} &= \left[C^{ww}\right]\{F\} \\ \{\theta\} &= \left[C^{\theta\theta}\right]\{M_{ea}\} \end{aligned} \tag{40}$$

where [*C*] is a matrix of influence coefficients representing the response of the structure. The matrix form of aerodynamic formulation can be written as

$$\{\alpha\} = \left[\mathrm{A}_a^{-1}\right]\{cc_l\} \tag{41}$$

where $\{cc_l\}$ is a matrix of influence coefficients representing the applied force or moment due to aerodynamics related to deflection, such as angle of attack.

The problem of trim in this dissertation involves the determination of the correct control settings that satisfy some desired operational conditions with initially 1 degree of angle of attack. The auto-pilot and discrete auto-pilot methods [90] are well suited for the solution of the trim configuration when the problem is formulated using this finite element based multibody dynamics analysis, DYMORE. The auto-pilot method continuously modifies the controls so that the system converges to a trimmed configuration. The discrete auto-pilot approach modifies the control setting at each revolution only.

In the present study, for antisymmetric unit degree of β, the zero roll rate is set as the desired operational condition (control output) to determine the operating aircraft speed (control input). The auto-pilot trimming is performed in three steps: reference run, perturbation run and simulation run. First, in the reference run, the finite element based

multibody code is run till the target values stabilized using a set of prescribed aileron deflection settings. Then, the perturbation run was performed in which the control input is perturbed. Finally, in the simulation run, the control input is updated for dynamic simulation based on the auto-pilot control law, till the output converged to desired value. The initial value of operating aircraft speed is 50 ft/sec; the target value of roll rate is $p = 0$. During the perturbation run, the operating aircraft speed is perturbed by 25 ft/sec for each iteration. At convergence, the roll rate is approaching zero, with ± 0.02% error compared to the desired value. Table 4.2 lists the trim angles of attack for different trimmed configuration associated with different flying speeds. Results show all the angles of attack are below the stall angle of attack for NACA 0009 airfoil. In addition, as the flying speed increases, the lift increases. Due to the force equilibrium about z direction, the angle of attack decreases with increasing flying speed.

Table 4.2: Trim angle of attack versus nondimensional dynamic pressure

q/q_D	0.1	0.2	0.3	0.4	0.5	0.6
AOA, deg	3.948	3.352	2.816	2.325	1.865	1.425

For trim analysis, the various components of the rolling moment must all sum to zero during the entire operating dynamic pressure. The rolling moment consists of the component caused by the elastic twist, the roll rate, and the aileron deflection. Particularly, at the point of control reversal, the component of the rolling moment caused by the roll rate vanishes. Therefore, for the antisymmetric unit degree of β, the zero roll rate is set as the desired operational condition to determine the operating aircraft speed. Note that the speed can be interpreted as the dynamic pressure with the constant air density. Results for different components of the rolling moment versus the

nondimensional operating dynamic pressure (normalize operating dynamic pressure by divergence dynamic pressure) are shown in Figure 4.10. The rolling moment caused by the roll rate vanishes at the dynamic pressure equal to 127.3 lb/ft^2, which means that the roll rate vanishes. This condition is the so-called the control reversal for the aircraft. During the post-reversal regime but before divergence, a much higher rolling moment caused by the roll rate is generated, although it has the opposite sense with that of operating the aircraft in the conventional regime. That means a flying aircraft can achieve higher roll rate during this regime to do a rolling maneuver. This phenomenon may be used to develop the highly maneuverable aircraft, especially the fighter aircraft. To demonstrate this phenomenon, more practical cases will be investigated in Section 4.2.4. Before that, maneuverability for an aircraft is discussed in next section.

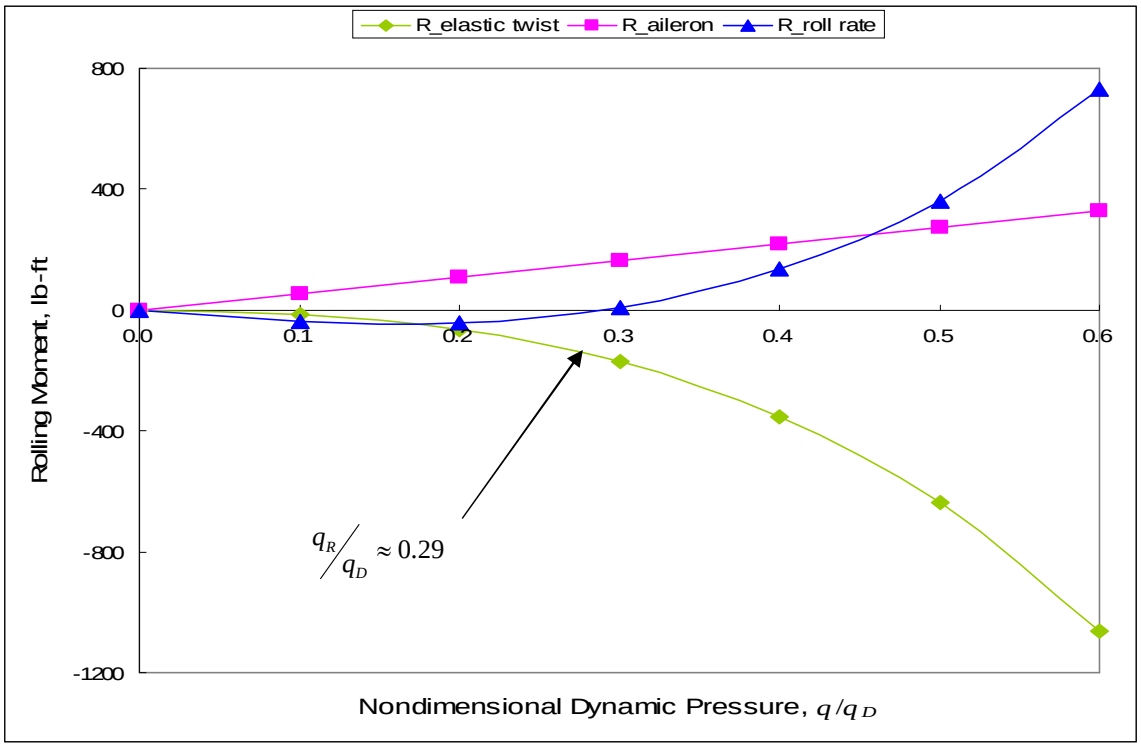

Figure 4.10: Variation of the components of the rolling moment versus nondimensional operating dynamic pressure

4.2.3 Maneuverability

Enhancement of roll maneuverability for the aircraft requires the pilot to be able to achieve maximum rolling of the aircraft by deflecting trailing-edge control surfaces antisymmetrically. The aileron system increases the lift on one wing and decreases lift on the other one, and tends to provide a rolling moment for the rolling maneuver. The primary function of this control is to produce a rolling moment. The effectiveness of the ailerons in producing rolling moments is described by the control derivative $\partial M_r / \partial \beta_a$, where M_r is rolling-moment. The flap angle β_a is defined as the mean value of the magnitudes for the aileron deflection on both sides of the fuselage [34]. Note that since the same magnitude of the aileron deflection is given for the ailerons on both sides in the models herein, $\beta_a = \beta$ and the control derivative can be simplified as $\partial M_r / \partial \beta$. It is positive when the right aileron deflection is downward. The derivative $\partial M_r / \partial \beta$ is normally positive, right aileron down producing a roll to the left. However, if the high performance aircraft is operating at high dynamic pressure where deformation of the wing is significant, the roll rate is reduced as shown in Figure 4.11 by a detrimental aerodynamic twisting moment produced by the trailing-edge control surface rotation. A roll reversal dynamic pressure, at which the aileron system is rendered completely ineffective for producing roll rate for an aircraft, can be determined.

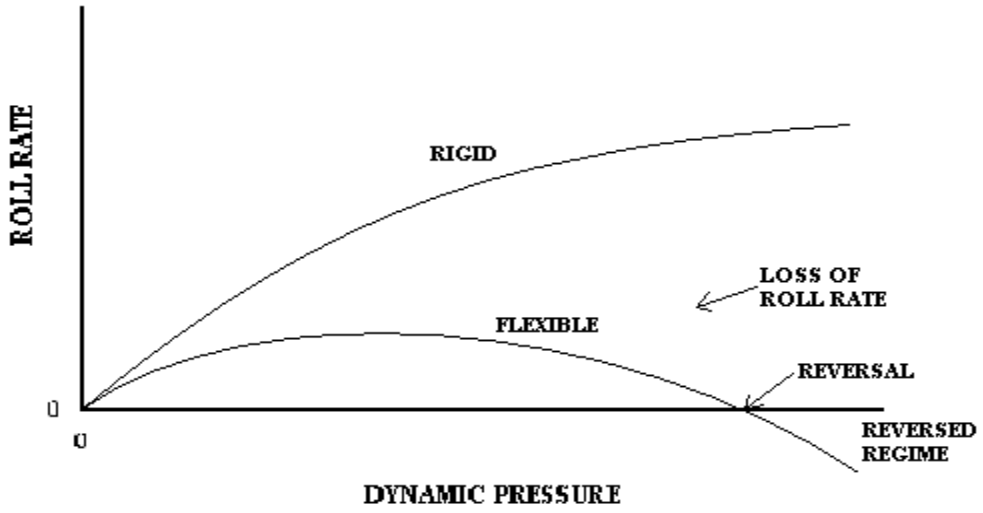

Figure 4.11: Loss of roll rate due to wing flexibility

Same as the cantilevered wing model, to determine the maneuverability of the flying aircraft, the effects of large aileron deflection are evaluated first. Using the rolling aircraft model with 10-foot span and given antisymmetric aileron deflection, results for the deflection up to 4 degree are reported in Figure 4.12. Note that the dashed lines show the aeroelastic boundaries versus aileron deflection for analytical results, and the difference between numerical and analytical results is due to numerical results are got from a more sophisticated code which can capture more 3D effects. With increasing aileron deflection, divergence dynamic pressure decreases, which means the potential of aeroelastic instability increases. That is because effective camber increases with increasing aileron deflection, and tends to increase the lift-curve slope. Meanwhile more lift will be generated based on higher lift-curve slope at certain speed. Indeed, by reviewing Eqn. (25) again, divergence dynamic pressure is inversely related to the lift-curve slope.

On the other hand, reversal dynamic pressure increases while aileron deflection

increases. Effective camber increases with increasing aileron deflection, and tends to increase both C_{L_β} and C_{M_β} shown as Figure 4.13. The slope for C_{L_β} curve is higher than that for C_{M_β} curve, which means the pure aerodynamic lift due to aileron deflection increases faster than the decreasing of aeroelastic lift due to aileron deflection. In other words, the negative aeroelastic lift is more difficult to overpower the pure aerodynamic lift with increasing aileron deflection. By reviewing Eqns. (29) and (30), the associated parameters to calculate the reversal dynamic pressure for the analytical results are plotted as Figure 4.14. All the three parameters increase with the increasing aileron deflection, and tend to increase the reversal dynamic pressure. Although nonlinear analysis is used for the model in this section, the variation of all aerodynamic coefficients and the associated parameters is small. Therefore, the reversal dynamic pressure increases almost linearly as aileron deflection increases. Note that the reversal here represents the roll rate of a flying aircraft vanishes.

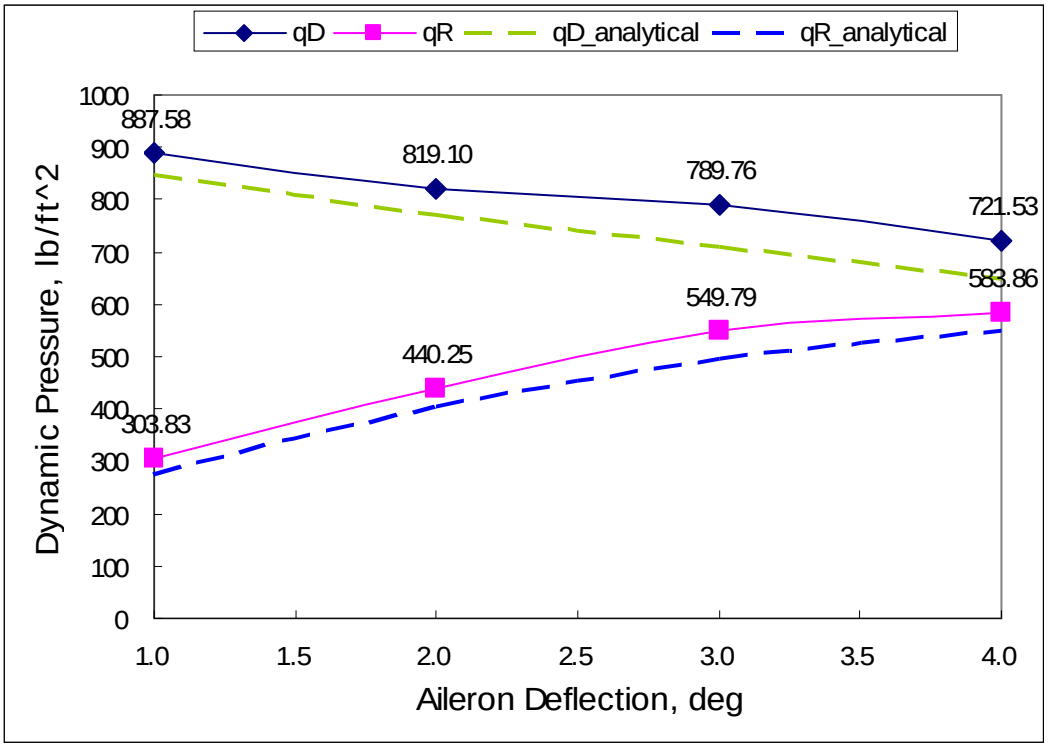

Figure 4.12: Aeroelastic boundaries versus aileron deflection (rolling aircraft)

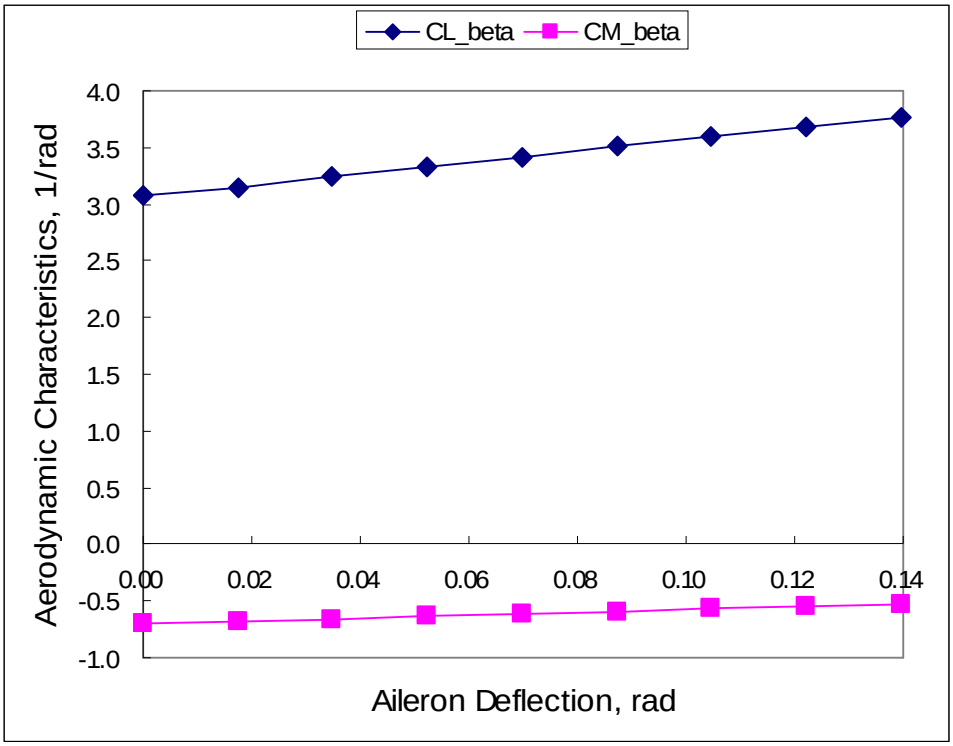

Figure 4.13: Variation of C_{L_β} and C_{M_β} versus aileron deflection

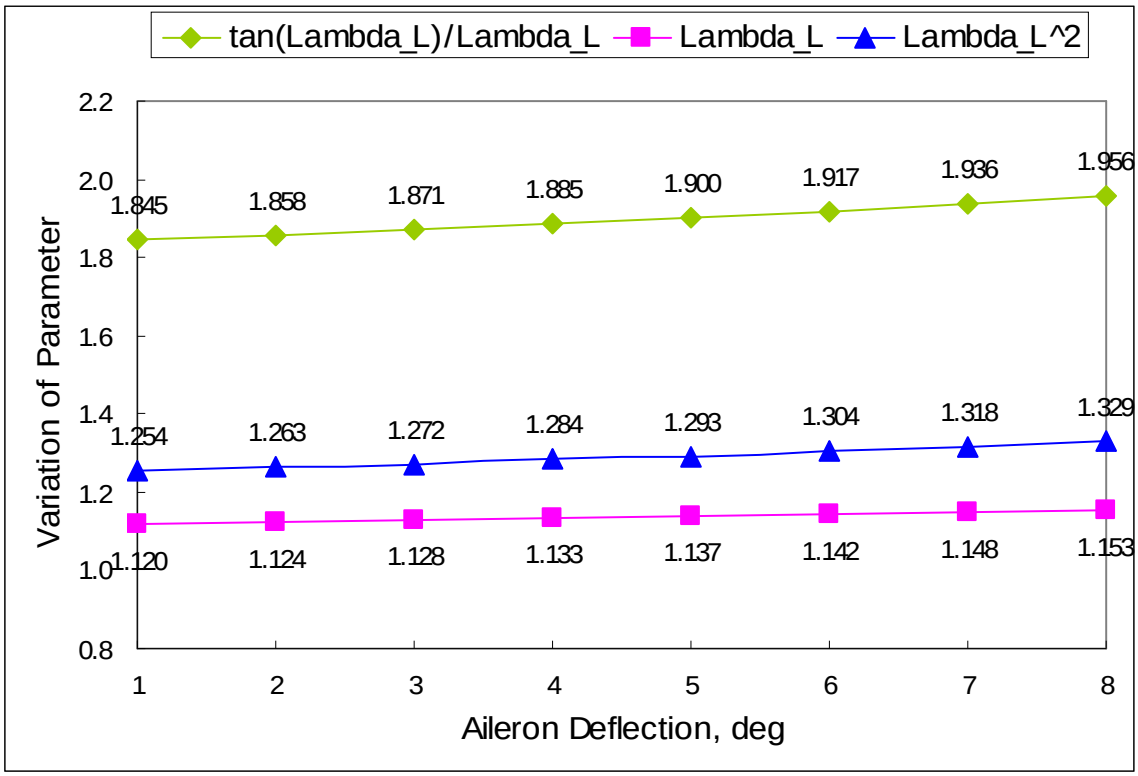

Figure 4.14: Variation of parameters in Eqn. (29) versus aileron deflection

Next, to predict the aeroelastic boundaries of the flying aircraft in Section 4.2, different combinations of flight conditions will be investigated. The major factor affecting the flight conditions is the operating altitude. Changing the altitude, the temperature and the air density will change as well as the speed of sound [5]. For the same free stream velocity, increasing the altitude will decrease the temperature, which tends to decrease the speed of sound, and finally Mach number decreases. On the other hand, for the same freestream velocity, increasing the altitude will decrease the air density and the temperature, and Reynolds number will change as well. Mach number and Reynolds number are the major factors to influence the composition of the airtable in the DYMORE model. Here the altitude from sea level to 30,000 feet, Mach number up to 0.72, and Reynolds number up to 15 million are investigated. Different combinations of

these three factors are evaluated to determine to divergence and reversal boundaries for a flying aircraft with the aspect ratio equal to 15.

First, Figure 4.15 shows the variations of aeroelastic boundaries versus Mach number by keeping Reynolds number constant. Both divergence and reversal dynamic pressures decrease with increasing Mach number. The wider post-reversal range can be taken advantage of for lower Mach numbers.

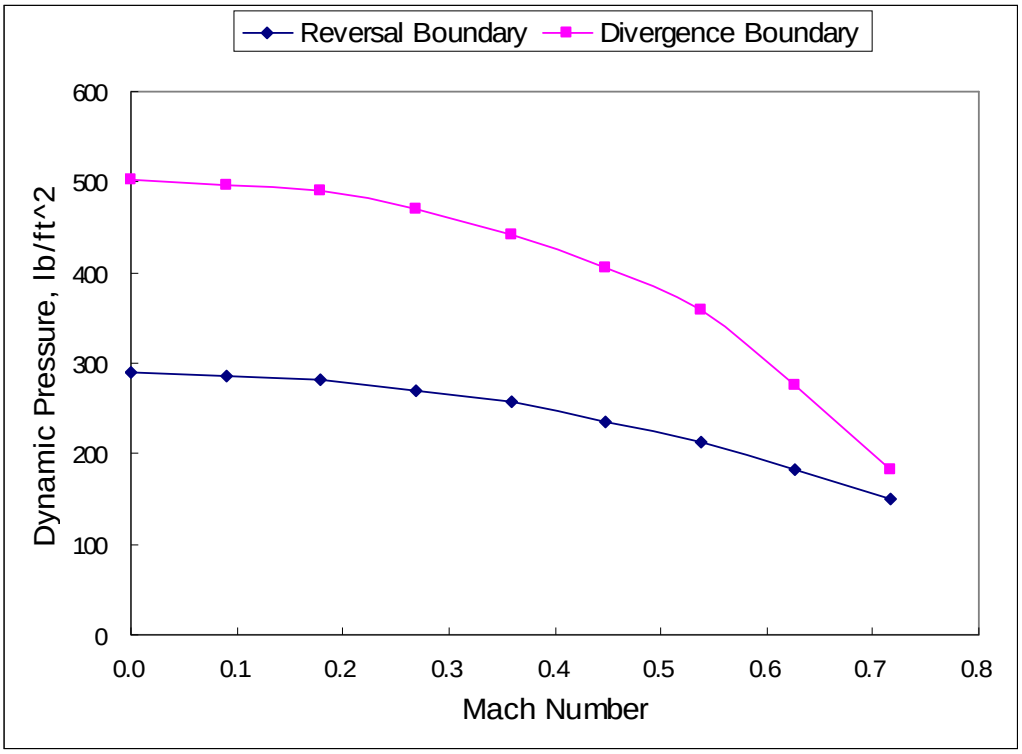

Figure 4.15: Aeroelastic boundaries of a flying aircraft at sea level with *Re* = 6,000,000

Next, Figure 4.16 shows the variations of aeroelastic boundaries versus Reynolds number by keeping Mach number constant. Divergence dynamic pressures increase with increasing Reynolds number, but there is almost no change for reversal dynamic pressure. Thus, the wider post-reversal range can be taken advantage of for higher Reynolds numbers.

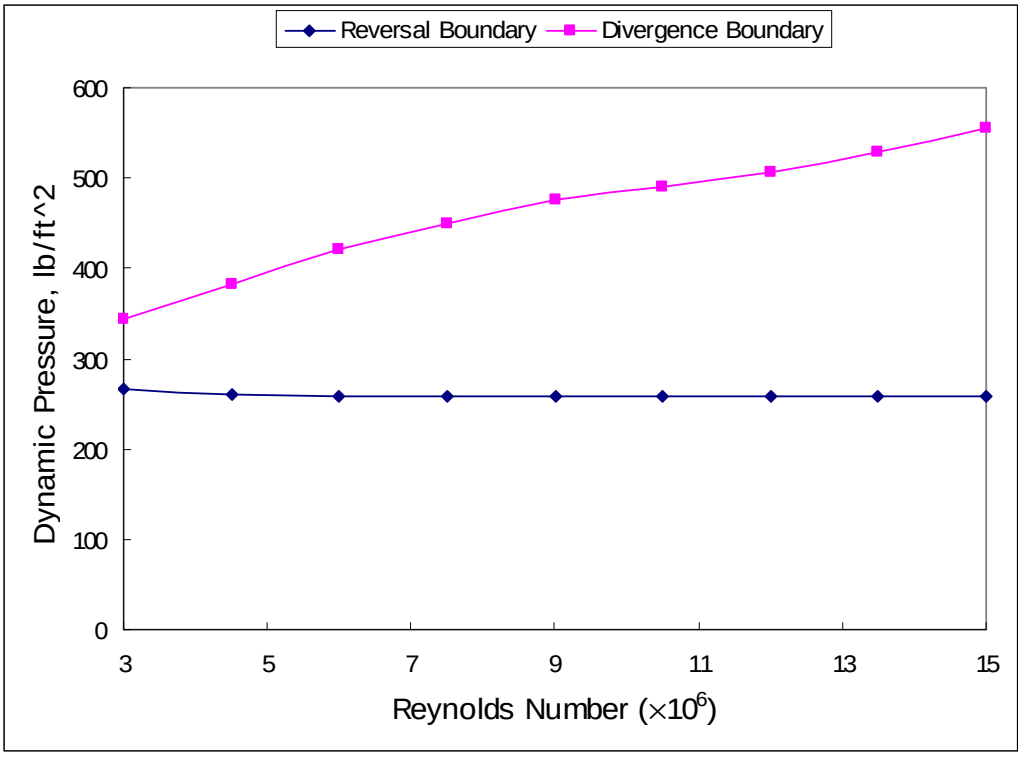

Figure 4.16: Aeroelastic boundaries of a flying aircraft at sea level with $M_\infty = 0.36$

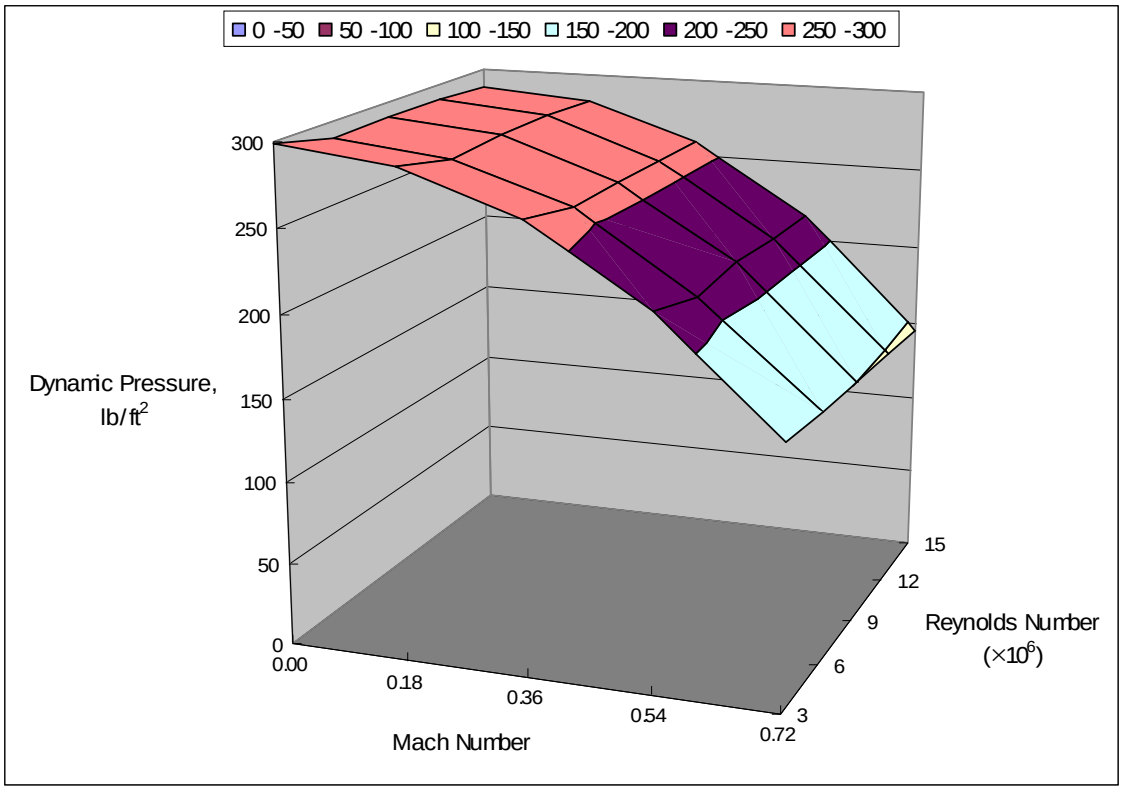

Figure 4.17: Reversal boundary of a flying aircraft at sea level

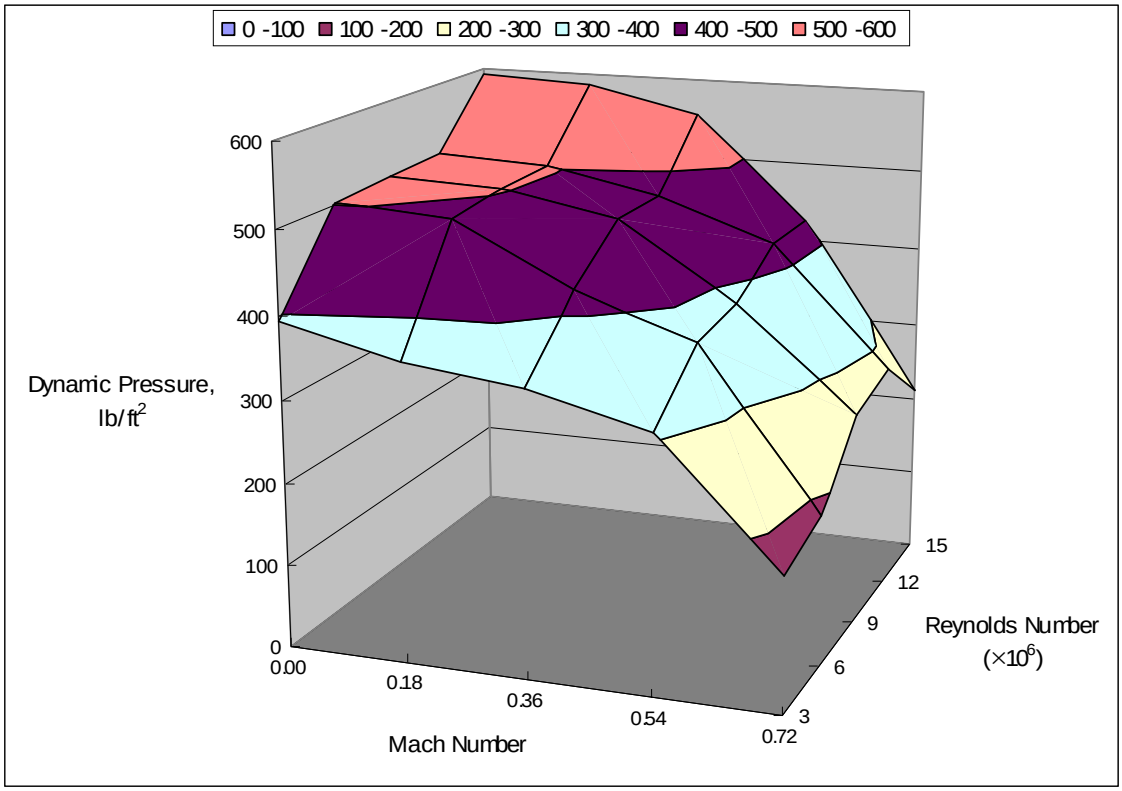

Figure 4.18: Divergence boundary of a flying aircraft at sea level

Figures 4.17 and 4.18 show the 3D plots with the relations between aeroelastic boundaries, Mach number, and Reynolds number. Reversal dynamic pressure almost keeps constant by varying Reynolds numbers, but decreases with increasing Mach number. For divergence dynamic pressure, there is a dramatic drop while Mach number increases and Reynolds number decreases. To explain the phenomena, the characteristics of airfoil in different Mach numbers and Reynolds numbers should be discussed from an aerodynamic point of view. The important factors to influence the divergence and reversal are lift-curve slope with respect to angle of attack and moment-curve slope with respect to aileron deflection, which are C_{L_α} and C_{M_β}, respectively. C_{L_α} represents how lift is generated and how quickly it is generated with respect to changes in angle of attack. C_{M_β} represents how aeroelasticity affects the model and how much angles of attack

decrease with wing flexibility.

Table 4.3: The variation of C_{L_α} versus Mach and Reynolds numbers

		Reynolds Number (×10^6)				
		3.0	**6.0**	**9.0**	**12.0**	**15.0**
Mach Number	**0.00**	6.24	6.31	6.33	6.35	6.37
	0.18	6.36	6.45	6.48	6.51	6.53
	0.36	6.86	6.99	7.04	7.08	7.11
	0.54	8.00	8.21	8.05	7.99	8.02
	0.72	9.85	9.81	10.20	10.59	10.58

Table 4.4: The variation of C_{M_β} versus Mach and Reynolds numbers

		Reynolds Number (×10^6)				
		3.0	**6.0**	**9.0**	**12.0**	**15.0**
Mach Number	**0.00**	-0.33	-0.32	-0.32	-0.32	-0.32
	0.18	-0.34	-0.33	-0.32	-0.32	-0.32
	0.36	-0.36	-0.34	-0.33	-0.34	-0.33
	0.54	-0.38	-0.34	-0.36	-0.36	-0.36
	0.72	-0.42	-0.40	-0.40	-0.41	-0.41

Table 4.3 shows the data from XFOIL for the model with NACA 0009 airfoil and given zero aileron deflection, and obviously lift-curve slope with respect to angle of attack increases with the increasing of Mach number. From surfaces pressure distribution shown in XFOIL, the difference of pressure distribution between upper surface and lower

surface of airfoil is getting larger with increasing Mach number, which tends to create more lift. Higher lift increasing quickly tends to lower the aeroelastic boundary. However, there is a nonlinear variation of C_{L_α} with respect to Reynolds number. Indeed, lift-curve slope is not influenced by Reynolds number much, but the maximum value of lift coefficient, which is governed by viscous effects, is dependent on Reynolds number. Reynolds number is a parameter that governs the strength of inertia forces relative to viscous forces in the flow and is dependent upon the freestream fluid density, velocity, and viscosity [4]. It would be difficult to check the sensitivity of lift-curve slope to Reynolds number if all the parameters above are not considered carefully. More details will be discussed later.

Table 4.4 shows the data from XFOIL for NACA 0009 airfoil with hinge location at 80% chord and given one degree of aileron deflection. The magnitude of moment-curve slope with respect to aileron deflection increases with Mach number, and thus increasing the aeroelastic sensitivity of the model. On the other hand, there is no significant change of C_{m_β} with respect to Reynolds number since the moment coefficient is relatively insensitive to Reynolds number in the linear regime. Therefore, the reversal boundary is more sensitive to Mach number due to the variations of the aeroelastic effect. To accurately describe the post-reversal regime, both divergence and reversal dynamic pressures are transformed to divergence and reversal speeds at sea level and shown in Figures 4.19 and 4.20.

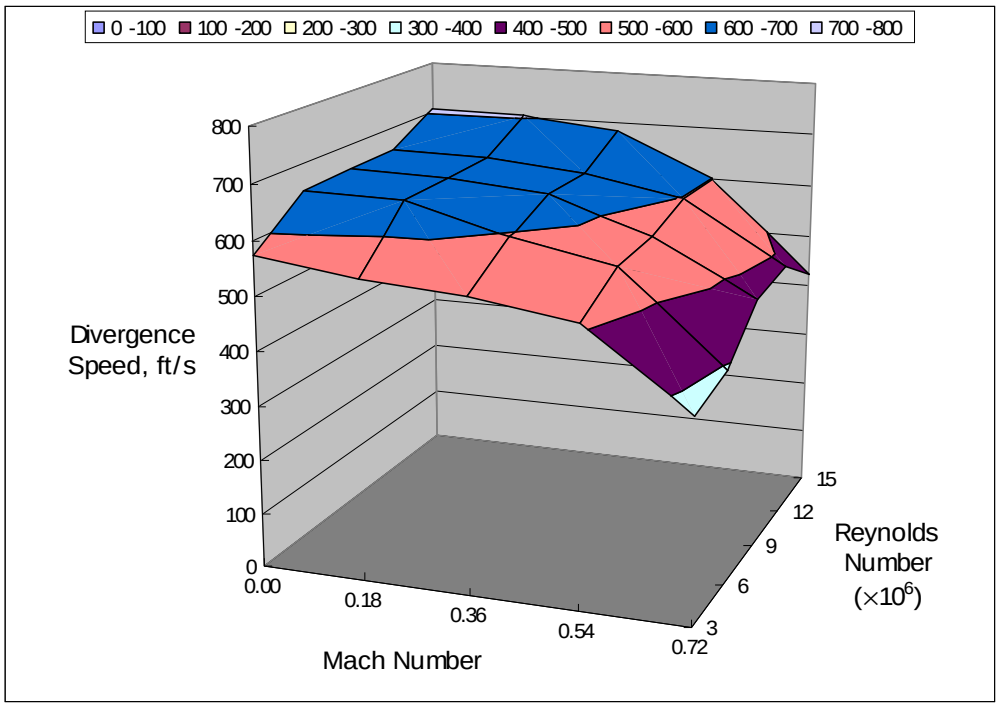

Figure 4.19: Divergence speed of a flying aircraft at sea level

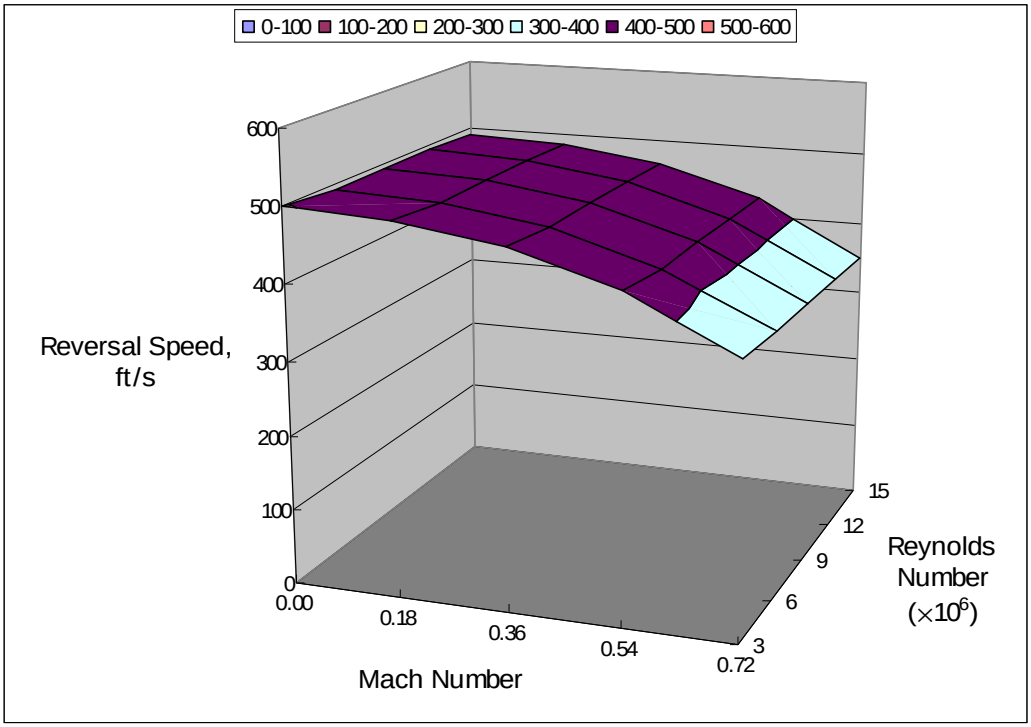

Figure 4.20: Reversal speed of a flying aircraft at sea level

If the aircraft is operated at 30,000 feet altitude, the variations of aeroelastic boundaries versus Mach number and Reynolds number are shown as Figures 4.21 and 4.22, respectively. Comparing with Figures 4.15 and 4.16, there are similar trends for both boundaries at different altitudes, but the post-reversal regime has shrunk at 30,000 feet altitude. That means a smaller post-reversal regime can be utilized at higher altitude. Note that the density is assumed to be constant within these comparisons, which means Reynolds number is not the real one at the specific altitude. Reynolds number equal to six millions is used in both Figures 4.15 and 4.21, although they represented the analyses at the different altitudes. The approaches here are easy to investigate the relations between the aeroelastic boundaries, Mach number, and Reynolds number. The real case under standard atmosphere will be discussed at the end of this section.

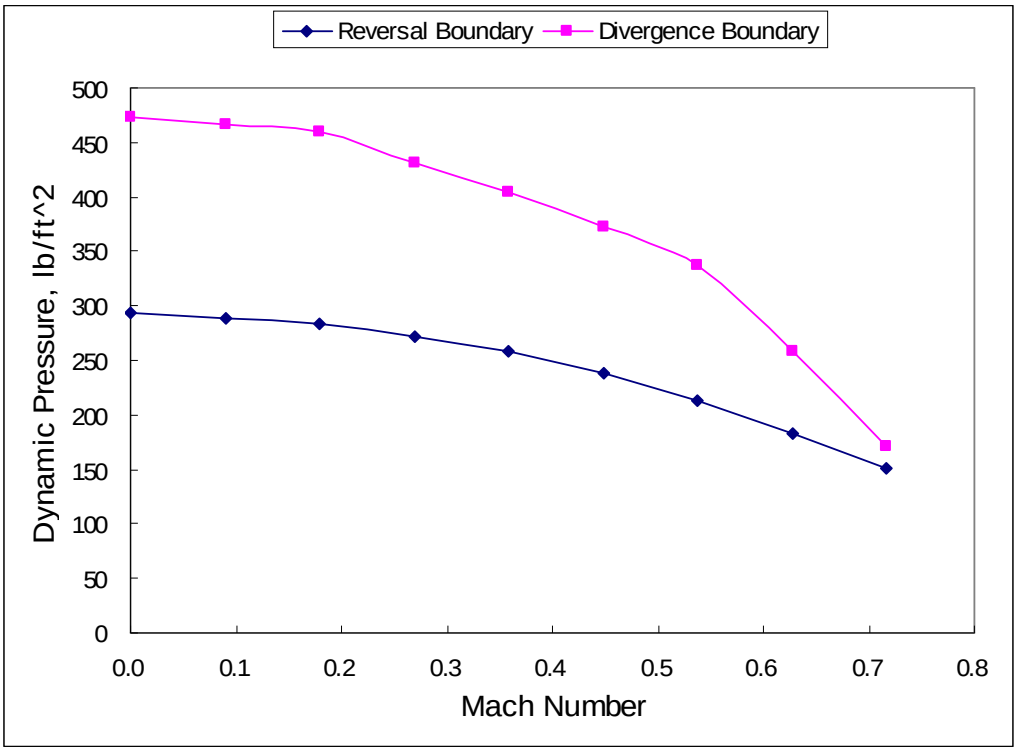

Figure 4.21: Aeroelastic boundaries of a flying aircraft at 30,000 ft with *Re* = 6,000,000

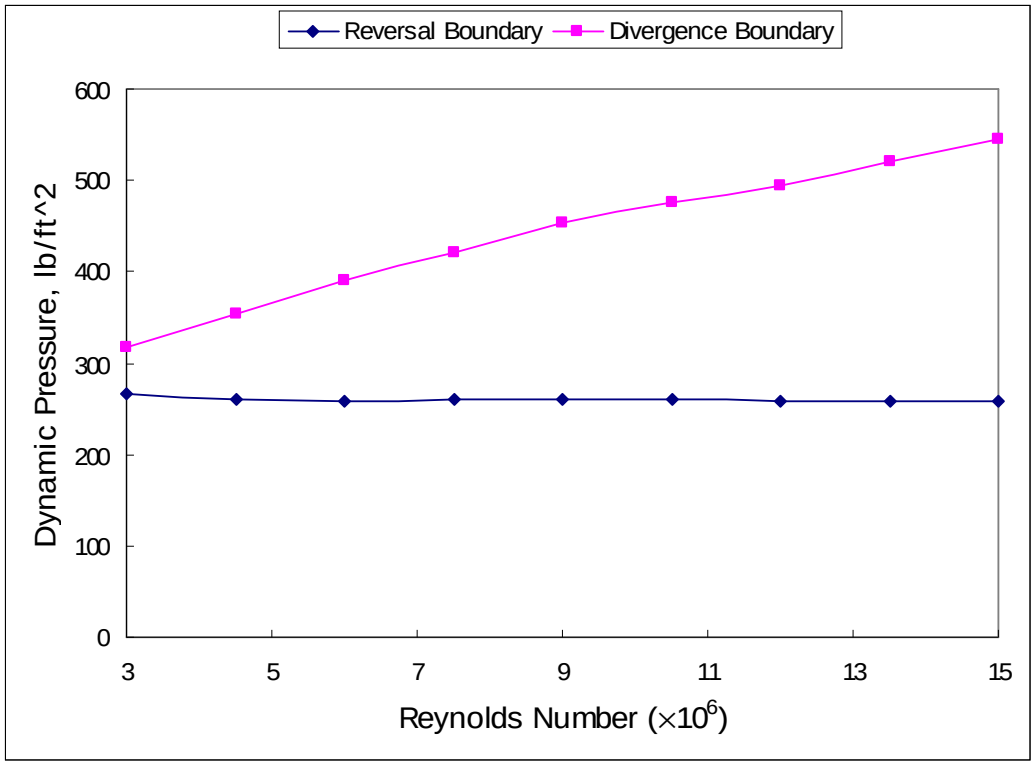

Figure 4.22: Aeroelastic boundaries of a flying aircraft at 30,000 ft with $M_\infty = 0.36$

Figures 4.23 and 4.24 show the 3D plots with the relations between aeroelastic boundaries, Mach number, and Reynolds number. Same as before, reversal dynamic pressure almost keeps constant by varying Reynolds numbers, but decreases with increasing Mach number. For divergence dynamic pressure, there is a dramatic drop while Mach number increases and Reynolds number decreases due to higher lift-curve slope, which is inversely related to the divergence dynamic pressure.

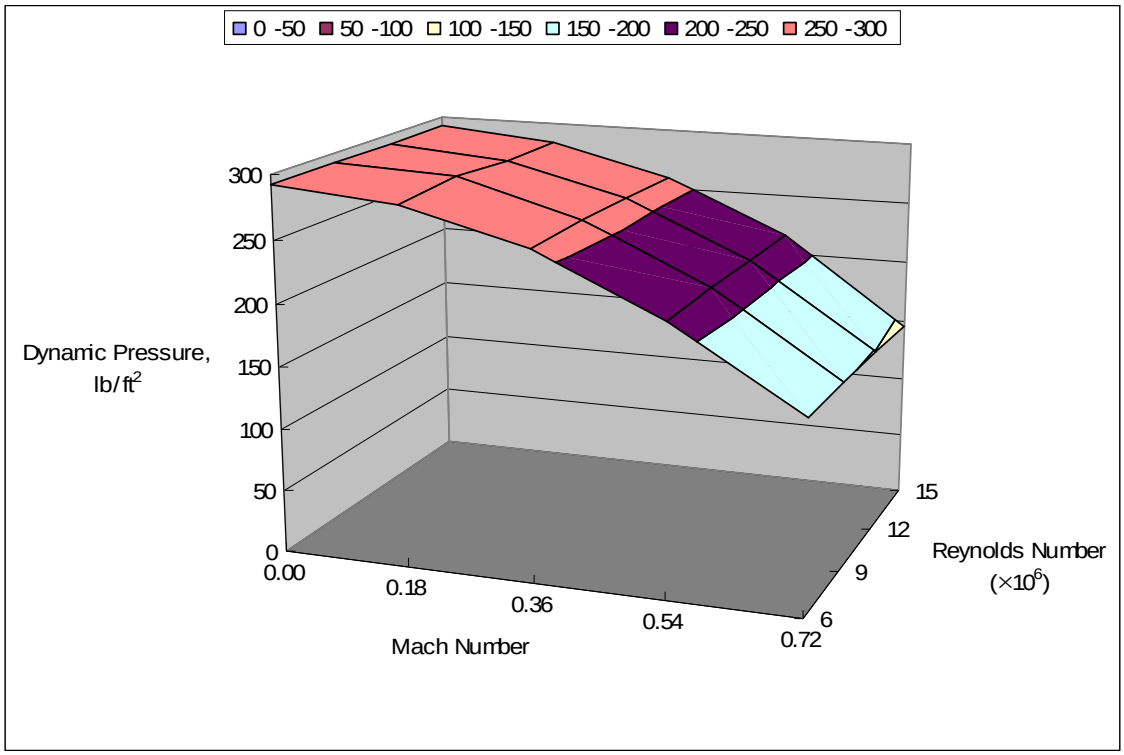

Figure 4.23: Reversal boundary of a flying aircraft at 30,000 ft

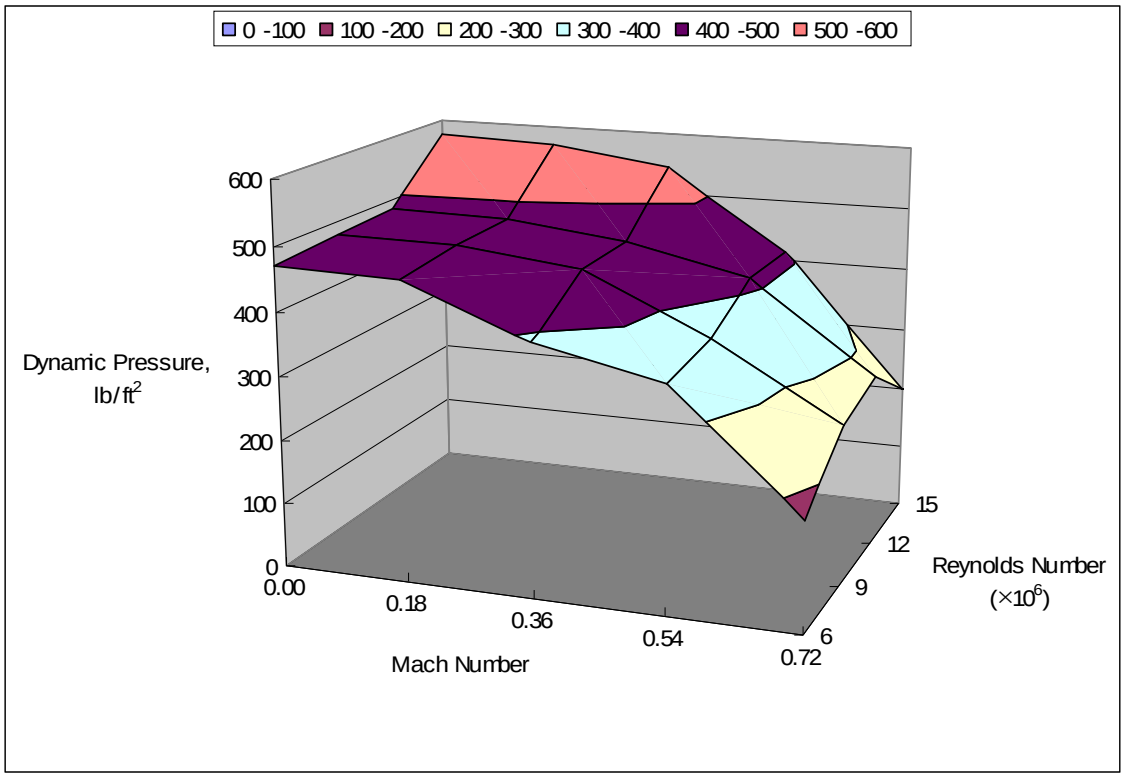

Figure 4.24: Divergence boundary of a flying aircraft at 30,000 ft

The influence of the altitude on the aeroelastic boundaries may be ascertained from the results recorded in Table 4.5. Obviously, with constant density assumption, there is no significant change in the reversal dynamic pressure when the altitude is varied. On the other hand, divergence dynamic pressure is sensitive to the altitude, which means it is sensitive to the flight condition. Therefore, the post-reversal regime decreases 19.6% from sea level to 30,000 feet, although the reversal dynamic pressure is not affected by the altitude directly.

Table 4.5: The variation of aeroelastic boundaries with respect to the altitude (M_∞ = 0.36, Re = 6,000,000)

		Altitude (ft)						
		Sea Level	**5000**	**10000**	**15000**	**20000**	**25000**	**30000**
Dynamic Pressure (lb/ft^2)	**Reversal**	258	258	258	258	257	260	259
	Divergence	421	421	418	414	407	399	390

As before, to accurately describe the post-reversal regime, both divergence and reversal dynamic pressures are transformed to divergence and reversal speeds at 30,000 feet and shown in Figures 4.25 and 4.26.

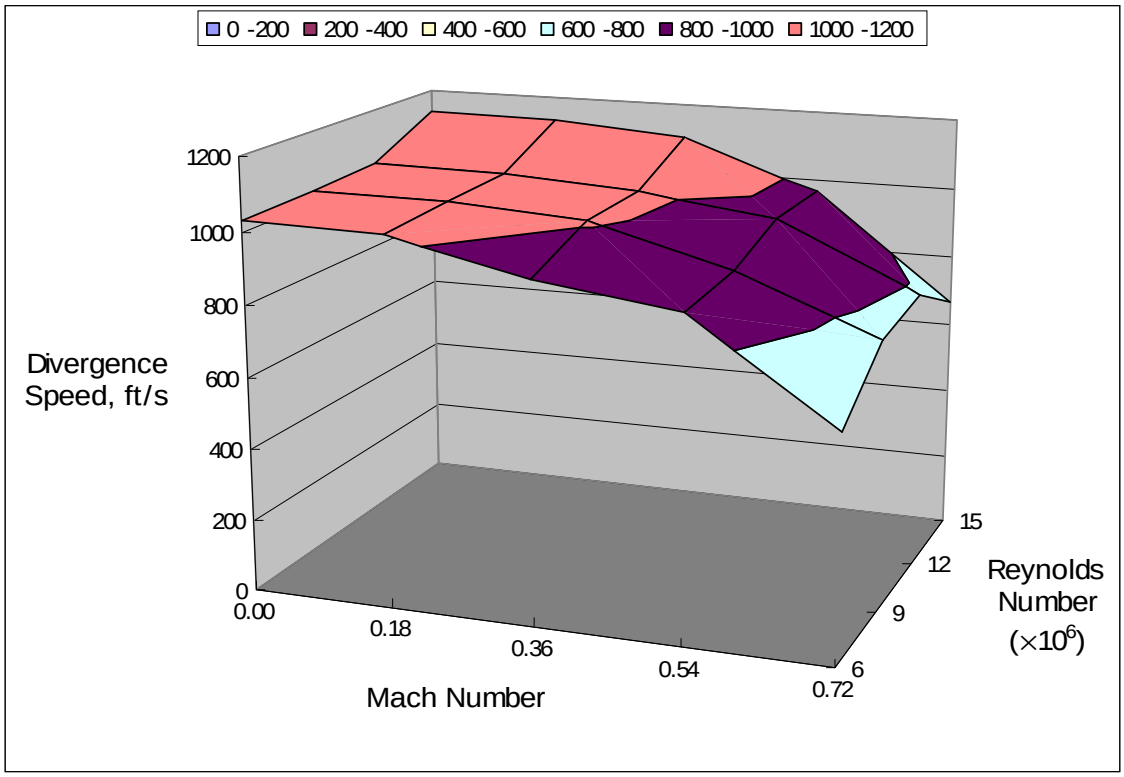

Figure 4.25: Divergence speed of a flying aircraft at 30,000 ft

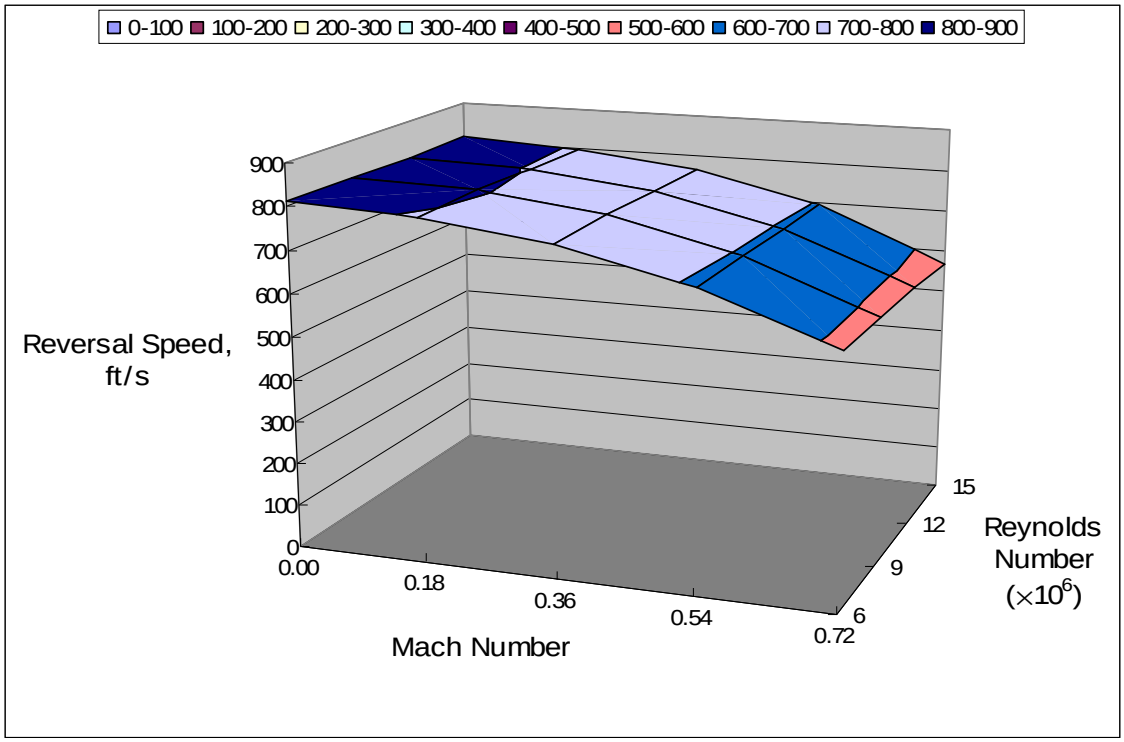

Figure 4.26: Reversal speed of a flying aircraft at 30,000 ft

Table 4.6: The variation of air properties with respect to the altitude and the lift-curve slope for NACA 0009

Altitude, ft	**Sea Level**	**5000**	**10000**	**15000**	**20000**	**25000**	**30000**
Temperature, °R	518.69	500.86	483.04	465.23	447.43	429.64	411.86
Density, slug/ft^3 (×10^{-3})	2.38	2.05	1.76	1.50	1.27	1.07	0.90
Viscosity, slug/ft-s (×10^{-7})	3.74	3.52	3.30	3.09	2.87	2.65	2.44
Reynolds No. (×10^6)	2.54	2.33	2.13	1.94	1.77	1.61	1.46
C_{l_α}	6.69	6.62	6.50	6.45	6.38	6.33	6.32

To investigate realistic cases, the variation of the density and the viscosity with respect to the altitude must be involved in the models (assumed constant before). Table 4.6 lists different air properties with respect to the altitude and the associated lift-curve slope from XFOIL.

It is clear to see the variations of Reynolds number with respect to the altitude under the standard atmosphere in Figure 4.27. Reynolds number decreases with the increasing of the altitude. Figure 4.28 shows the lift-curve slope versus Reynolds number for NACA 0009 with 1-degree aileron deflection. Reynolds number decreasing also makes the lift-curve slope decrease. Therefore, the lift-curve slope is lower at the higher altitude. The lower lift-curve slope increases the divergence dynamic pressure. The results in Figure 4.29 clearly show the variations of the aeroelastic boundaries with respect to the altitude under the standard atmosphere. Both reversal and divergence dynamic pressures increase with the increasing altitude. The post-reversal regime expands slightly at higher altitude. This gave insight to the flight limitation, although the models here are relatively simpler than the real cases.

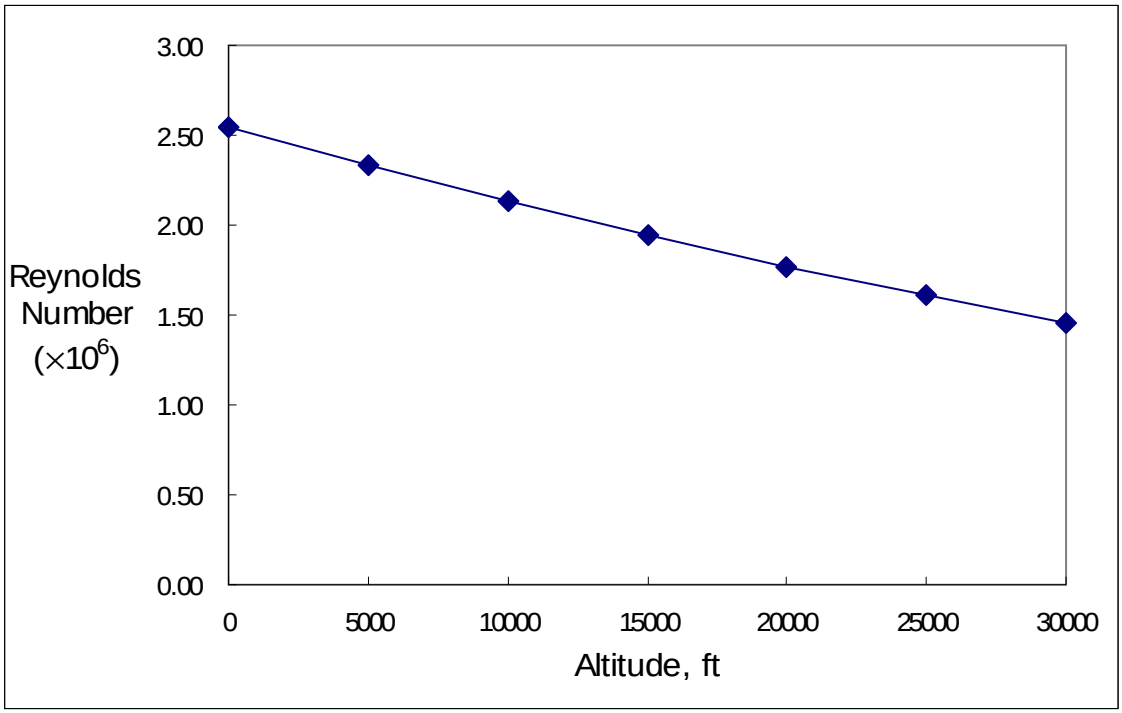

Figure 4.27: Reynolds number versus altitude

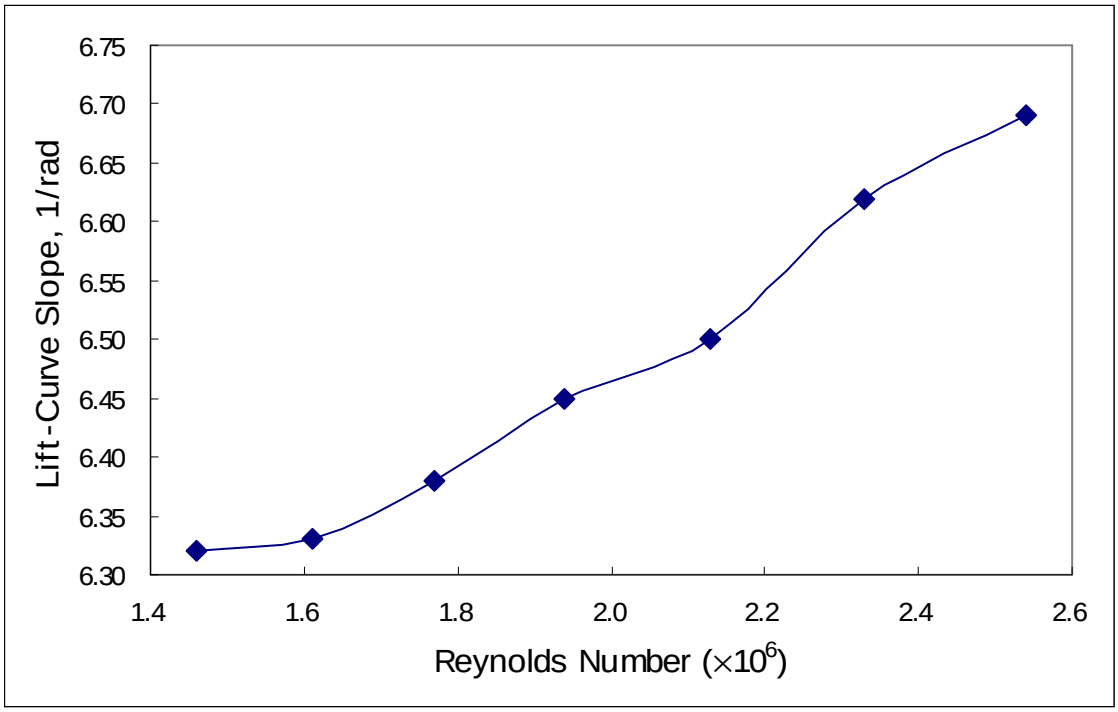

Figure 4.28: Lift-curve slope versus Reynolds number (M_∞ = 0.36)

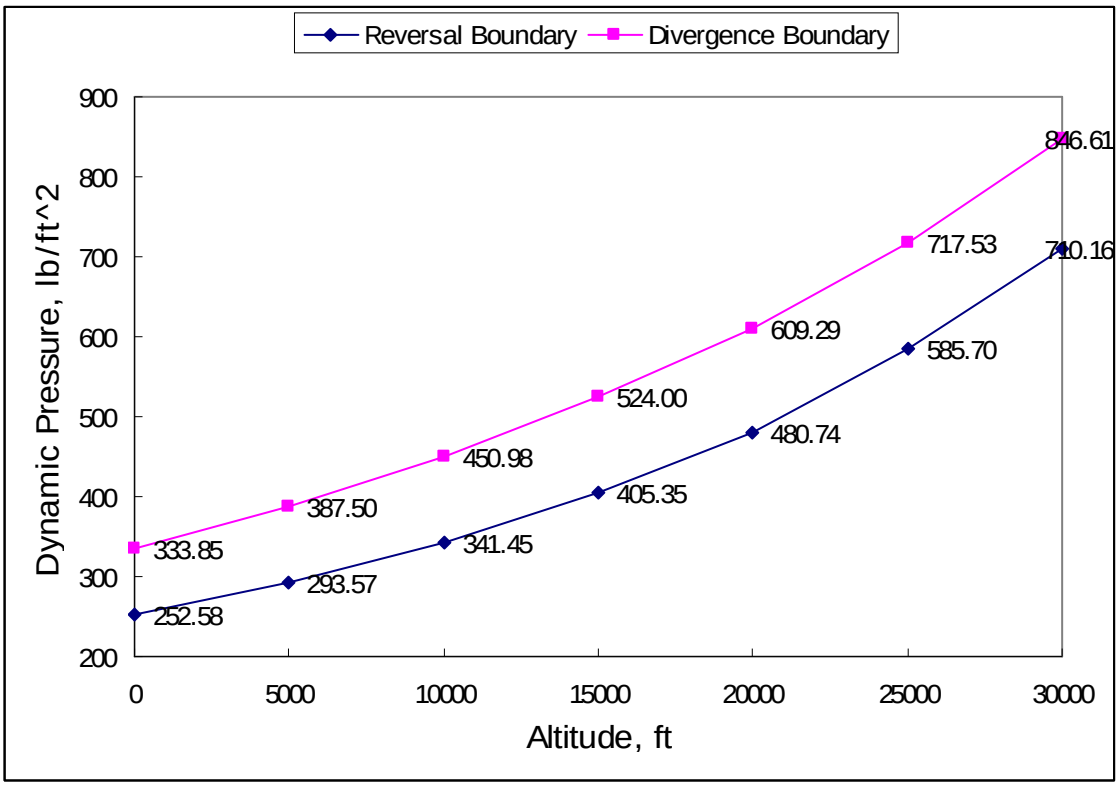

Figure 4.29: Aeroelastic boundaries versus the altitude under standard atmosphere

4.2.4 Numerical Results

Up to now, the solid wings are used to all the models in DYMORE, which means more mass and stiffness are generated for the models. It is not realistic, especially for the rolling aircraft due to the trim analysis. That being the case, a simple design for the inner structures of a wing section is shown as Figure 4.30. In addition, more realistic materials are used to reduce the weight but increase the stiffness. Aluminum alloy 7075-T6 is used for the skin and spar. Aluminum 5052 Honeycomb is used for the core.

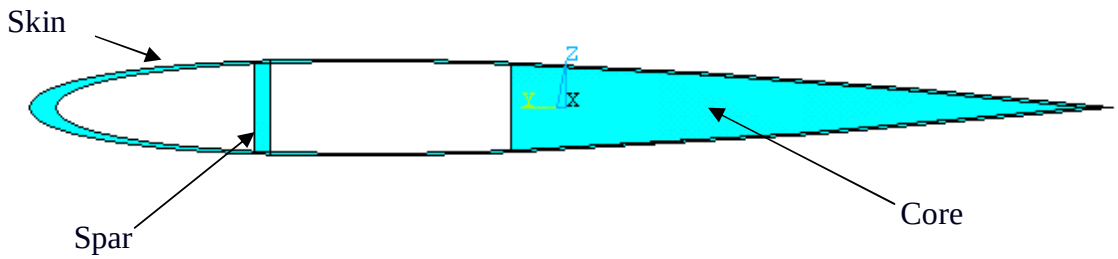

Figure 4.30: 2-cells inner structures for the wing section (NACA 0009)

Table 4.7: Structural properties of the uniform wing

Property	Uniform Wing
Axial Stiffness (lb)	1.136×10^{7}
Bending Stiffness (lb-ft^2)	1.688×10^{5}, 1.428×10^{8}
Torsional Stiffness (lb-ft^2)	1.706×10^{4}
Shearing Stiffness (lb)	2.840×10^{7}, 1.696×10^{7}
Sectional Mass (slug/ft)	1.763×10^{-1}
Mass Moment of Inertia (slug-ft)	9.169×10^{-3}, 7.332×10^{-5}, 9.095×10^{-3}
Chord (ft)	1.0
Wingspan (ft)	10.0

Based on the aeroelastic model in Section 4.2.1, the uniform wing's structural properties are modified as Table 4.7. Following the same procedure for trim analysis, results for different components of the rolling moment versus the nondimensional operating dynamic pressure are shown in Figure 4.31. The rolling moment caused by the roll rate vanishes at the dynamic pressure equal to 157.59 lb/ft^2, which means that the roll rate vanishes. This plot shows the operating dynamic pressure up to 70% of divergence dynamic pressure, since the aeroelastic instability must be avoided for a flying aircraft.

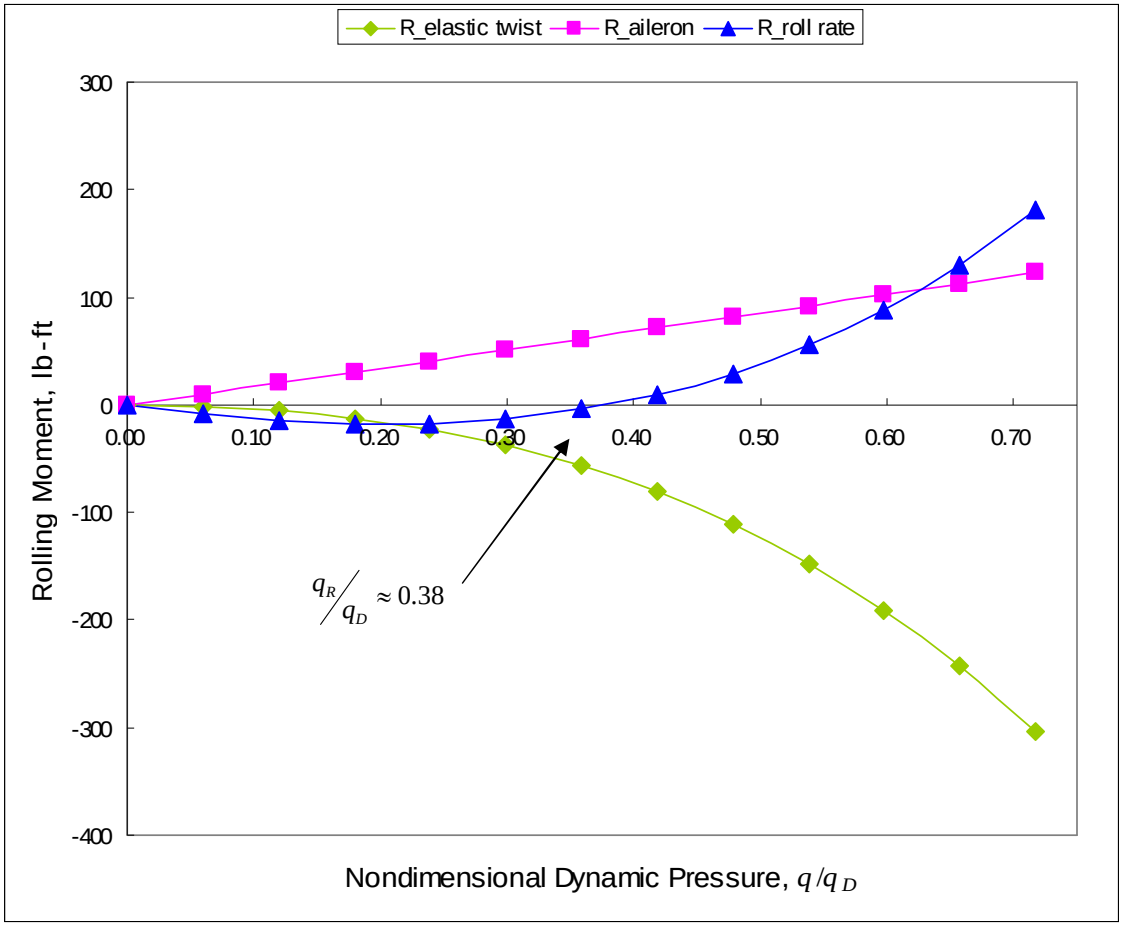

Figure 4.31: Variation of the components of the rolling moment versus nondimensional operating dynamic pressure (10-foot wingspan with inner structures design)

The rolling axis is the longitudinal axis of the fuselage and it is positive going to the tail of the aircraft. The variation of roll rate versus nondimensional dynamic pressure up to 70% of divergence dynamic pressure is shown in Figure 4.32. Positive roll rate represents the right wing of the aircraft going upward and the left wing going downward. After the reversal occurs, the maximum roll rate achieves five times of that for the conventional operating regime, although it has opposite direction.

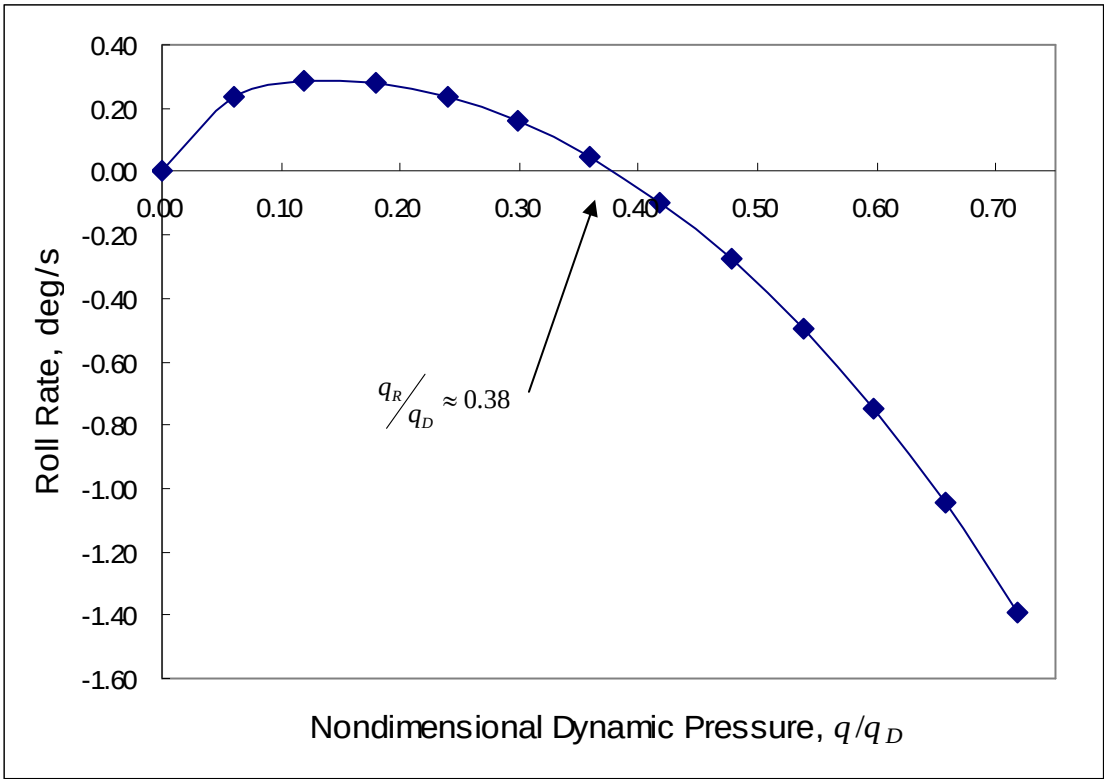

Figure 4.32: Steady roll rate versus nondimensional dynamic pressure

(10-foot wingspan with inner structures design)

Next, the model above is investigated again by moving the horizontal hinge location of the aileron to 90% chord. Note that both the aerodynamic model in XFOIL and the structural model in DYMORE changed to make certain both models are consistent with each other. Results for different components of the rolling moment versus the nondimensional operating dynamic pressure are shown in Figure 4.33. The rolling moment caused by the roll rate vanishes at the dynamic pressure equal to 208.58 lb/ft^2, which means that the roll rate vanishes. Comparing with the previous case, reversal dynamic pressure changed from moving the hinge to a different location. More details will be discussed in Chapter 6. As in the previous case, this plot shows the operating

dynamic pressure up to 70% of divergence dynamic pressure.

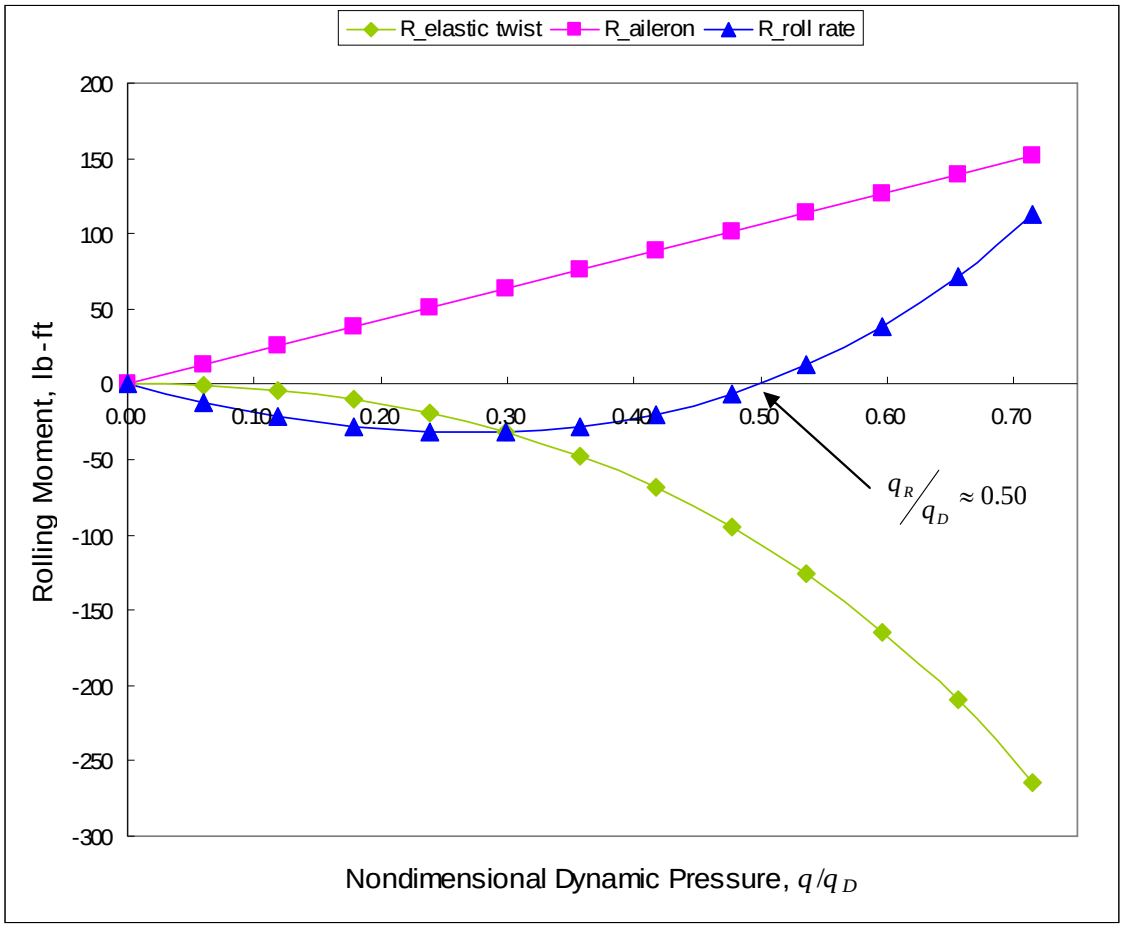

Figure 4.33: Variation of the components of the rolling moment versus nondimensional operating dynamic pressure (10-foot wingspan with inner structures design; hinge location at 90% chord)

The variation of roll rate versus nondimensional dynamic pressure up to 70% of divergence dynamic pressure is shown in Figure 4.34. In this case, the maximum roll rate only achieves twice of that for the conventional operating regime after the reversal occurs.

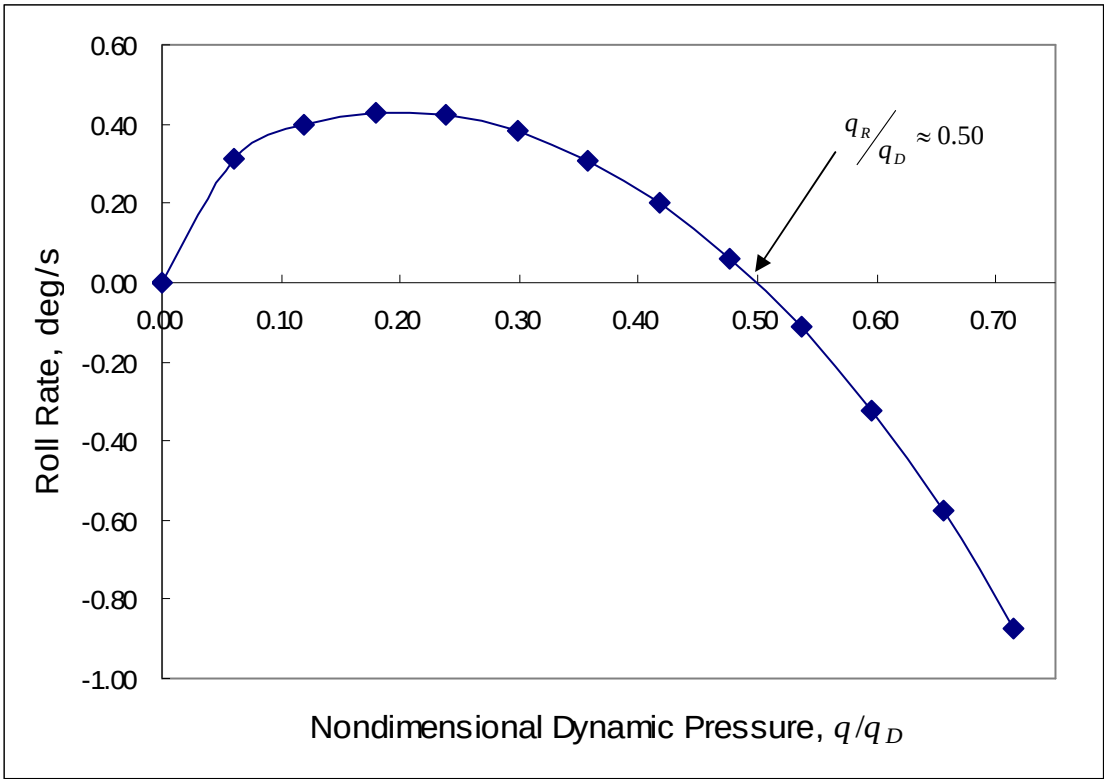

Figure 4.34: Steady roll rate versus nondimensional dynamic pressure (10-foot wingspan with inner structures design; hinge location at 90% chord)

4.3 Chapter Summary

Two aeroelastic models are investigated in this chapter. They are uniform lifting surface with aileron and rolling aircraft with ailerons, respectively. Both aerodynamic and structural nonlinearities are considered in the models to more accurately evaluate the post-reversal regime. In addition, the maneuverability for a flying aircraft is discussed in Section 4.2.3. The effects of aileron deflection, Mach number, Reynolds number, as well as the altitude are investigated, and both divergence and reversal boundaries are

established based on a simple aeroelastic model. The more realistic case for rolling aircraft is presented in Section 4.2.4. Results show there are some effects of the structural design for this aeroelastic problem. More detailed studies for some structural parameters design will be described in Chapter 6. The analyses will focus on how these parameters influence the aileron effectiveness. Before that, there are the comparisons and verifications of the results between XFOIL, advanced CFD codes, and the experimental data for some special cases in Chapter 5. The objective for Chapter 5 is to verify the practicality of the previous results.

CHAPTER V

COMPARISONS AND VERIFICATIONS BETWEEN XFOIL, CFD, AND EXPERIMENTAL DATA

5.1 Two-Dimensional Airfoil Characteristics with/without Closed Trailing Edge

XFOIL has the ability to do airfoil redesign through "Geometry Design Routine" for the models (see Appendix A). Airfoil can be modified by interactive specification of new geometric parameters such as leading-edge radius, trailing-edge thickness, and hinge locations. To verify the practicability of the airfoil characteristics from XFOIL and its ability for geometric design, the SC1095 airfoil, which is utilized in the UH-60A main rotor, is investigated for two different geometries with XFOIL and compared with the results shown in Ref. [105]. Figure 5.1 shows the lift coefficient with respect to angles of attack for the SC1095 airfoil from XFOIL compared with the results from advanced CFD codes. The results using the advanced CFD codes are provided by the first author of Ref. [105]. Smith in Georgia Tech used Cobalt LLC, Phanse in Georgia Tech used CFL3D, Army Aeroflightdynamics Directorate (AFDD) used OVERFLOW, Aviation Engineering Directorate (AED) used FUN2D, and Baeder in University of Maryland used TURNS as their CFD codes. In addition, the table look-up results are from Ref. [102]. The test conditions are set as Mach number equal to 0.4 and Reynolds number equal to 6.5 million, which is consistent with the model in Ref. [105]. One curve from XFOIL is for the normal geometry of the airfoil, and the other is for the geometry with closed trailing

edge, and the geometries are shown as Figure 5.2.

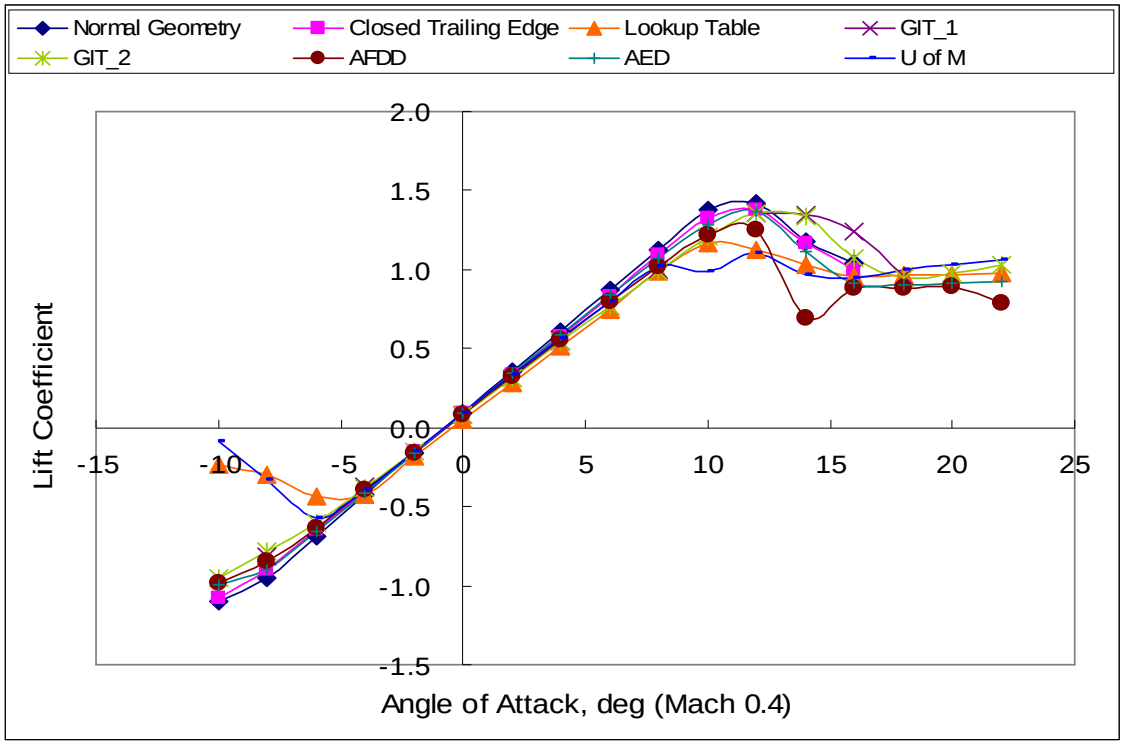

Figure 5.1: Comparison of lift coefficient of SC1095 airfoil between XFOIL and CFD

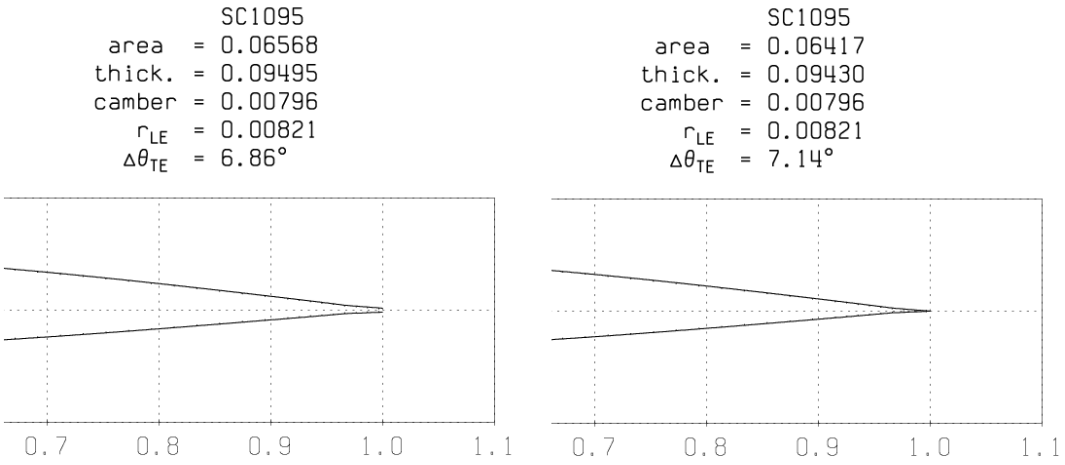

Figure 5.2: Different geometries of SC1095 airfoil from XFOIL

Based on the range of angles of attack from -10° to 22°, XFOIL generates the lift coefficient up to 16°, which exceeds the stall angle of attack. Beyond 16°, the airfoil has

stalled, so the viscous/inviscid analysis of XFOIL is no longer physically appropriate to generate correct results. The curves from XFOIL have good agreement with the results from advanced CFD codes, except for the curves generated from University of Maryland and the data in Ref. [102]. There is less than 5% difference of the lift-curve slope between the two geometries in XFOIL, although the geometry with closed trailing edge will not be used in this dissertation since it is not practical. XFOIL can predict the lift coefficient well in the linear range, and even slightly beyond the stall angle of attack. Capturing the trends is sufficient for the approaches herein.

5.2 The Variation of Lift-Curve Slope

A more rigorous indication of XFOIL capabilities can be investigated by further comparison of the sectional lift characteristics in the linear regime. The lift-curve slope multiplied by the Prandtl-Glauert subsonic correction is weakly dependent upon Reynolds number for values above one million and independent of subcritical Mach number. Experimental data [71] has shown the corrected lift-curve slope to be a good indication. McCroskey proposed an equation for this relationship for the NACA 0012 airfoil as

$$\beta_p c_{l_\alpha} = 0.1025 + 0.00485 \log\left(\mathrm{Re}/10^6\right) \tag{42}$$

In the subsonic range $M_\infty \le 0.5$, c_{l_α} is given by Eqn. (42) to within $\pm 2\%$. Especially a good fit of the lift-curve slope data in the limited range $2\times10^6 \le \mathrm{Re} \le 2\times10^7$ is given by Eqn. (42). Results from XFOIL are compared with the

experimental data, which is generated directly from Eqn. (42), and shown in Figures 5.3 and 5.4. The trend of the curve agrees well with the experimental data in Figure 5.3, with less than 6% difference between two curves. Note that the dashed lines in Figure 5.3 represent the reliable range of Eqn. (42), where Mach numbers are 0 and 0.5, respectively.

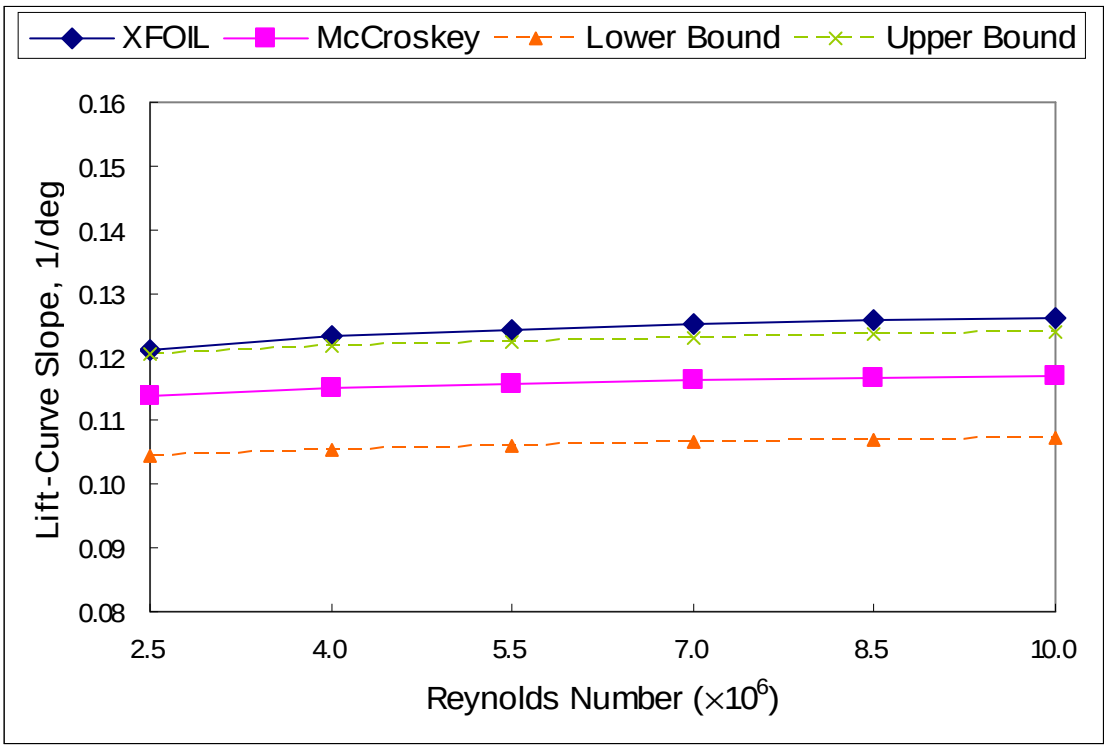

Figure 5.3: Comparison of lift-curve slope with Reynolds number ($M_\infty = 0.4$)

The variation of lift-curve slope is close to the experimental data. Although there is widening difference while increasing Mach number, the average 5% difference is still acceptable. Note that the dashed lines in Figure 5.4 represent the reliable range of Eqn. (42), where Reynolds numbers are 2×10^6 and 2×10^7, respectively.

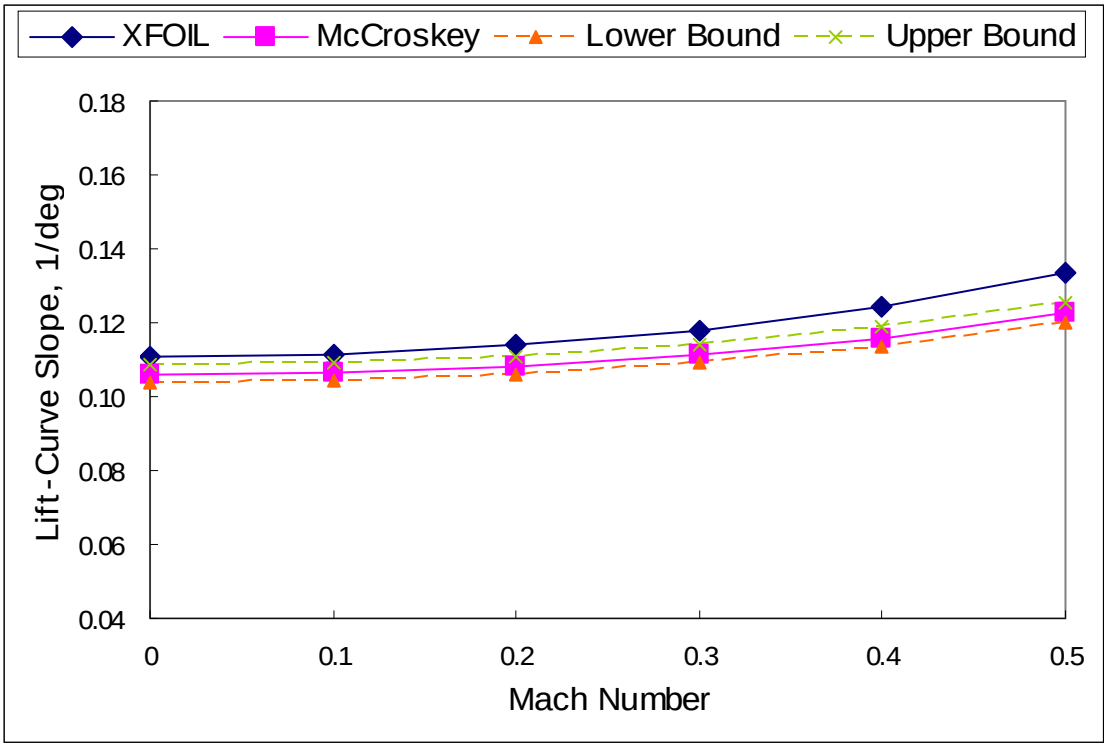

Figure 5.4: Comparison of lift-curve slope with Mach number (R_e = 5,500,000)

5.3 Wing-Aileron System with Varying Aileron Deflection

To verify the accuracy of the data for the wing-aileron system from XFOIL, results for S7012 airfoil with three kinds of aileron deflection, 2.5, 5, and 10 degrees, are compared with the experimental data from University of Illinois at Urhana-Champaign (UIUC) which are recorded in Refs. [66] and [99]. Reynolds number is set to be 0.3 million to be consistent to the models in UIUC, and results are shown in Figures 5.5, 5.6, and 5.7.

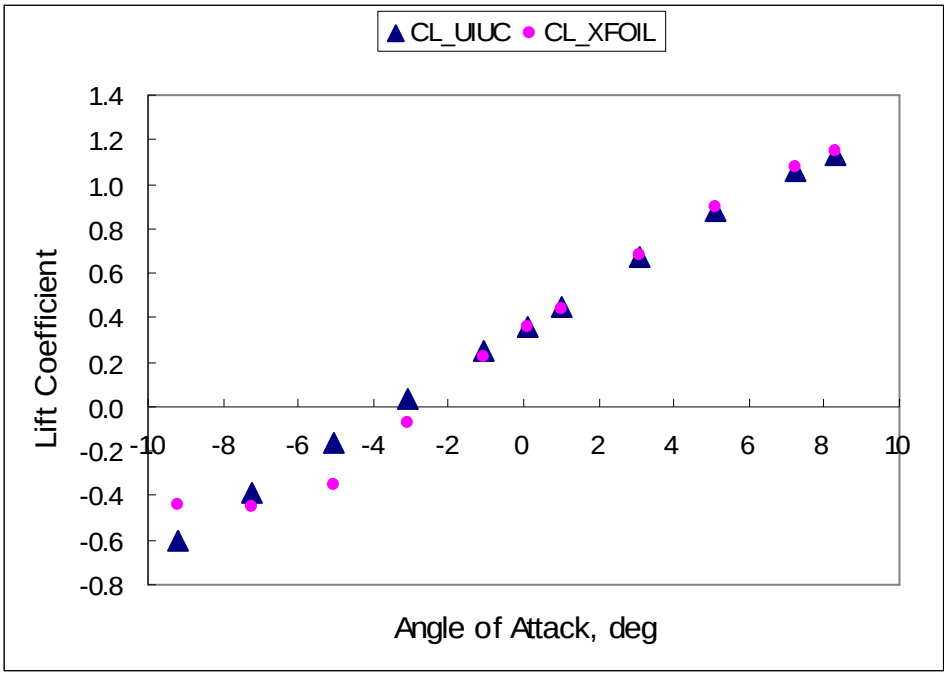

Figure 5.5: Comparison of lift coefficient of S7012 airfoil with 2.5 degree aileron deflection

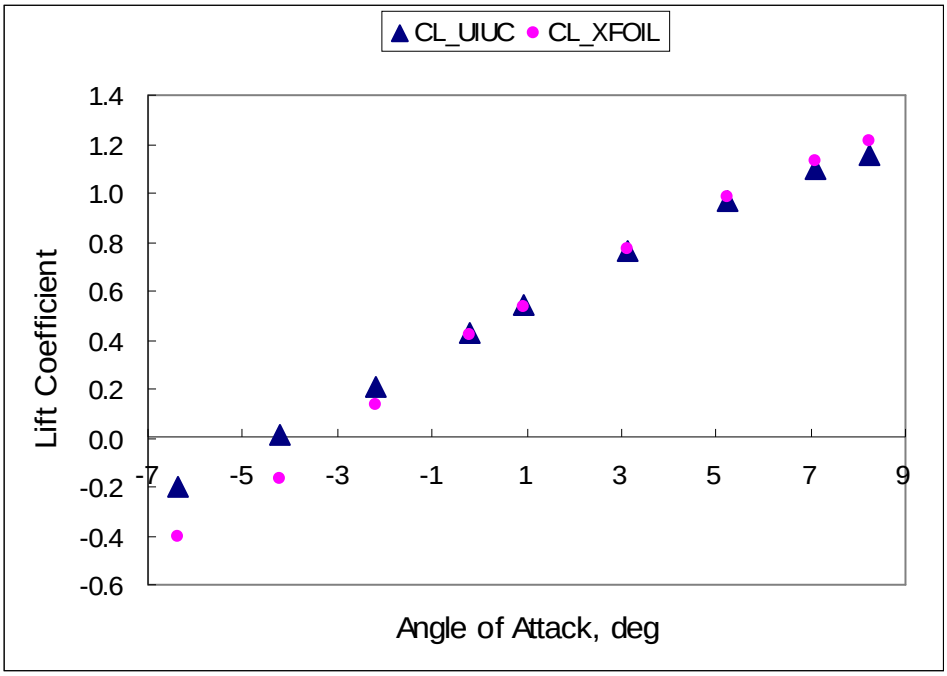

Figure 5.6: Comparison of lift coefficient of S7012 airfoil with 5 degree aileron deflection

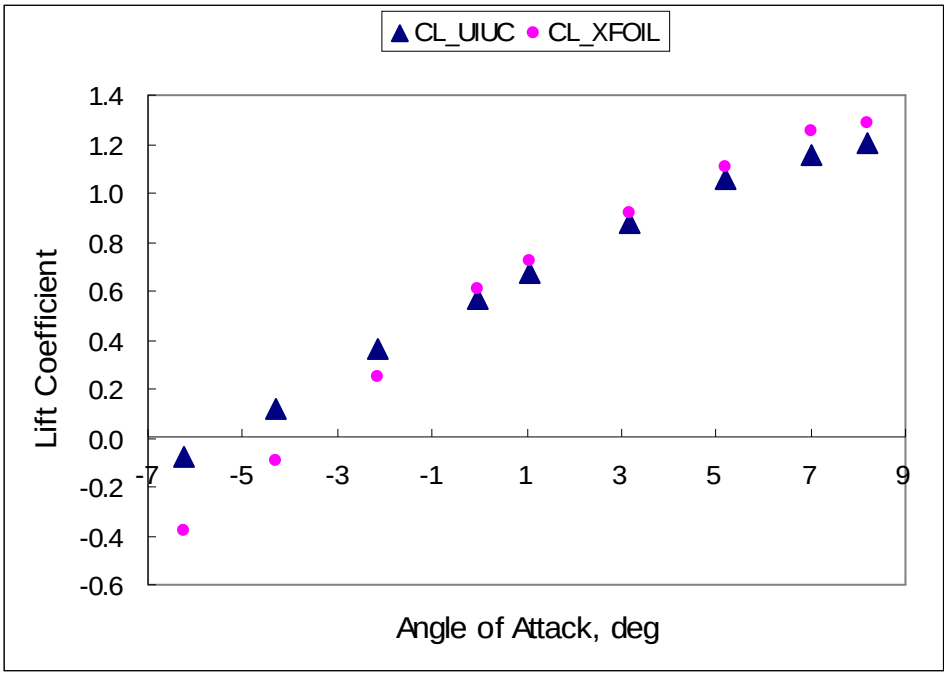

Figure 5.7: Comparison of lift coefficient of S7012 airfoil with 10 degree aileron deflection

Compared with the experimental data within the linear regime, XFOIL can predict the lift coefficient well and has less than 3% difference with the data from UIUC. Although XFOIL has the capability to predict the lift coefficient slightly beyond the stall angle of attack, results show the difference is getting larger with increasing aileron deflection in the nonlinear regime. For the lift-curve slope, XFOIL has only a 2% difference with the experimental data for the model with 2.5 degrees aileron deflection. While the aileron deflection increasing to 10 degrees, there is more than 6% difference between results from the two sources, and XFOIL is no longer reliable. The aileron deflection for most of the models in this dissertation is set to be 1 degree, and XFOIL can predict the aerodynamic coefficients very well. If the research is extended to the case with higher aileron deflection, the advanced CFD codes should replace XFOIL to

accurately build the aerodynamic model.

5.4 Chapter Summary

To verify the practicality of the results from XFOIL, three different approaches are executed to compare with CFD codes and the experimental data. First, in Section 5.1, the lift coefficient of SC1095 airfoil from XFOIL is verified with CFD codes, and XFOIL's capability for geometric design is demonstrated there. Next, the lift-curve slope for NACA 0012 is indirectly compared with the experimental data by use of Eqn. (42) proposed by McCroskey, and the results are shown in Section 5.2. In Section 5.3, the wing-aileron system with different aileron deflection for S7012 airfoil is checked by the wind tunnel data generated from UIUC. Results show XFOIL is a good option to quickly generate the accurate data in the initial analyses, except for larger aileron deflection. Since the aileron deflection has been kept 1 degree for most of the models in this dissertation, a sufficiently accurate aerodynamic model can be developed for use in DYMORE based on XFOIL and experimental data. The parametric design based on this aerodynamic model for enhancement of roll maneuverability will be discussed in Chapter 6.

CHAPTER VI

POST-REVERSAL PARAMETRIC DESIGN

To enhance roll maneuverability by post-reversal design, the influence for aspect ratio of the wings is first checked based on the previous models. In addition, the direct method used for airfoil design in XFOIL allows ones to generate aerodynamic coefficients with respect to any geometry. The airfoil can be modified by interactive specification of new geometric parameters such as leading-edge radius, trailing-edge thickness, hinge locations, flap deflection, and airfoil dimension. Here hinge locations and the airfoil dimensions are selected as the design variables. The built-in airfoil, NACA 0009, is chosen for these analyses. To simulate the more realistic wing sections, different airfoil inner structures and composite materials are investigated as well. The finite element based tools ANSYS and DYMORE are used for these purposes.

The objective here is to show how these design variables affect the aeroelastic phenomena, such as divergence and reversal speeds as well as the static loading distribution over wings. The nonlinear analyses are implemented by using the aeroelastic models built in the nonlinear tool, DYMORE. Structural nonlinearities are included in the tool with geometrically-exact composite beam theory, and aerodynamic nonlinearities are included in the tool through look-up airtable with static stall model. To determine the effectiveness of the ailerons within the post-reversal regime, increasing the magnitude of rolling moment is chosen as the design metric for the cantilevered wing model and discussed in Section 6.1. On the other hand, increasing the magnitude of steady roll rate

is chosen as the design metric for the rolling aircraft model instead, and that will be discussed in Section 6.2. The same rolling axis is used to evaluate the aileron effectiveness for the two models, which is positive going backward from the origin of the coordinates system. The origin is located at the root of elastic axis of the wing. Note that aileron effectiveness can be quantified by normalizing it with the span of aileron to accurately compare different parametric design.

6.1 Post-Reversal Behavior for Cantilevered Wing

6.1.1 Aspect Ratio

The aspect ratio is an important geometric property of a finite wing, denoted by $\mathcal{AR}$ and defined as

$$\mathcal{AR} = \frac{l^2}{S} \tag{43}$$

which l is the wingspan, and S is planform area. For the rectangular wings, the aspect ratio is equal to the span divided by chord. The same solid cantilevered wing model as used in Section 4.1.1, except with material properties of Aluminum alloy 7075-T6, is investigated with aspect ratios 10, 12.5, and 15. The chord for the wing section is equal to 1 foot, which means the wingspans and the associated ailerons are 10, 12.5, and 15 feet, respectively.

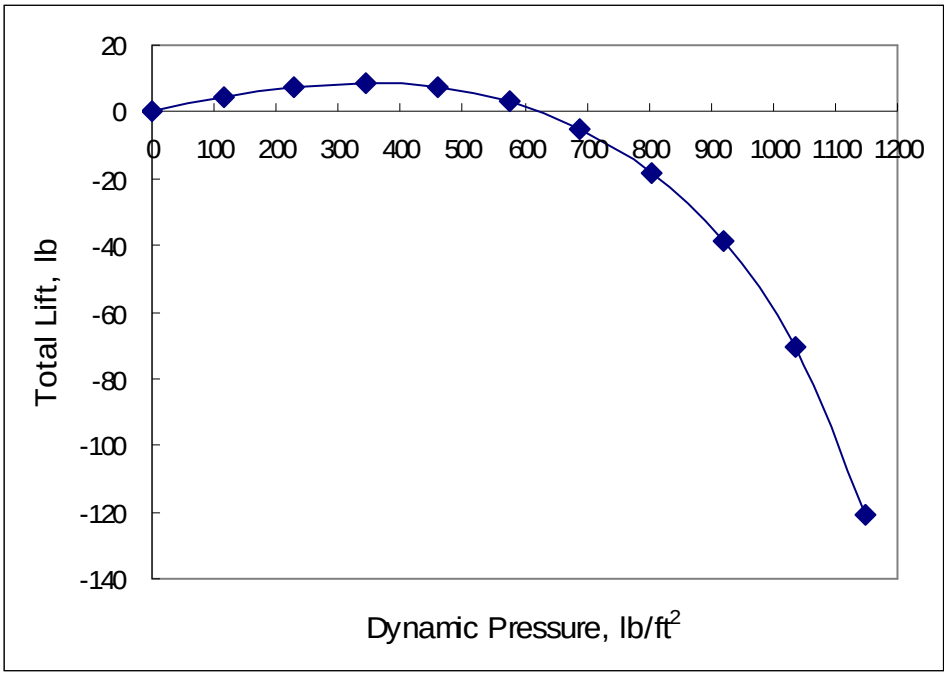

Figure 6.1: Total lift generated up to 80% divergence dynamic pressure ($\mathcal{AR}$ = 10)

For a unit aileron deflection, the divergence dynamic pressure for the model with $\mathcal{AR}$ = 10 is 1436.08 lb/ft^2, and reversal occurs at 626.69 lb/ft^2 of dynamic pressure. The total lift generated up to 80% divergence dynamic pressure is shown in Figure 6.1. To make certain whether or not the model encountered stall, the tip rotation is checked and shown in Figure 6.2. The maximum tip twist in this case is only -0.54° with respect to the wing axis, which is far below the stall angle of attack for NACA 0009 airfoil. To evaluate the effectiveness of the ailerons, the resulting rolling moment up to 80% divergence normalized by the span of aileron is shown in Figure 6.3. Results show at 80% divergence, there is more than twelve times rolling moment produced by unit aileron deflection than that in the conventional regime. Note that a positive aileron deflection produces a positive rolling moment (chordwise axis is positive going to the trailing edge) to make the wing up before reversal, but produces the rolling moment in opposite sense

within the post-reversal regime instead.

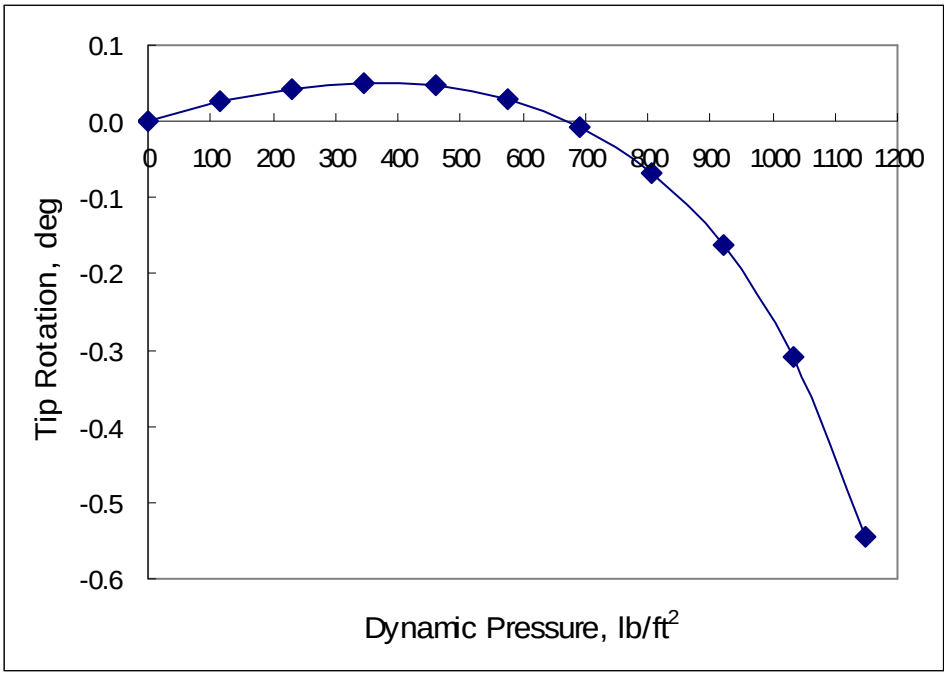

Figure 6.2: Resulting tip rotation up to 80% divergence dynamic pressure ($\mathcal{R}$ = 10)

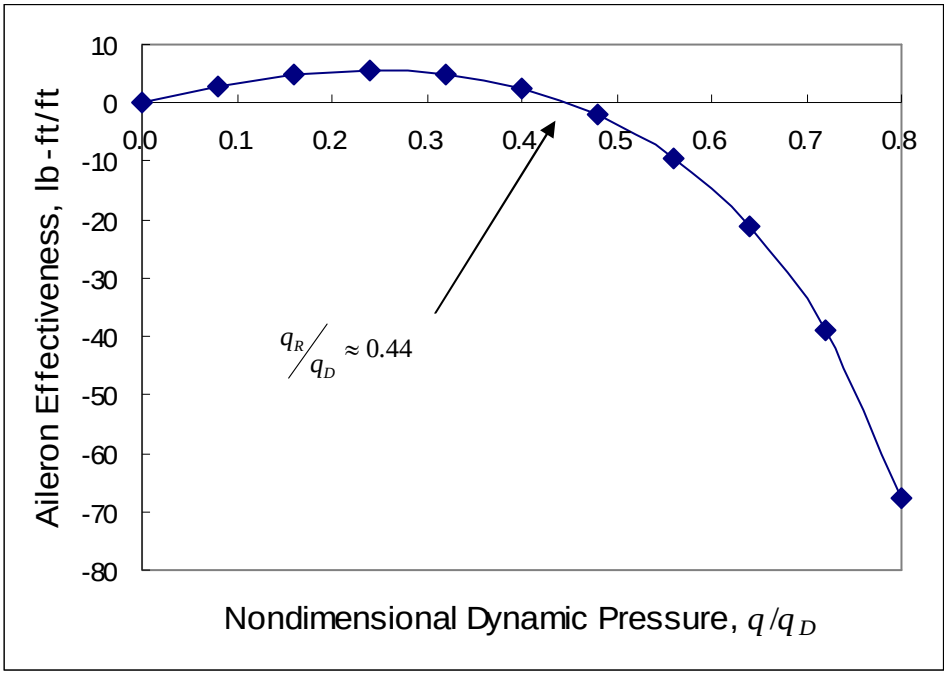

Figure 6.3: Aileron effectiveness versus nondimensional dynamic pressure ($\mathcal{R}$ = 10)

From the results shown in Figure 6.1, more than ten times the lift is generated than the regime before reversal. To check if the structures can sustain such high airloads, the stress analysis for the wing root is executed, since the root has the highest bending moment within the wing, and the results for Von Mises stress is shown in Figure 6.4. The highest stress is happened around the wing skin, and is below the yield stress for Aluminum 7075-T6, which is 1.15×10^7 lb/ft^2. Specially note if 80% divergence is the allowable operating dynamic pressure, which means the highest stress here is the allowable stress, the factor of safety, n_s, is equal to 7 for this case.

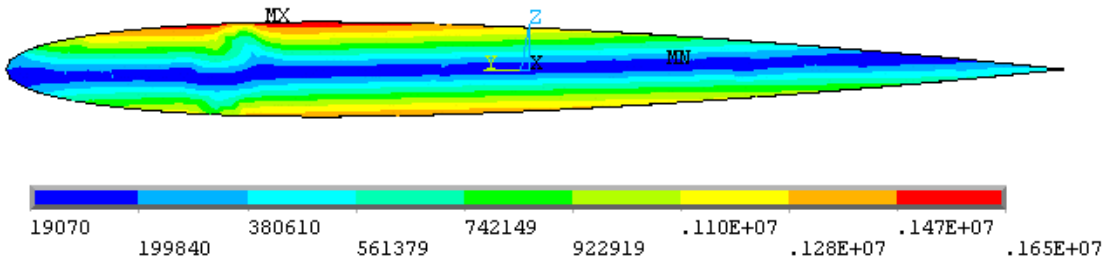

Figure 6.4: Von Mises stress at 80% divergence dynamic pressure for cantilevered wing ($\mathcal{AR}$ = 10)

For the $\mathcal{AR}$ = 15 model, given a unit aileron deflection, the divergence dynamic pressure is 491.59 lb/ft^2, and reversal occurs at 279.68 lb/ft^2 of dynamic pressure. Similarly, the total lift generated up to 80% divergence is shown in Figure 6.5, and the associated tip rotation is shown in Figure 6.6. Again, the resulting rolling moment up to 80% divergence normalized by the span of aileron is plotted as Figure 6.7. High aspect-ratio wing is structurally more flexible than lower one, which means for them the aeroelastic phenomena are more significant. Divergence and reversal dynamic pressure will decrease for higher aspect-ratio wings, and tends to decrease the resulting airloads at

80% divergence dynamic pressure. The Von Mises stress for this case is shown in Figure 6.8. Although the lower negative lift can be utilized during the post-reversal regime, the factor of safety is increased to 14.5.

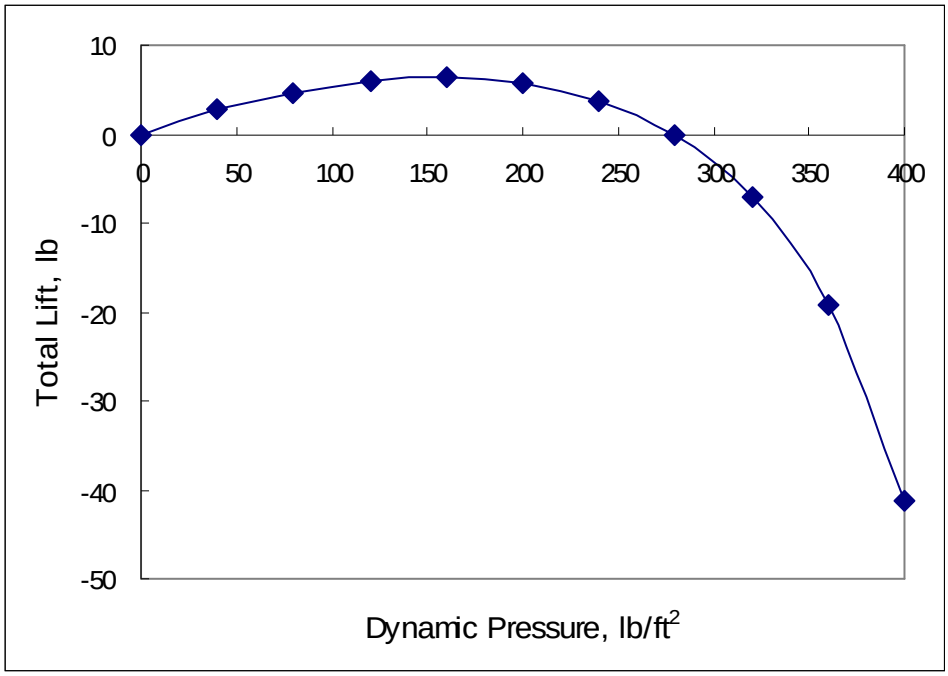

Figure 6.5: Total lift generated up to 80% divergence dynamic pressure (AR = 15)

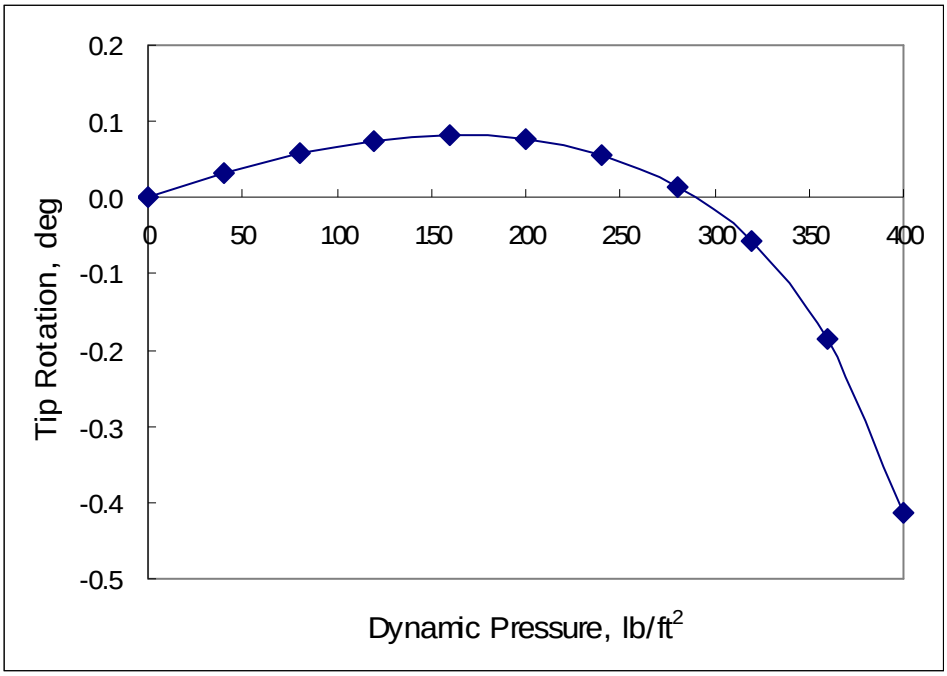

Figure 6.6: Resulting tip rotation up to 80% divergence dynamic pressure ($\mathcal{R}$ = 15)

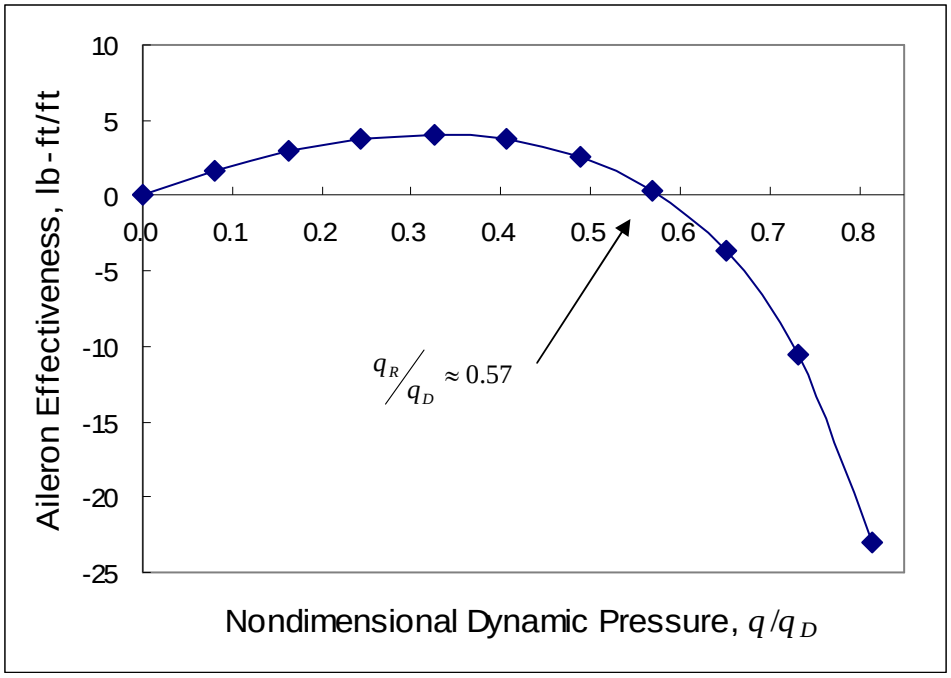

Figure 6.7: Aileron effectiveness versus nondimensional dynamic pressure ($\mathcal{R}$ = 15)

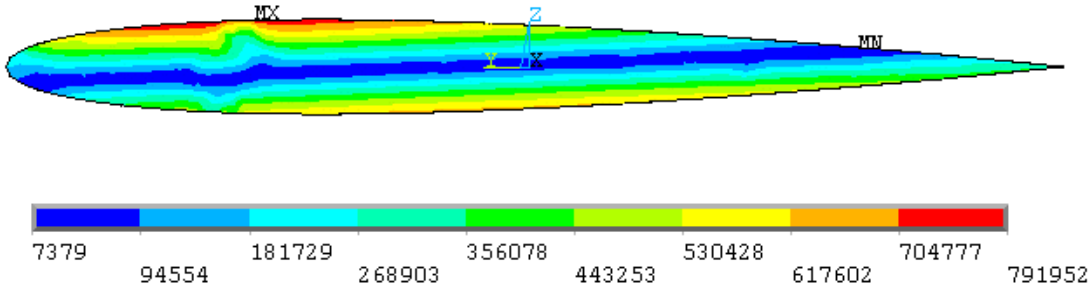

Figure 6.8: Von Mises stress at 80% divergence dynamic pressure for cantilevered wing (AR = 15)

Table 6.1 shows the comparisons between the three models investigated in this section. The post-reversal regime has shrunk for the AR = 15 case, and the more negative rolling moment due to aileron deflection can be generated for AR = 10 case. Within these three cases of high-aspect-ratio wings, aileron effectiveness is higher for the lower-aspect-ratio wings. The desired operating dynamic pressure can be increased for the higher aspect-ratio wings, since the resulting airloads are far below what the structures can sustain. For example, AR = 10 case can generate higher negative lift at 80% divergence which may result in two possible dangerous situations. Those are high stress distribution (beyond the yield stress of the materials) at the wing root and large tip rotation tending to encounter wing stall, respectively. Instead, AR = 15 case can generate lower negative lift and result in smaller tip rotation at 80% divergence, which means one can increase the desired operating dynamic pressure for the case. Specially note that comparisons are made here with respect to 80% divergence for each case due to different width of the post-reversal regime for them. Rather than making the comparisons at the same dynamic pressure, using the dynamic pressure at the same ratio of divergence is a better option here since exploring the post-reversal behavior is the main purpose for this

study. Instead, if there is only small difference for the width of the post-reversal regime, the same operating dynamic pressure within the regime is a better reference to make the comparison.

Table 6.1: Comparisons of aspect ratio for cantilevered wing

Aspect Ratio	Reversal Dynamic Pressure (lb/ft^2)	Divergence Dynamic Pressure (lb/ft^2)	80% Divergence Dynamic Pressure (lb/ft^2)		
			Lift (lb)	Tip Rotation (deg)	Aileron Effectiveness (lb-ft/ft)
10.0	626.69	1436.08	-120.97	-0.54	-67.61
12.5	402.74	801.43	-65.81	-0.46	-36.82
15.0	279.68	491.59	-41.20	-0.41	-23.03
Note: chord = 1 ft					

6.1.2 Hinge Location

In XFOIL, the *x*-axis is chord-wise direction, the *y*-axis is flap-wise direction, and the origin is placed at the leading edge of the model. For the 1-foot chord, given Reynolds number 3×10^6 and flap angle 1 degree, several horizontal hinge locations are investigated, and the range is from 0.7 to 0.925 ft from the leading edge. Three cases of the geometry with different horizontal hinge locations in XFOIL are shown in Figures 6.9, 6.10, and 6.11. The aerodynamic coefficients generated are then put into the DYMORE model for $\mathcal{AR}$ = 10 to build up full range angles of attack ($-180^\circ \le \alpha \le 180^\circ$) for analyses. Results in Table 6.2 and Figure 6.12 show that aeroelastic boundaries change with varying the horizontal hinge locations due to effective camber changes. Indeed, from Figures 6.9 to

6.11, effective camber changes so that divergence and reversal dynamic pressures change because different airtables are used in DYMORE.

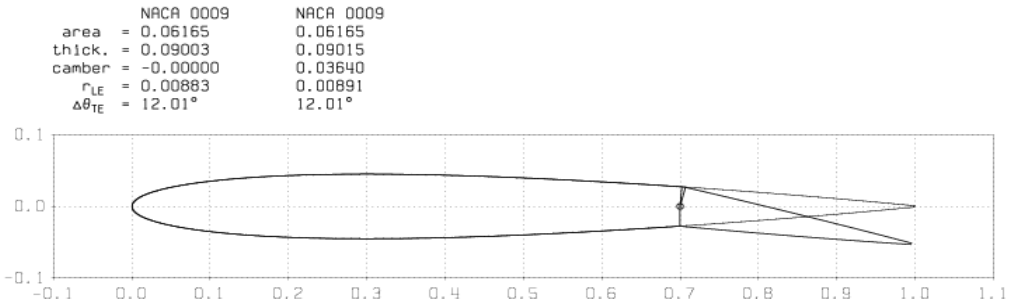

Figure 6.9: Horizontal hinge location at 70% chord

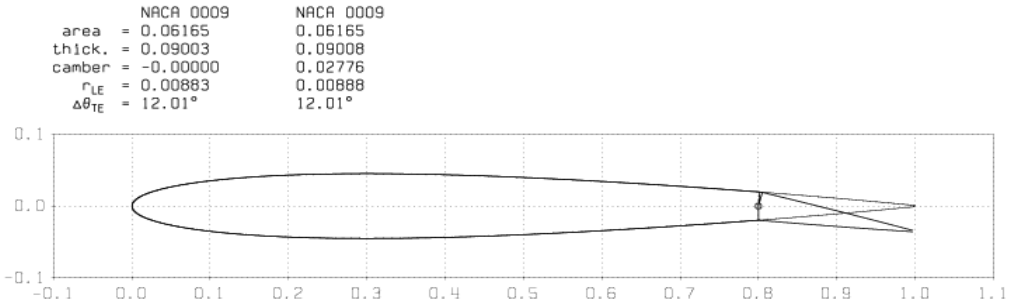

Figure 6.10: Horizontal hinge location at 80% chord

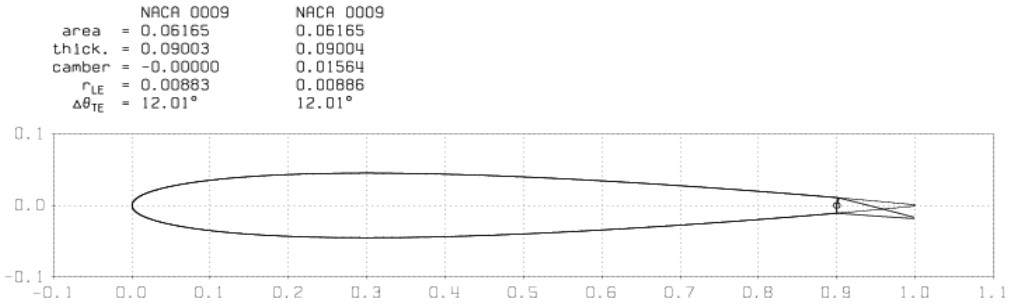

Figure 6.11: Horizontal hinge location at 90% chord

Table 6.2: Effects of horizontal hinge locations for critical speeds and aileron effectiveness for cantilevered wing

Horizontal Hinge Location (ft)	**0.7**	**0.725**	**0.75**	**0.775**	**0.8**
Reversal Dynamic Pressure (lb/ft^2)	623.25	601.06	592.64	579.29	567.72
Divergence Dynamic Pressure (lb/ft^2)	1686.57	1692.24	1709.31	1717.87	1726.46
Aileron Effectiveness (lb-ft/ft)	-25.51	-30.25	-32.78	-36.03	-37.90
Horizontal Hinge Location (ft)	**0.825**	**0.85**	**0.875**	**0.9**	**0.925**
Reversal Dynamic Pressure (lb/ft^2)	564.44	556.28	548.18	541.74	530.56
Divergence Dynamic Pressure (lb/ft^2)	1746.57	1761.01	1778.42	1810.56	1819.37
Aileron Effectiveness (lb-ft/ft)	-37.07	-35.55	-31.91	-25.92	-19.15
Note: Operating Dynamic Pressure = 1000 lb/ft^2					

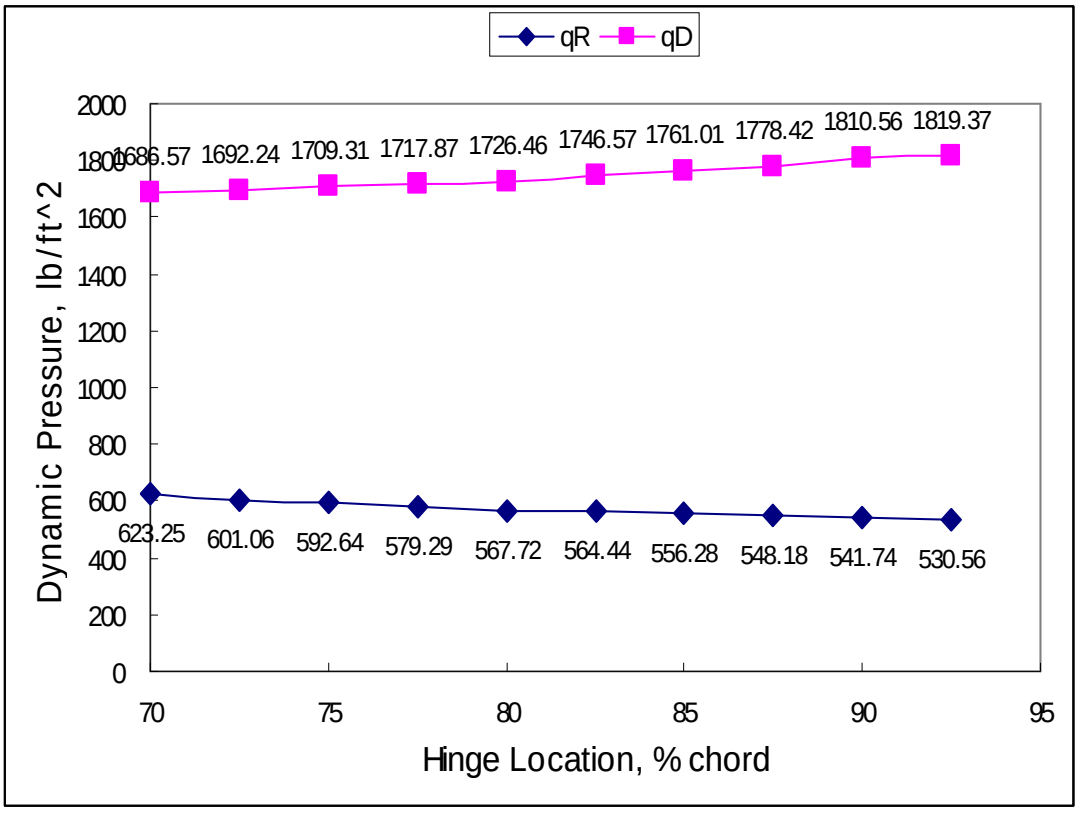

Figure 6.12: Aeroelastic boundaries versus horizontal hinge locations for cantilevered wing (operating dynamic pressure = 1000 lb/ft^2)

Figure 6.13 shows how horizontal hinge location affects the trend of aileron effectiveness at 1000 lb/ft^2 of operating dynamic pressure. Again, the aileron effectiveness is defined as the resulting rolling moment normalized by the span of aileron. Results show the hinge location at 80% chord can generate the most rolling moment.

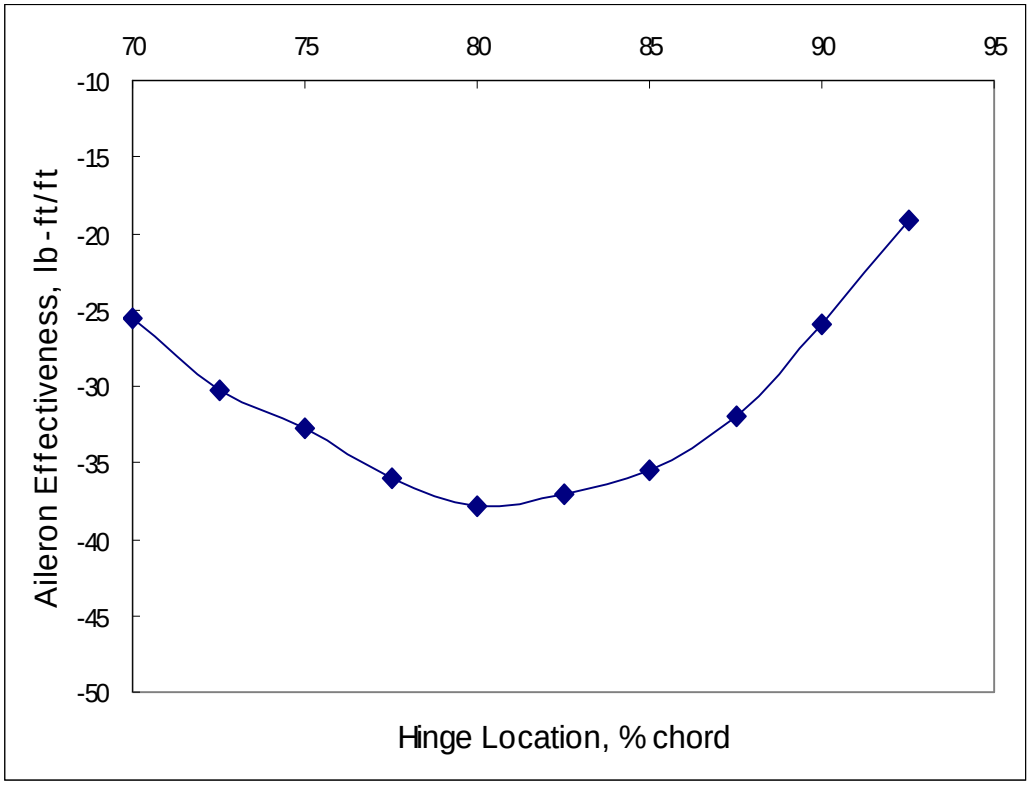

Figure 6.13: Aileron effectiveness versus horizontal hinge locations for cantilevered wing (operating dynamic pressure = 1000 lb/ft^2)

The total lift for each case up to 1000 lb/ft^2 of operating dynamic pressure is plotted as Figure 6.14. The trend is a powerful evidence for the results shown in Figure 6.13. Negative lift creates negative rolling moment (rolling axis is positive going to the trailing edge), and the largest magnitude of lift results in the largest rolling moment for rolling.

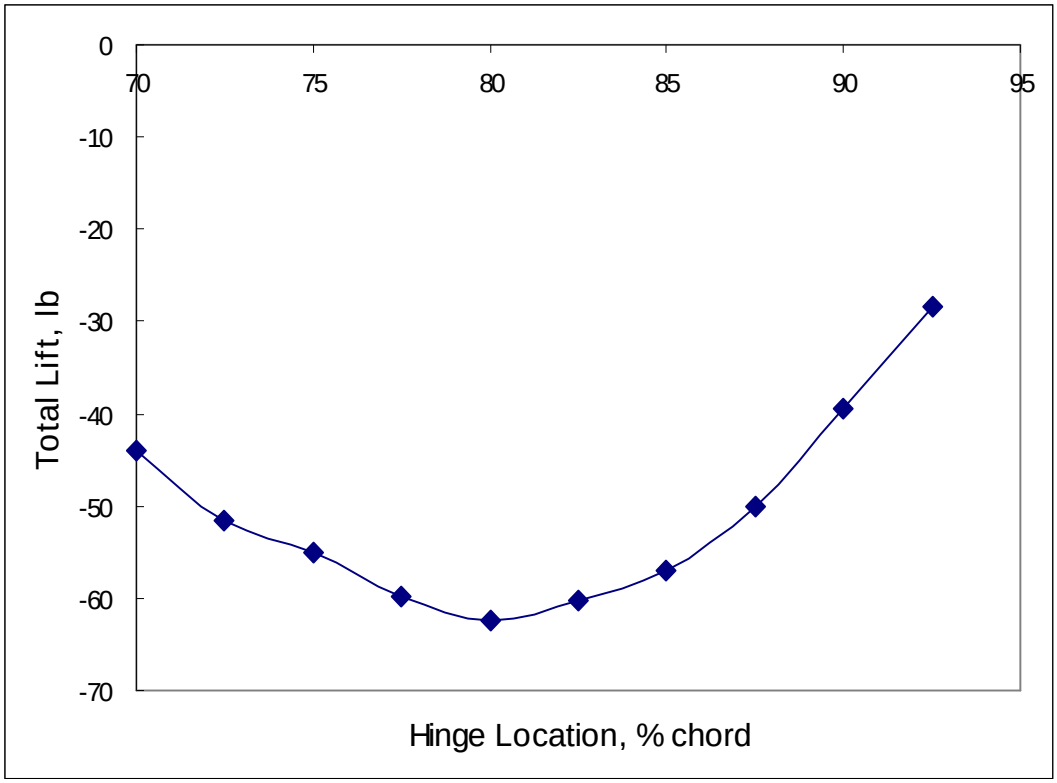

Figure 6.14: Total lift versus horizontal hinge locations (operating dynamic pressure = 1000 lb/ft^2)

Suppose the aileron is extremely small as in Figure 6.11. Since only very small lift is generated by the aileron, the aeroelastic effect is very small. The wing then can be thought of as rigid. Thus, the optimum location is expected to be somewhere forward of the trailing edge. From Figure 6.13, the better horizontal hinge location to provide large rolling moment is around 80% chord for the model with NACA 0009 airfoil.

Varying the vertical hinge location for thin airfoils does not strongly influence the aeroelastic of interest here. For the 1-foot chord of a NACA 0009 airfoil, the maximum thickness is only 1.08 inches. Similarly, the vertical dimension compared to the horizontal dimension for the aileron is extremely small. From Figure 6.15, the effective

moment arm, r, is equal to x if the vertical hinge is located at the mean camber line. Suppose the horizontal hinge location is kept constant but the vertical hinge location is slightly changed, say by dy, then the effective moment arm becomes

$$r = \sqrt{x^2 + (dy)^2} \tag{44}$$

Since dy is extremely small for a thin airfoil, then it follows that $r \approx x$. Therefore, compared to the effect of the horizontal hinge location, varying the vertical hinge location of thin airfoils almost has no influence on the aeroelastic phenomena of interest here. Numerical results obtained (not presented here) confirm this.

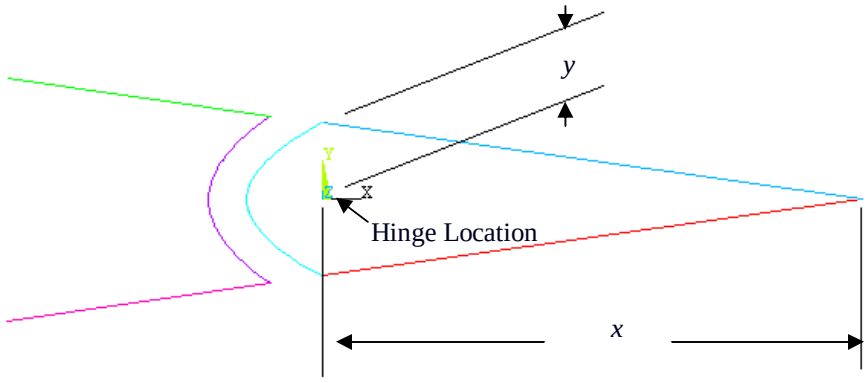

Figure 6.15: Schematic showing geometry of hinge location

6.1.3 Airfoil Dimension

Traditionally, more lift will be generated for larger planform area, which is proportional to the chord of the airfoil for rectangular wings. To investigate the effects of airfoil dimension to the aeroelastic problems, three different section dimensions are evaluated, which are 1.0, 1.25, and 1.5 foot chord, respectively. For all the cantilevered wing models with solid wing section and 15-foot wing span, the hinge is located at 80% chord line for each case with given Mach number 0.1, Reynolds number 3×10^6, and

angle of attack 2 degrees. The geometries for the three models in XFOIL are shown in Figure 6.16. Note that three plots are in different scales, but the actual size of airfoil can be seen from the coordinates.

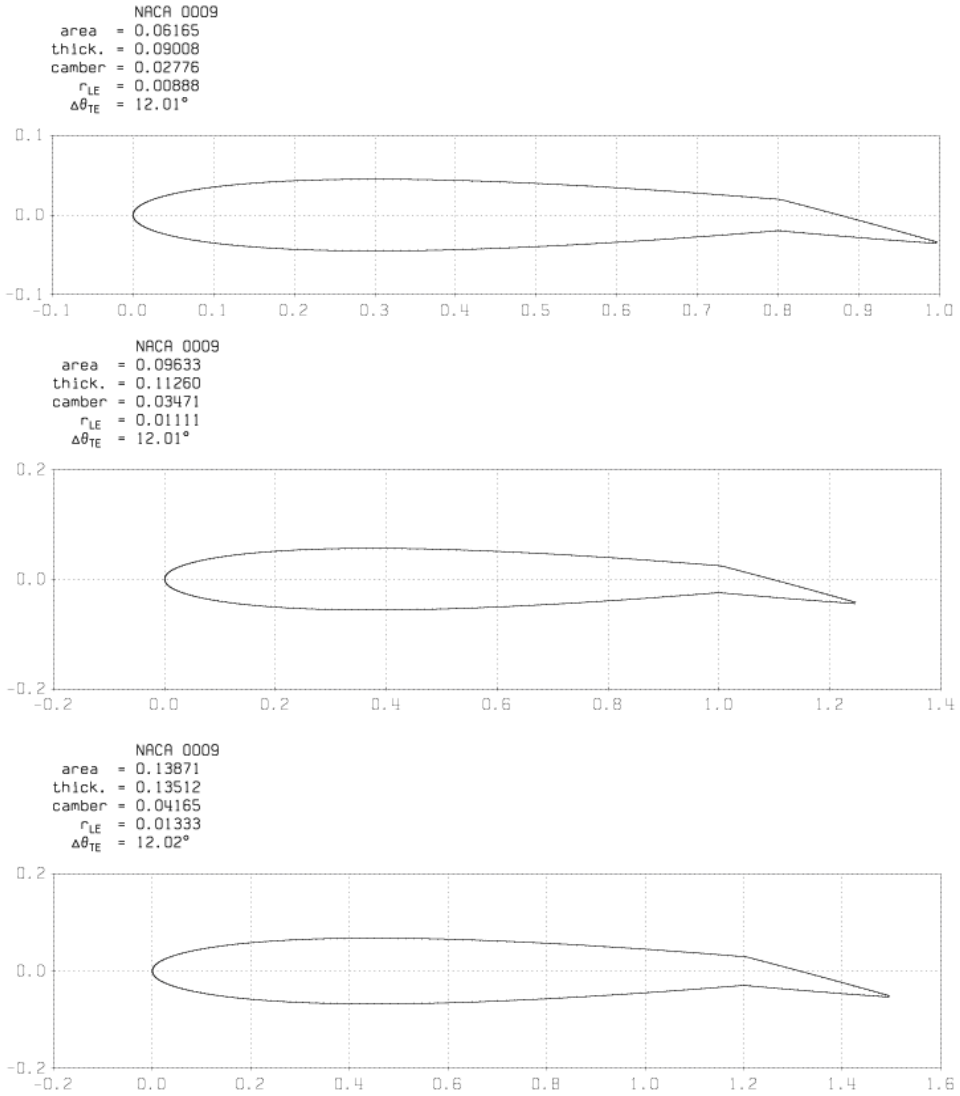

Figure 6.16: Airfoil dimensions by keeping *y/t* constant

Unlike the models in Section 6.1.1, aspect ratio changes by varying the chord but keeping the wing span constant. Results in Table 6.3 show the comparisons between three kinds of chord, resulting in three different aspect-ratio wings. Note that aileron effectiveness is defined as how much rolling moment can be generated up to 80%

divergence normalized by unit length of aileron here. From aerodynamic point of view, all the quantities of the aerodynamic parameters involved in the aeroelastic problems, such as lift and moment coefficients, are normalized by the product of dynamic pressure and planform area, which means theoretically there is hardly any influence on the reversal and divergence due to airfoil dimensions. The only effect is from the wing's aspect ratio. The more 3D effects, like downwash velocity, happened at the wing tip, since the chord increases in this case. On the other hand, to make consistent to the aerodynamic models, the sectional properties also change with varying the chord, which tends to increase the stiffness for the lower aspect-ratio wing. The major factor of structural properties is torsional stiffness, and both reversal and divergence dynamic pressures increase with increasing torsional stiffness. Therefore, there are higher reversal and divergence, and wider post-reversal regime for the model with 1.5-foot chord. Also, higher negative lift and higher rolling moment per unit length of aileron can be generated for this case. Note the tip rotations for three models are acceptable and far below the stall angle of attack. The Von Mises stress at the wing root up to 80% divergence for three cases are shown as Figures 6.17, 6.18, and 6.19, and the associated factors of safety are 14.5, 10.0, and 8.0, respectively.

Table 6.3: Comparisons of airfoil dimension for cantilevered wing

Chord (ft)		1.00	1.25	1.50
AR		15	12	10
Torsional Stiffness (lb-ft^2)		23,900	58,350	121,000
Reversal Dynamic Pressure (lb/ft^2)		279.68	460.01	690.39
Divergence Dynamic Pressure (lb/ft^2)		491.59	895.82	1449.17
80% Divergence Dynamic Pressure	**Lift (lb)**	-36.41	-105.69	-234.07
	Tip Rotation (deg)	-0.37	-0.43	-0.46
	Aileron Effectiveness (lb-ft/ft)	-20.33	-58.63	-129.00

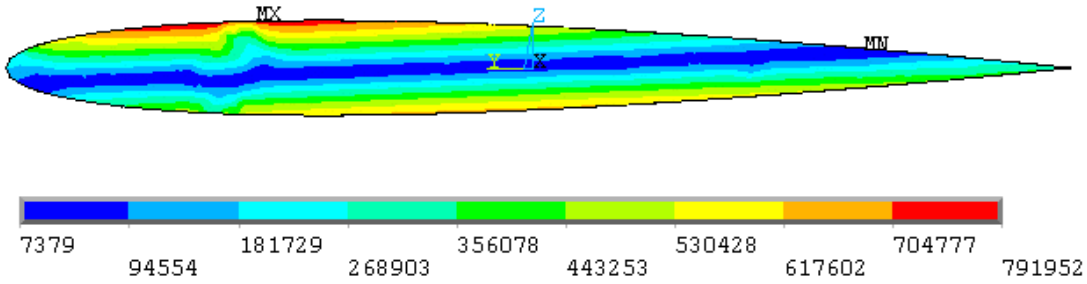

Figure 6.17: Von Mises stress at 80% divergence dynamic pressure for 1-foot chord cantilevered wing

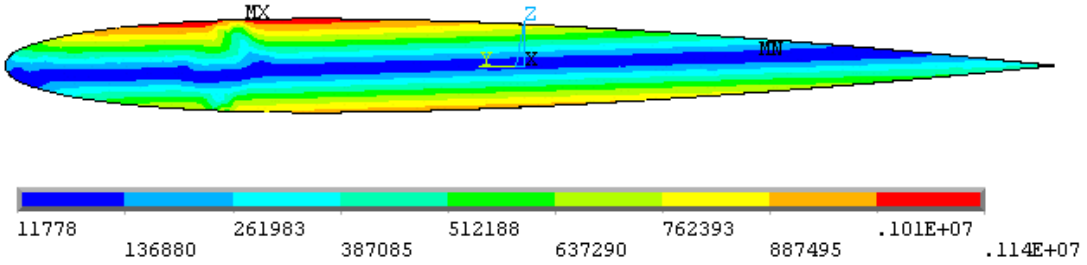

Figure 6.18: Von Mises stress at 80% divergence dynamic pressure for 1.25-foot chord cantilevered wing

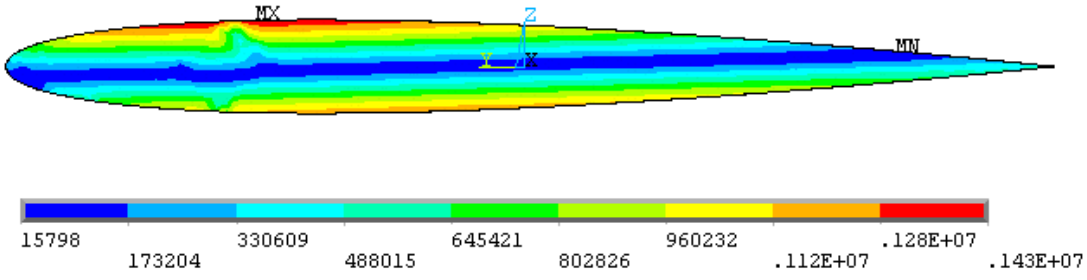

Figure 6.19: Von Mises stress at 80% divergence dynamic pressure for 1.5-foot chord cantilevered wing

6.1.4 Wing Section Inner Structures

Up to now, the solid wings are used for most of the models in DYMORE, except for the simple inner design of the wing discussed in Section 4.2.4. To simulate more realistic wings, the cases of inner design for the wing section with one to three cells are investigated [69]. Figure 6.20 shows the geometry for three inner designs. In addition, isotropic materials are used to reduce the weight but increase the stiffness [16, 20, 78]. Aluminum alloy 7075-T6 is used for the skin and spar. Aluminum 5052 honeycomb is used for the core [49].

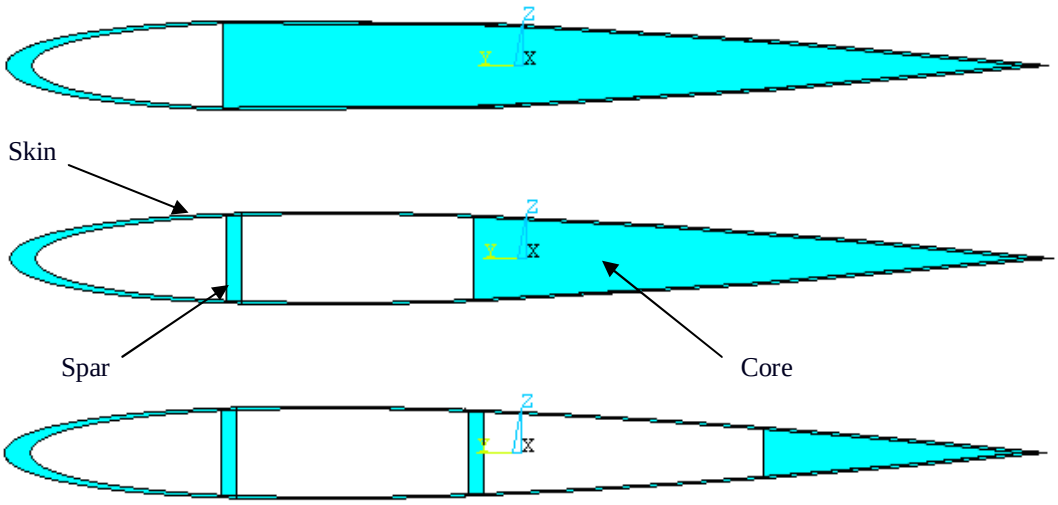

Figure 6.20: Schematic showing of the wing section inner design

Table 6.4 shows the comparisons between three inner designs for two cases of cantilevered wing model, which has 10-foot and 15-foot span, respectively. Note that aileron effectiveness is defined as how much rolling moment can be generated up to 80% divergence normalized by the span of aileron here. The sectional mass decreases with increasing cells, but the torsional stiffness increases instead due to stiffer material used in

the locations of the spar. With increasing torsional stiffness, both reversal and divergence dynamic pressures increase, and this agrees with the previous results. At 80% divergence, the higher torsional stiffness results in the wider post-reversal regime, the higher negative lift, and larger rolling moment per unit aileron deflection. On the other hand, comparing the same inner design between two spans, the magnitude of aileron effectiveness for the 10-foot case, which is structurally stiffer, is higher, and this agrees well with the previous results. To check if the models will encounter stall, the tip rotations at 80% divergence dynamic pressure are listed in Table 6.4. Also, Figure 6.21 shows the associated Von Mises stress of the wing root for three cases. The maximum stress happened around the skin for all the cases, but still below the yield stress of Aluminum alloy 7075-T6. The associated factors of safety are 4.9, 4.6, and 3.8, respectively.

Active Aeroelastic Wing Technology turns wing aeroelastic flexibility into a net benefit through use of multiple leading- and trailing-edge control surfaces. The main objective of this idea is to alleviate the weight penalty for the traditional design with the reinforcement of the wing structures. The weight of the wings can be dramatically decreased by multiple cells inner design, but the stiffness could be reduced in the meantime. To maintain the required stiffness of the wings, even higher, composite skin design, such as material choosing and layup design, will be discussed in the next section.

Table 6.4: Comparisons of wing section inner design for cantilevered wing

		10 ft			15 ft		
		1 Cell	**2 Cells**	**3 Cells**	**1 Cell**	**2 Cells**	**3 Cells**
Sectional Mass (slug/ft)		0.28	0.18	0.08	0.28	0.18	0.08
Torsional Stiffness (lb-ft^2)		14,060	17,060	24,340	14,060	17,060	24,340
Reversal Dynamic Pressure (lb/ft^2)		368.89	448.25	635.36	164.54	199.87	284.31
Divergence Dynamic Pressure (lb/ft^2)		721.53	867.16	1196.14	266.01	320.27	449.71
80% Divergence Dynamic Pressure	**Lift (lb)**	-31.71	-37.17	-46.25	-11.53	-13.35	-17.39
	Tip Rotation (deg)	-0.236	-0.227	-0.195	-0.192	-0.182	-0.163
	Aileron Effectiveness (lb-ft/ft)	-17.55	-20.52	-25.29	-6.41	-7.39	-9.54

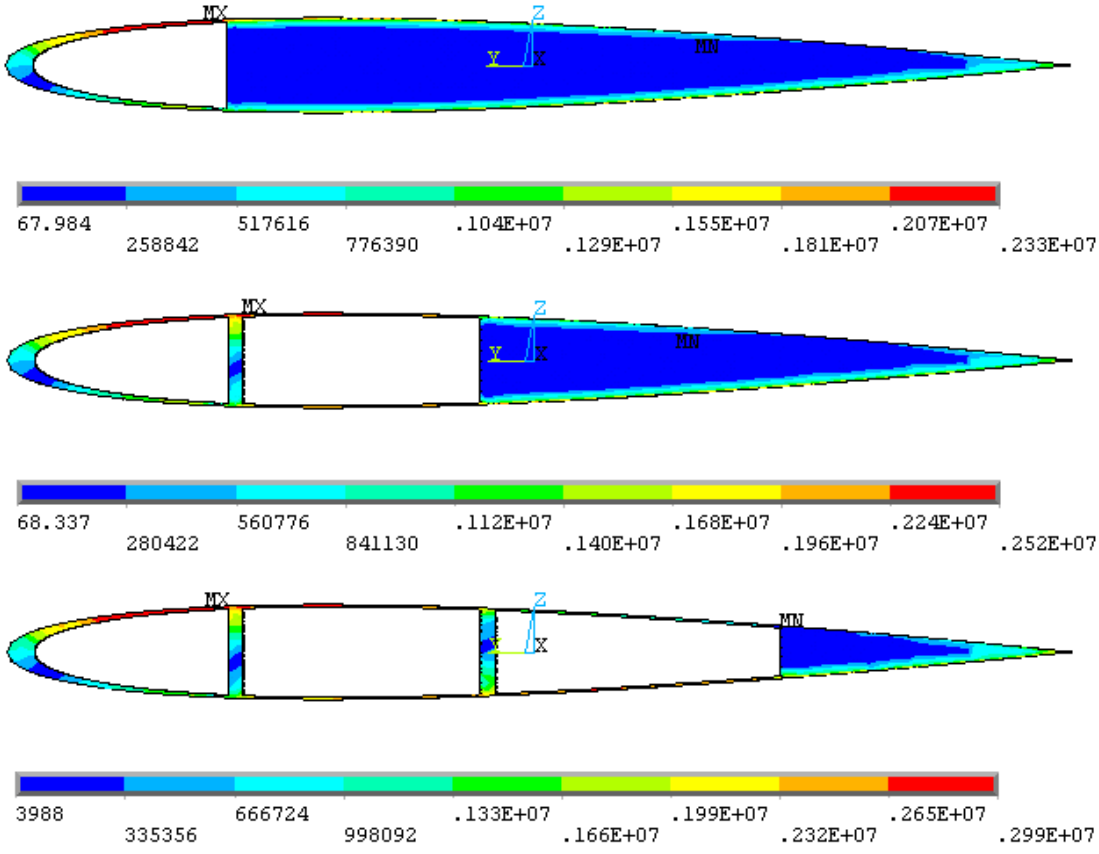

Figure 6.21: Von Mises stress for different inner designs

at 80% divergence dynamic pressure

6.1.5 Composite Skin

Until now, the isotropic material aluminum alloy 7075-T6 is used for the skin for all the models in DYMORE. To evaluate the influence of composite materials to the aeroelastic problems, the reinforcement of wing stiffness by layup design of the skin for the 15-foot cantilevered wing model is investigated. The roll maneuverability can be improved by increasing the torsional stiffness, and the torsional stiffness can be increased by varying ply angles without significant weight penalty, since the same materials are used. Table 6.5 shows four cases of composite skin designs [67, 79], and Figure 6.22 shows the example of layups description for Case 1. As before, aluminum alloy 7075-T6 is used for the skin and spar. Aluminum 5052 honeycomb is used for the core. The same ply thickness is used for all the models, and the color represented the same layup angle used for the layers in Figure 6.22. For example, Case 3 applied in Figure 6.22 means five 30° plies are used for the pink layer, five -45° plies are used for the blue layer, and five 30° plies are used for the purple layer.

Table 6.5: Description of composite skin design

	Layers	**Stacking Sequence**	**Ply Thickness (in)**
Case 1	9	$\{[45]_3, [-45]_3, [45]_3\}$	0.0053
Case 2	9	$\{[30]_3, [-45]_3, [30]_3\}$	0.0053
Case 3	15	$\{[30]_5, [-45]_5, [30]_5\}$	0.0053
Case 4	30	$\{[30]_{10}, [-45]_{10}, [30]_{10}\}$	0.0053

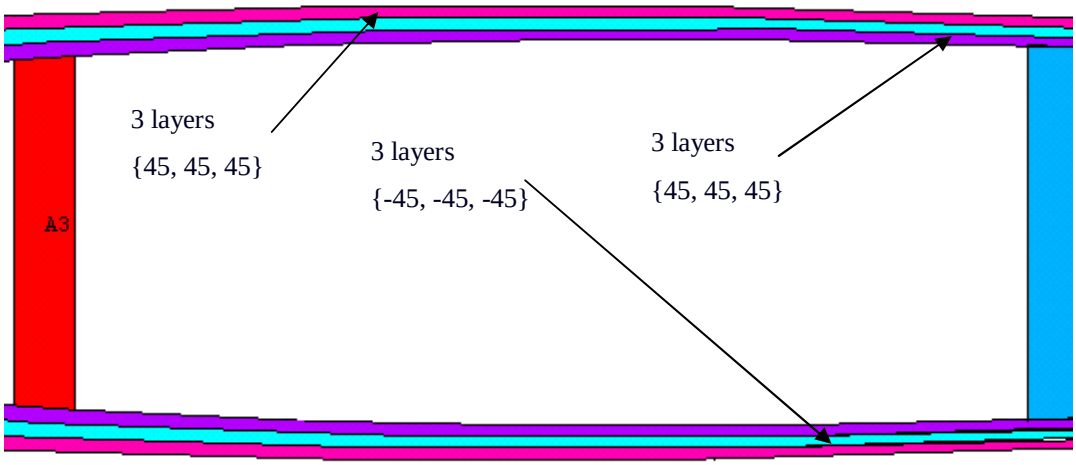

Figure 6.22: Schematic showing of composite skin design

Same as before, aileron effectiveness is defined as how much rolling moment can be generated up to 90% divergence normalized by the span of aileron, and results are reported in Table 6.6. First, comparing between Cases 1 and 2, both reversal and divergence dynamic pressures increase with increasing the torsional stiffness, although the difference is small because only six layup angles changed. Also, the resulting rolling moment per unit length of aileron increases slightly for Case 2. Comparing between Cases 2, 3, and 4, the torsional stiffness increases significantly by adding more layers, and results in dramatic increases in both reversal and divergence dynamic pressure. The post-reversal regime which can be utilized has widened a lot as well. There is no rule for the value of aileron effectiveness in the three cases, because the aileron effectiveness is defined as how much rolling moment can be generated up to 90% divergence with respect to unit length of aileron. The tip rotation for Case 4 is less than that for Case 3, which means the less deformation for Case 4. Based on the constitute law, less deformation results from less airloads distribution. Therefore, the design for Case 4 provides less rolling moment than Case 3, and the design for Case 3 can provide the most

rolling moment with respect to unit length of aileron within four cases. Note that the tip rotation for the four cases is far below the stall angle of attack for NACA 0009 airfoil.

Table 6.6: Comparisons of composite skin design for cantilevered wing

		15-foot Span Cantilevered Wing			
		Case 1	**Case 2**	**Case 3**	**Case 4**
Torsional Stiffness (lb-ft^2)		16,880	17,000	43,830	72,530
Reversal Dynamic Pressure (lb/ft^2)		197.93	198.90	508.55	834.97
Divergence Dynamic Pressure (lb/ft^2)		317.81	320.27	819.10	1224.94
Post-Reversal Regime (lb/ft^2)		119.88	121.37	310.55	389.97
90% Divergence Dynamic Pressure	**Tip Rotation (deg)**	-0.205	-0.206	-0.207	-0.086
	Aileron Effectiveness (lb-ft/ft)	-8.22	-8.32	-21.68	-16.21

6.1.6 Aeroelastic Tailoring

Aeroelastic tailoring is the design of wings using the directional properties of composite materials to optimize aeroelastic performance. Composite materials are anisotropic, which implies different material characteristics in different directions. It is easier to get insight of the behavior of composite wings by involving the bending-torsion coupling in the simple beam equation [47]. For anisotropic beams with bending-torsion coupling, the constitutive equation is

$$\begin{Bmatrix} S \\ T \\ M \end{Bmatrix} = \begin{bmatrix} GK_3 & GK_3 s_2 & 0 \\ GK_3 s_2 & GJ & -K \\ 0 & -K & EI_2 \end{bmatrix} \begin{Bmatrix} 2\gamma_{13} \\ \kappa_1 \\ \kappa_2 \end{Bmatrix} \tag{45}$$

where S is the shear force, T is the twisting moment, M is the bending moment, K is the bending-torsion coupling stiffness (having the same dimensions as EI_2 and GJ), GK_3 is the shearing stiffness, and s_2 is the offset from the reference line to the shear center. A positive K means that a positive bending deflection will be accompanied by a nose-up twist, which is normally destabilizing for cases with the elastic axis behind the aerodynamic center. Supposing that the reference line is located at the locus of shear centers for the uniform wing, the divergence dynamic pressure is

$$q_D = \frac{\frac{\pi^2}{4} GJ\left(1-\kappa^2\right)}{ecC_{l_\alpha} l^2 \left(1+\frac{3\pi^2}{76}\frac{l}{e}\frac{K}{EI_2}\right)} \tag{46}$$

where κ is the dimensionless parameter and it is

$$\kappa = \frac{K}{\sqrt{EI_2 GJ}} \tag{47}$$

With Eqn. (46) the divergence dynamic pressure can be determined with sufficient accuracy to ascertain its trend versus the elastic coupling parameter κ. To demonstrate the influence of the elastic coupling to the aeroelastic instability, the specific values of κ are substituted into Eqn. (46), and all the structural and aerodynamic properties are the same

as the uniform lifting surface model in Section 3.3.4. The analytical results are shown in Figure 6.23. Note that there is a limit to how much coupling can be achieved, as typically, $|\kappa| \leq 0.5$.

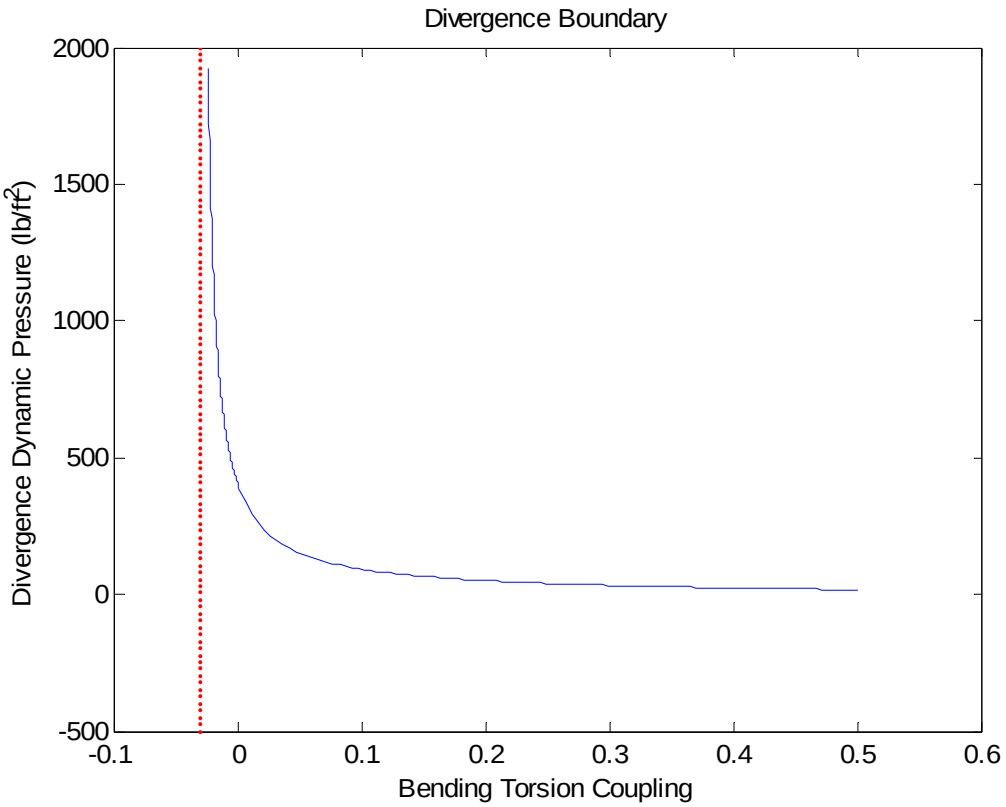

Figure 6.23: The trends of divergence dynamic pressure versus the bending-torsion coupling (analytical results)

From Figure 6.23, the plot represents the trends of divergence dynamic pressure with the reasonable range of κ. The red dashed line represents the boundary, which means crossing a regime in which divergence exists to one in which it does not, and κ is equal to -0.0313 here. Indeed, while κ is approaching this value from the right hand side, the

divergence dynamic pressure is getting larger and larger and finally the denominator of Eqn. (46) vanishes and the divergence becomes infinite. Also, beyond this line, the divergence dynamic pressure becomes negative. Thus in either case divergence is impossible. Reviewing Section 3.3.4, the bending-torsion coupling is involved by artificially adding the bending-torsion stiffness into the DYMORE aeroelastic model to evaluate the trends of divergence dynamic pressure herein, and the numerical results are shown in Figures 6.24.

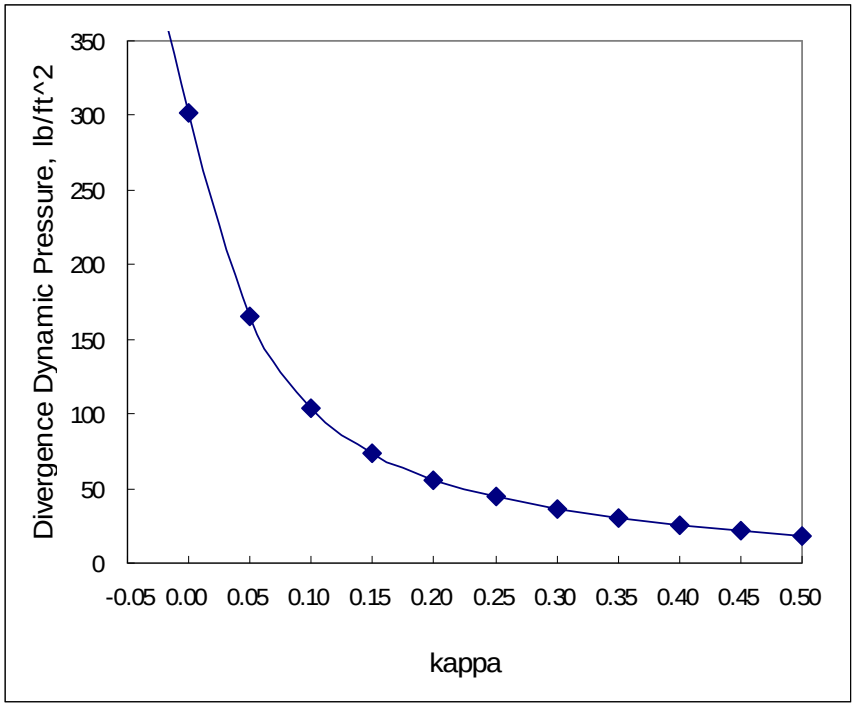

Figure 6.24: The trends of divergence dynamic pressure versus the bending-torsion coupling (numerical results)

Similarly, the reasonable divergence dynamic pressures with the specific values of κ are shown in this plot. From Figure 6.24, the higher bending-torsion coupling results in the lower divergence dynamic pressure. Therefore, the positive κ did destabilize for cases with the elastic axis behind the aerodynamic center, which agrees well with the previous

conclusion. Around the boundary for the divergence approaching the infinity, κ is equal to -0.035 in this case. The trend of the divergence dynamic pressure is similar to the analytical results, and the results show the negative κ can improve the aeroelastic instability. Specially note the purpose of this dissertation is to take advantage of the post-reversal regime. The cases with the negative divergence dynamic pressure mean that no divergence occurs, but reversal still may occur. One can still have a post-reversal design for those cases.

After illustrating the influence of the bending-torsion coupling to the aeroelastic instability, the focus is moved to how the elastic coupling affects aileron reversal. The model in Section 4.1 is investigated again with bending-torsion coupling. Figures 6.25 and 6.26 represent the cases for 10-foot span and 15-foot span, respectively.

Results show the negative bending-torsion coupling can improve the divergence dynamic pressure significantly, but the reversal dynamic pressure has almost no change with varying the elastic coupling. The resulting wider post-reversal regime can be utilized for the higher negative bending-torsion coupling. It is clear to check how much rolling moment per unit length of aileron can be generated at 80% divergence dynamic pressure shown in Figure 6.27. The more rolling moment can be generated by involving larger negative elastic coupling. Also higher level of aileron effectiveness can be achieved for lower-aspect-ratio wing, which agrees with the previous conclusion. To validate the results, the tip rotation at the highest dynamic pressure is -5.44 degrees for 10-foot case and -2.84 degrees for 15-foot case, both of which are far below the stall angle of attack for NACA 0009.

Specially note that the wing cross-sectional distortion is neglected in this study. Although VABS can report the in-plane warping resulting from the applied aerodynamic

loads, the change of the wing section shape is extremely small, of the order of the maximum strain and a characteristic length of the wing section, which is 1-foot chord in this study. Therefore, the change will be less than 0.1% relative to the undeformed shape of the wing section. Using the deformed shape back to XFOIL to update the aerodynamic coefficients, such as lift, moment, and drag coefficients used in this study, XFOIL cannot accurately capture the change in lift, drag, an pitching moment coefficients for such a small change in shape. Moreover, such small changes in the aerodynamic coefficients cannot significantly influence the results. To reach a level of cross-section deformation sufficiently large to measurably affect aerodynamic coefficients, special efforts must be undertaken to design the wing section for such deformation. An example of such a design is the chiral cellular materials discussed in [106]. Such additional study is appropriate for future work.

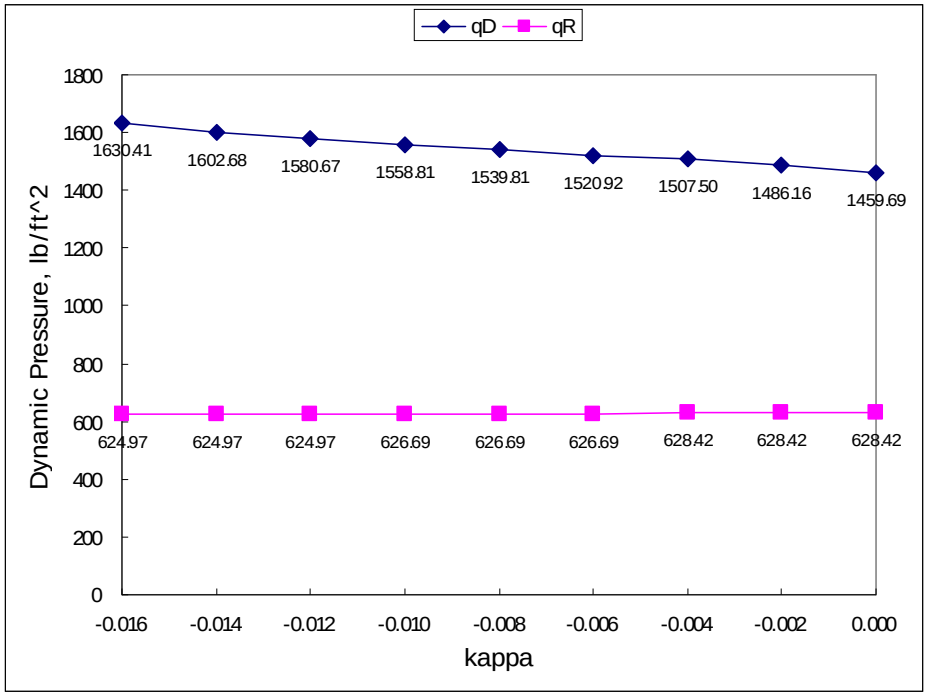

Figure 6.25: The trends of aeroelastic phenomena versus the bending-torsion coupling for cantilevered wing (wingspan = 10 ft)

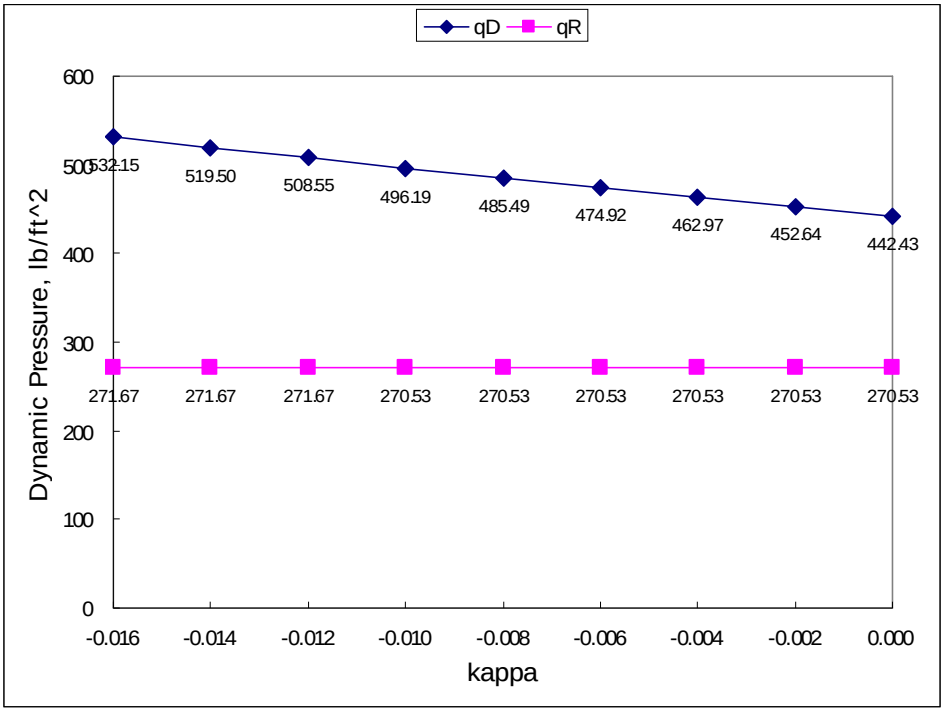

Figure 6.26: The trends of aeroelastic phenomena versus the bending-torsion coupling for cantilevered wing (wingspan = 15 ft)

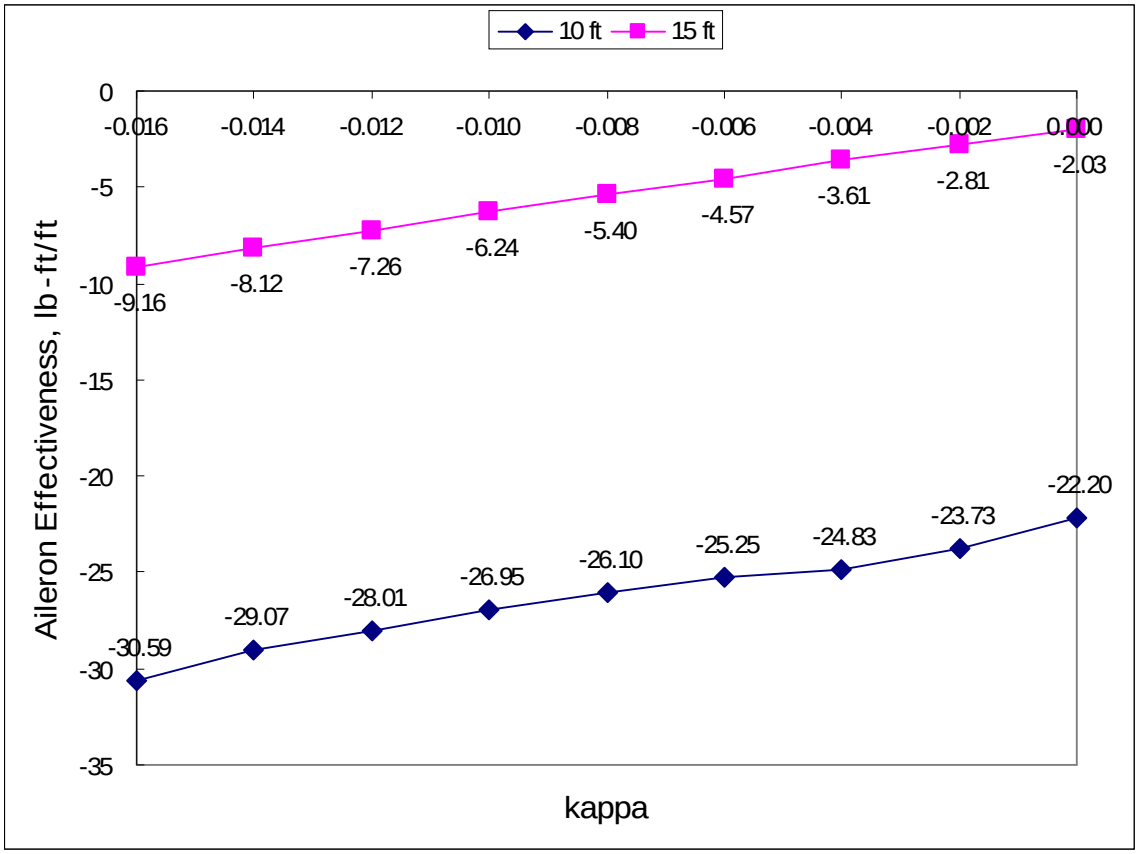

Figure 6.27: The aileron effectiveness versus the bending-torsion coupling for cantilevered wing (at 80% divergence)

The approach here is to involve the bending-torsion coupling by artificially adding the bending-torsion stiffness into the aeroelastic model, which means the other structural properties, such as torsional stiffness, did not change. On the other hand, the tested model is uniform cantilevered wing, and the major factors affecting the aileron reversal are GJ and C_{M_β} as mention before. Therefore, the bending-torsion coupling did not influence the aileron reversal much, since these parameters are kept the same.

6.1.7 Airfoil Selection

NACA 0009 airfoil is used for most of the models in XFOIL and DYMORE, except for the verifications presented in Chapter 5. To evaluate the effects of airfoil shape to the aeroelastic problems [19, 68, 96], several airfoils based on the literature [21, 98, 100, 105] are chosen as the wing section in the 15-foot cantilevered wing model. To ensure the consistency between the aerodynamic and structural models, aerodynamic data from XFOIL and structural properties from VABS are put into DYMORE together to build up the aeroelastic model. The aerodynamic data is generated based on single airfoil with 3 degrees of aileron deflection, where the hinge location is at 80% chord shown as Figures 6.28, 6.29, and 6.30. Figure 6.28 shows five NACA airfoils selected for analysis with the deflected aileron, and Figure 6.29 shows five other airfoils selected for the analyses with the deflected aileron. Figure 6.30 shows the two NACA airfoils used for F/A-18, which are also investigated here. Besides, the structural properties are generated based on the associated airfoils with solid wing section.

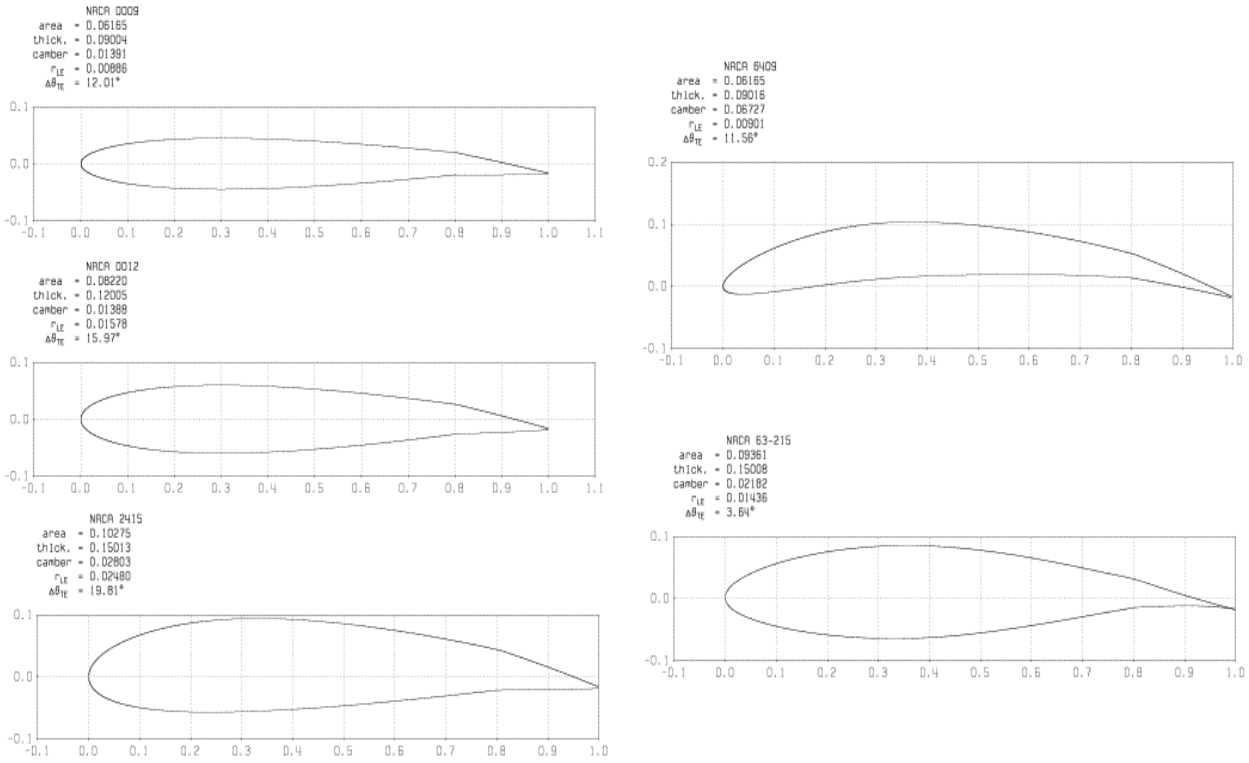

Figure 6.28: Five kinds of NACA series airfoils (NACA 0009, NACA 0012, NACA 2415, NACA 6409, and NACA 63215)

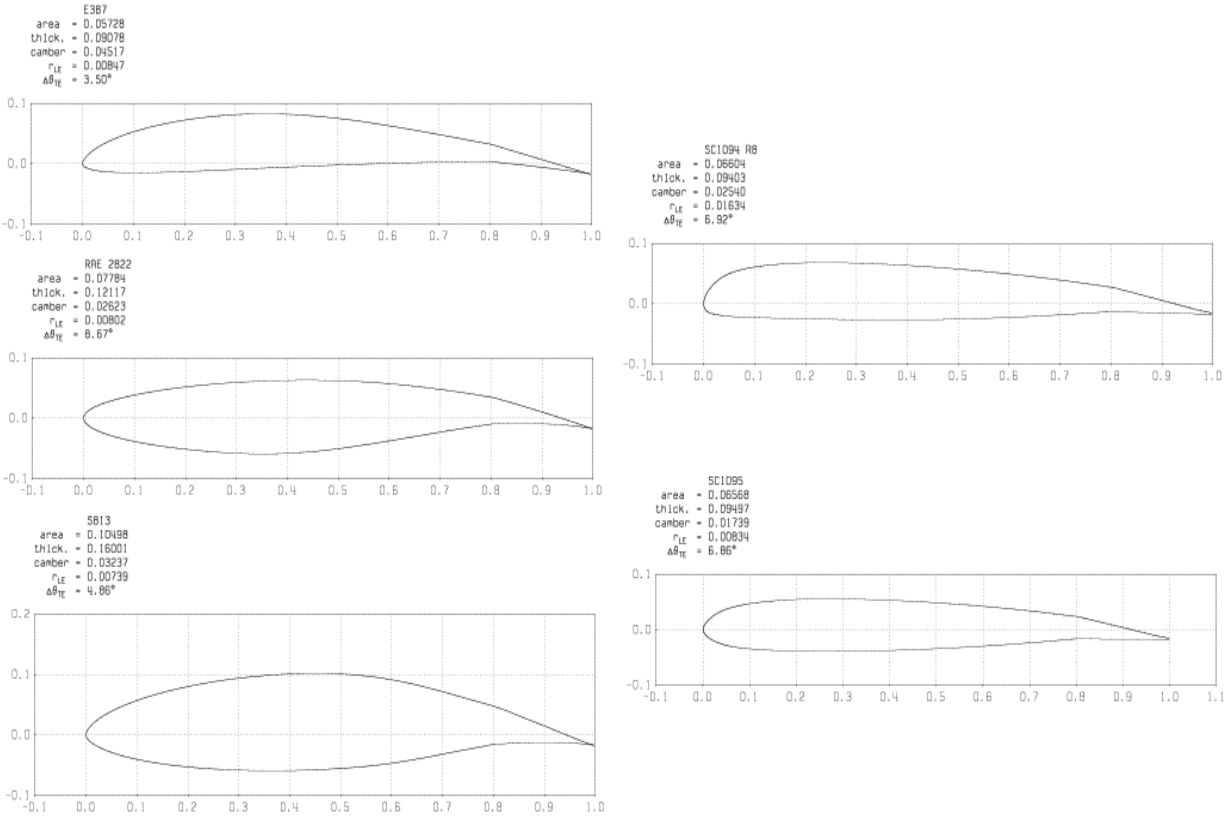

Figure 6.29: Airfoils selection (Eppler387, RAE2822, S813, SC1094r8, and SC1095)

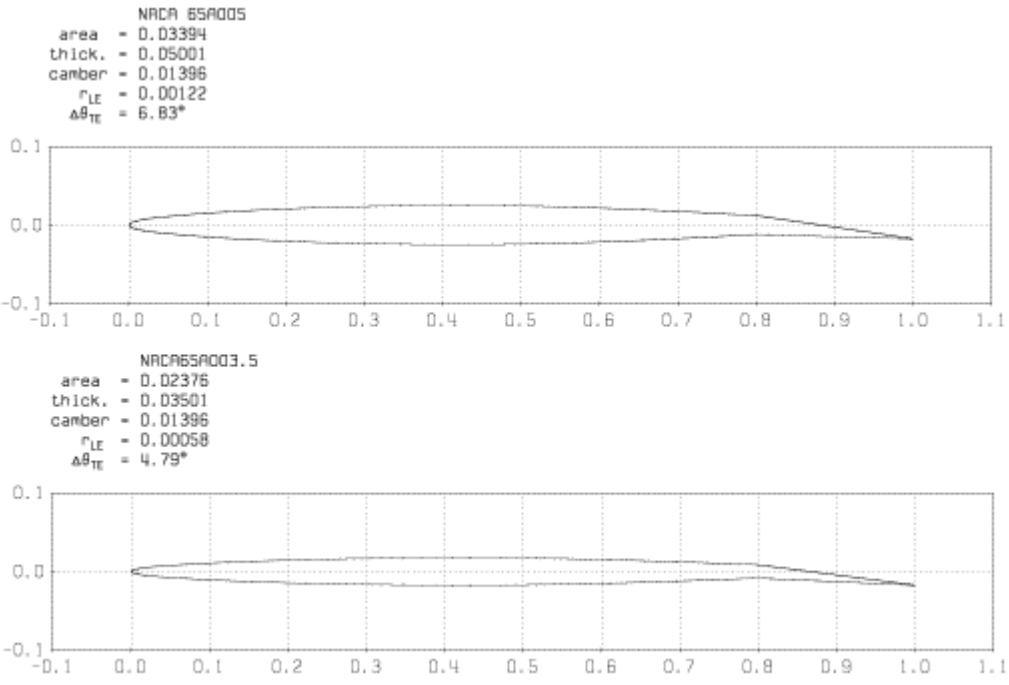

Figure 6.30: F/A-18 airfoils (NACA 65A005 for root; NACA 65A003.5 for tip)

Results shown in Table 6.7 consist of aerodynamic characteristics and the investigations of aeroelastic phenomena for the different airfoils. The aileron effectiveness is defined as how much rolling moment can be provided with 3 degrees of aileron deflection normalized by the span of aileron at certain dynamic pressure. For the purpose of this dissertation, the lower reversal dynamic pressure and the higher divergence dynamic pressure are to be explored, which means the wider post-reversal regime and higher rolling moment can be utilized. Although the investigations here are just the initial analyses for the simple structural model, the results may provide guidance for future research about these aeroelastic phenomena. First, comparing NACA 0009 and NACA 0012, the latter has high lift-curve slope and smaller magnitude of C_{M_β}, so it has lower reversal and higher divergence dynamic pressures, which implies that it fits well with the objective. Second, NACA 2415 and NACA 63215 airfoils are not suitable choices for the enhancement of roll maneuverability because of less rolling moment can be generated within the post-reversal regime. Third, comparing between two airfoils used for F/A-18, NACA 65A005 and NACA 65A003.5, they have similar post-reversal regime, but the former one has slightly higher divergence and reversal dynamic pressures. Fourth, RAE 2822 airfoil has the smallest magnitude of C_{M_β} within all the airfoils here, and the aircraft with RAE 2822 airfoil can get highest rolling moment (though negative) at 350 lb/ft^2 of dynamic pressure. Lastly, RAE 2822, SC 1094r8, NACA 65A005, and NACA 65A003.5 airfoils are better options for the present study, since they can provide more rolling moment within the post-reversal regime. Note that for different definition of aileron effectiveness, the results may be different. In fact, each airfoil has its advantages from an aerodynamic point of view. The further analysis about the rolling aircraft model

will be discussed in Section 6.2.7.

Table 6.7: Comparisons between airfoil selections for cantilevered wing

Airfoil		**NACA 0009**	**NACA 0012**	**NACA 2415**	**NACA 6409**	**NACA 63215**	**Eppler 387**
Linear Regime	C_{L_α}	6.23	6.44	6.37	6.26	6.36	6.44
	C_{M_β}	-0.68	-0.63	-0.61	-0.57	-0.61	-0.60
Reversal Dynamic Pressure (lb/ft^2)		287.81	275.09	278.53	287.81	285.48	284.31
Divergence Dynamic Pressure (lb/ft^2)		423.77	516.36	597.69	468.92	530.56	467.43
Dynamic Pressure 350 lb/ft^2	**Aileron Effectiveness (lb-ft/ft)**	-26.14	-23.27	-17.93	-20.84	-18.68	-23.02
Airfoil		**RAE 2822**	**S 813**	**SC 1094r8**	**SC 1095**	**NACA 65A005**	**NACA 65A003.5**
Linear Regime	C_{L_α}	6.09	5.43	6.57	6.54	6.55	6.41
	C_{M_β}	-0.53	-0.63	-0.67	-0.66	-0.63	-0.63
Reversal Dynamic Pressure (lb/ft^2)		279.68	267.14	279.68	279.68	276.23	275.09
Divergence Dynamic Pressure (lb/ft^2)		382.25	561.17	418.11	462.97	413.89	412.49
Dynamic Pressure 350 lb/ft^2	**Aileron Effectiveness (lb-ft/ft)**	-43.81	-20.43	-32.94	-25.59	-35.64	-35.69

6.2 Post-Reversal Behavior for Rolling Aircraft

6.2.1 Aspect Ratio

Similarly, the same model for rolling aircraft with the solid wing section as Section 4.2.2, i.e. given 1 degree of angle of attack and 1 degree of antisymmetric aileron deflection, is tested for three kinds of aspect ratio as Section 6.1.1. For rolling aircraft, it

is safer to operating the aircraft at lower dynamic pressure than the cantilevered wing case since it is closer to a practical case. Therefore, the desired operating dynamic pressure is assumed to be up to 70% divergence here. In order to check the variation for different rolling moment components clearly, Figure 6.31 only represents the dynamic pressure up to 60% divergence for $\mathcal{AR}$ = 10 case. The divergence dynamic pressure for this case is 991.11 lb/ft^2, and reversal occurs at 226.30 lb/ft^2 of dynamic pressure. At 70% divergence dynamic pressure, the steady roll rate can reach -6.51 deg/s as shown in Figure 6.32, and the associated Von Mises stress is shown as Figure 6.33. As usual, the highest stress is happened around the wing skin but still below the yield stress for Aluminum 7075-T6, which is 1.15×10^7 lb/ft^2. The factor of safety is 1.30 for the desired operating dynamic pressure in this case.

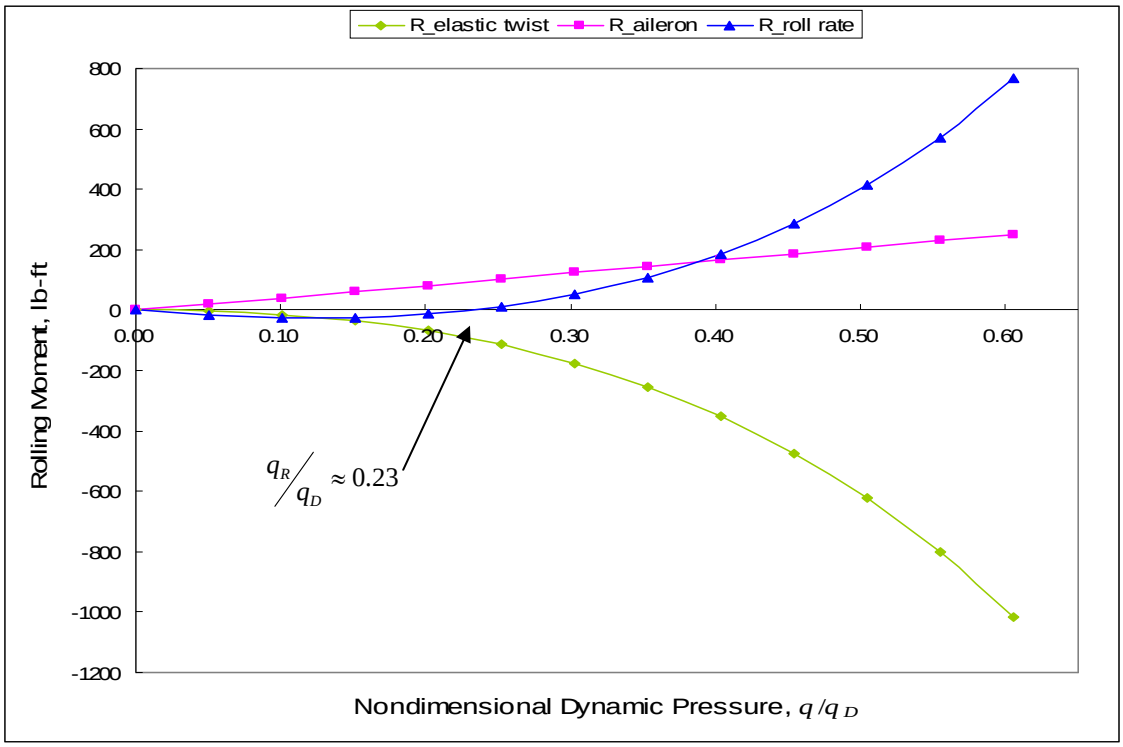

Figure 6.31: Variation of the components of the rolling moment up to 60% divergence dynamic pressure ($\mathcal{AR}$ = 10)

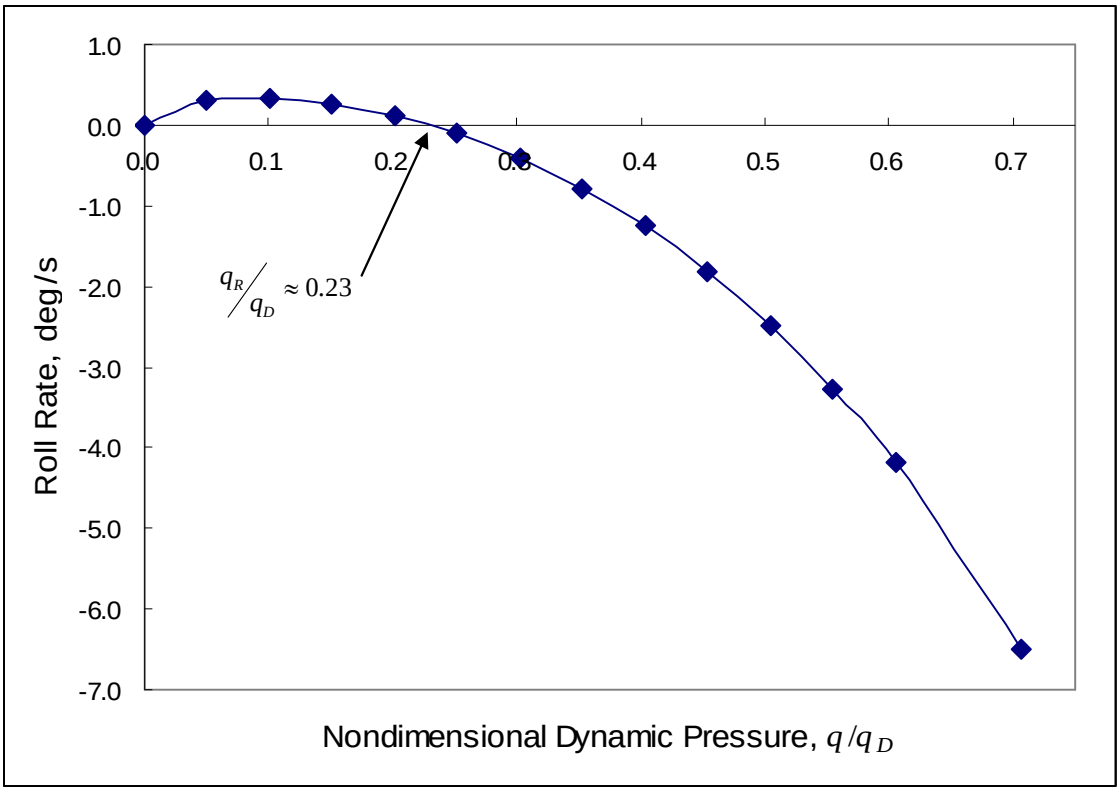

Figure 6.32: Steady roll rate versus nondimensional dynamic pressure

(10-foot wingspan with solid wing section)

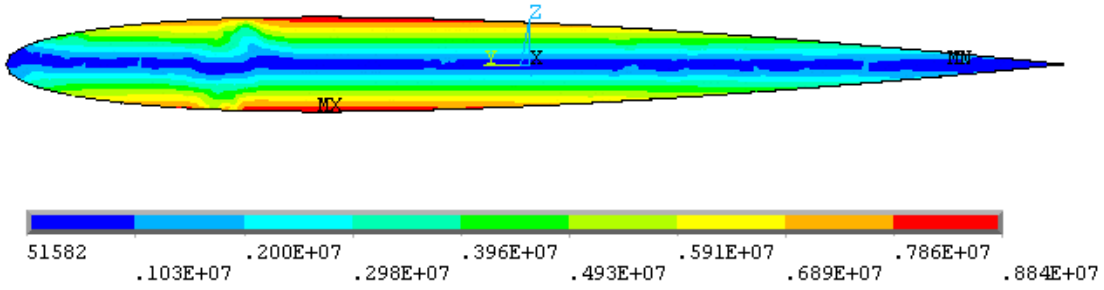

Figure 6.33: Von Mises stress at 70% divergence dynamic pressure

for rolling aircraft ($\mathcal{AR}$ = 10)

For the $\mathcal{AR}$ = 15 model of rolling aircraft, the divergence dynamic pressure is 342.87 lb/ft^2, and reversal occurs at 82.42 lb/ft^2 dynamic pressure. Similarly, in order to check the variation for different rolling moment components clearly, Figure 6.34 only

represents the dynamic pressure up to 60% divergence for the $\mathcal{AR}$ = 15 case.

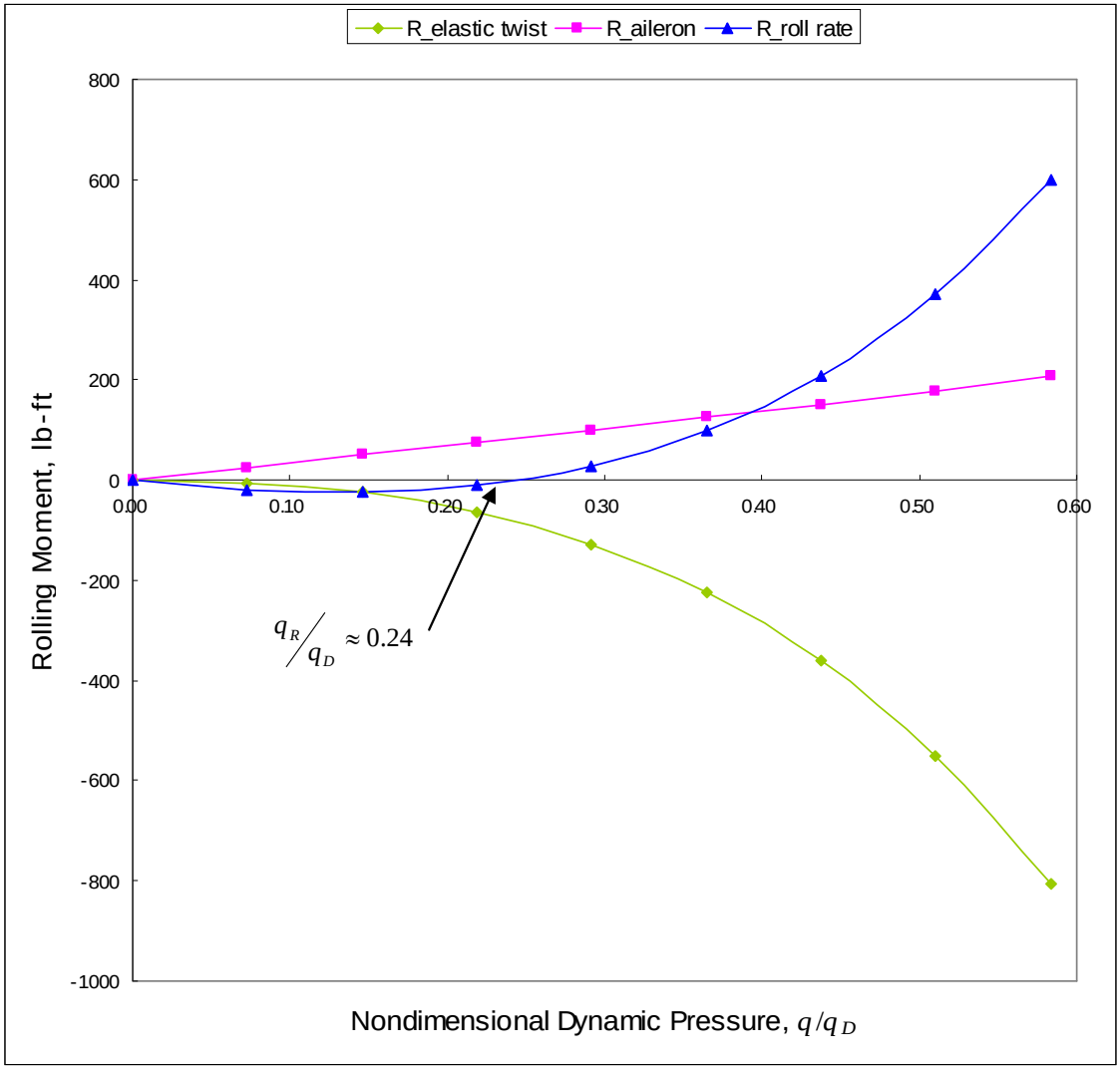

Figure 6.34: Variation of the components of the rolling moment up to 60% divergence dynamic pressure ($\mathcal{AR}$ = 15)

The steady roll rate can reach -3.30 deg/s at 70% divergence dynamic pressure as shown in Figure 6.35, and the associated Von Mises stress is shown as Figure 6.36. The highest stress is 7.47×10^6 lb/ft^2 for this case and the factor of safety can be 1.54 for the desired operating dynamic pressure.

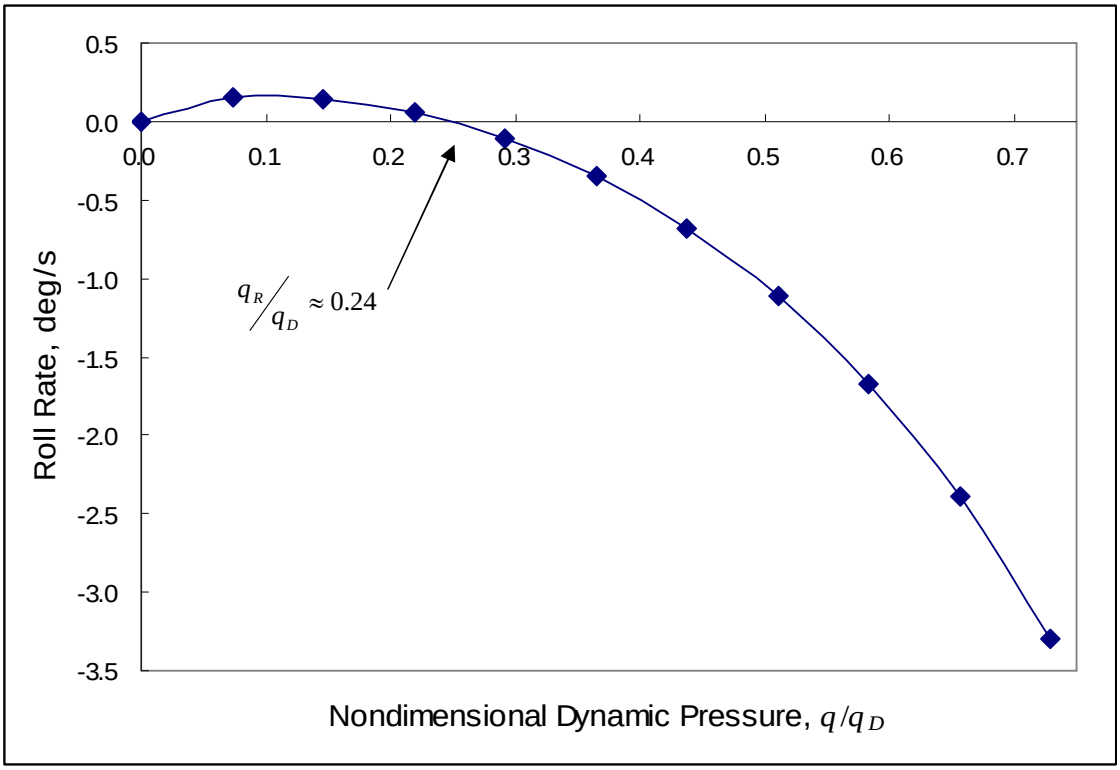

Figure 6.35: Steady roll rate versus nondimensional dynamic pressure

(15-foot wingspan with solid wing section)

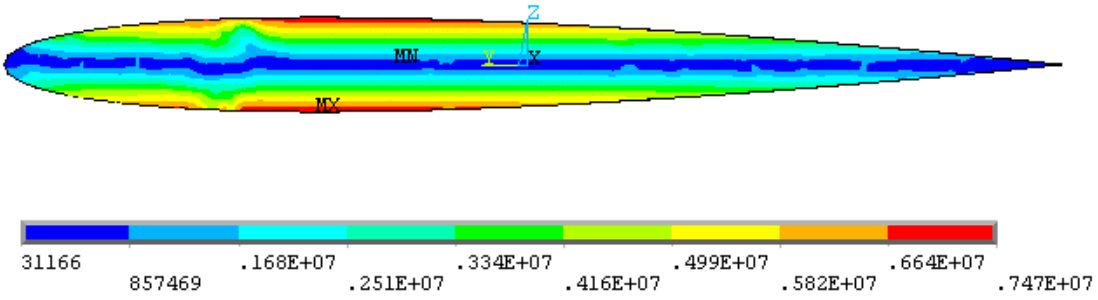

Figure 6.36: Von Mises stress at 70% divergence dynamic pressure

for rolling aircraft ($\mathcal{AR}$ = 15)

Table 6.8: Comparisons of aspect ratio for rolling aircraft

Aspect Ratio	Reversal Dynamic Pressure (lb/ft^2)	Divergence Dynamic Pressure (lb/ft^2)	70% Divergence Dynamic Pressure (lb/ft^2)			
			Tip Rotation for the Right Wing (deg)	Trim Angle of Attack (deg)	Roll Rate, p (deg/s)	Aileron Effectiveness, (deg/s-ft)
10.0	226.30	991.11	3.057	4.021	-6.51	-0.33
12.5	127.30	582.61	3.624	4.725	-4.51	-0.18
15.0	82.42	342.87	4.099	4.866	-3.30	-0.11
Note: chord = 1 ft						

Table 6.8 shows the comparisons for the rolling aircraft with different aspect ratio. Obviously, the post-reversal regime has shrunk for the $\mathcal{AR}$ = 15 case, and the aileron effectiveness, which is defined as how much roll rate can be generated up to 70% divergence normalized by the span of aileron, is lowest within three cases. The model with $\mathcal{AR}$ = 10 can generate highest roll rate for aircraft rolling. This agrees with the results for cantilevered wing model.

6.2.2 Hinge Location

For the rolling aircraft model, several horizontal hinge locations are investigated, and the range is from 0.7 to 0.95 ft from the leading edge. The aerodynamic coefficients generated are then put into the DYMORE model for $\mathcal{AR}$ = 10 to build up full range angles of attack ($-180^\circ \le \alpha \le 180^\circ$) for analyses. Results in Table 6.9 show that aeroelastic boundaries change with varying the horizontal hinge locations because effective camber changes. The changing of effective camber results in the changing of divergence and reversal dynamic pressures due to different airtables used in DYMORE.

Table 6.9: Effects of horizontal hinge locations for critical speeds and aileron effectiveness for rolling aircraft

Horizontal Hinge Location (ft)	**0.7**	**0.75**	**0.8**	**0.85**	**0.9**	**0.95**
Reversal Dynamic Pressure (lb/ft^2)	409.16	551.77	621.99	671.99	637.98	399.52
Divergence Dynamic Pressure (lb/ft^2)	1499.48	1520.92	1526.31	1572.45	1622.06	1470.25
Trim Angle of Attack (deg)	4.546	4.622	4.763	4.930	5.225	5.190
Aileron Effectiveness (deg/s-ft)	-0.66	-0.44	-0.35	-0.25	-0.21	-0.25
Note: Operating Dynamic Pressure = 1000 lb/ft^2						

Figure 6.37 shows how horizontal hinge location affects aeroelastic boundaries. Indeed, effective camber of an airfoil changes with respect to different hinge location, which tends to affect aerodynamic coefficients used for the airtable in DYMORE. Figure 6.38 shows the variation for different rolling moment components up to 80% divergence for the model with horizontal hinge location at 70% chord, and the resulting roll rate is shown as Figure 6.39. Comparing the six cases in Table 6.9, aileron effectiveness, defined as how much roll rate can be generated at 1000 lb/ft^2 of operating dynamic pressure normalized by the span of aileron, versus hinge location is plotted as Figure 6.40. Unlike cantilevered wing, the hinge location at 70% chord can generate the most roll rate for rolling. Note again for different definition of aileron effectiveness, the results may be different. Aileron effectiveness is determined by using the resulting rolling moment for the cantilevered wing. Instead, aileron effectiveness is determined by the combination of three different sources of rolling moment for the rolling aircraft case, and the moment is caused by rigid aileron deflection, elastic wing twist, and roll rate, respectively. In addition, rather than reversal occurs while the rolling moment vanishes for the cantilevered wing case, reversal occurs while the moment resulting from the roll

rate vanishes for the rolling aircraft case.

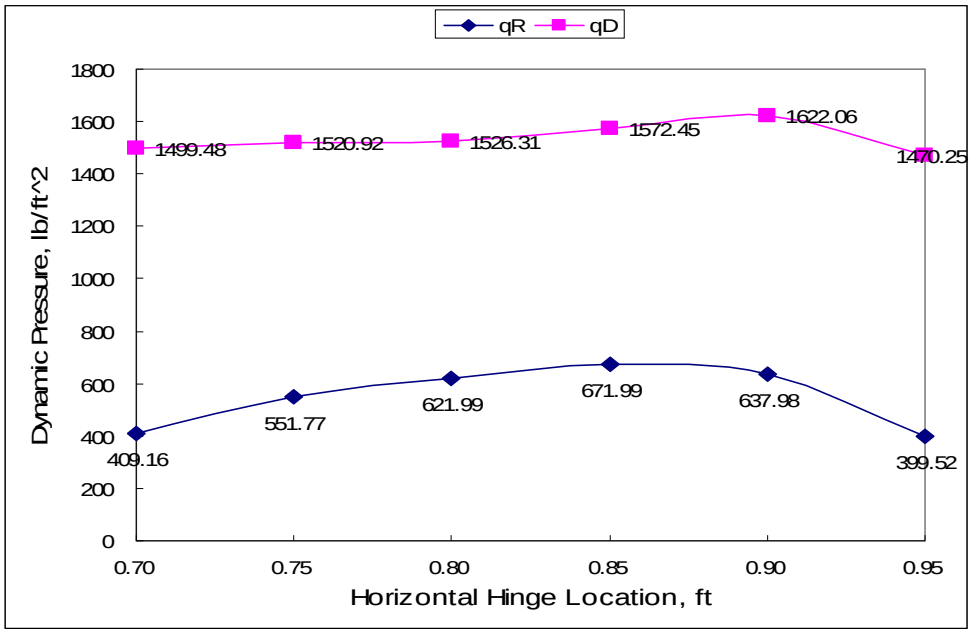

Figure 6.37: Aeroelastic boundaries versus horizontal hinge locations for rolling aircraft (operating dynamic pressure = 1000 lb/ft^2)

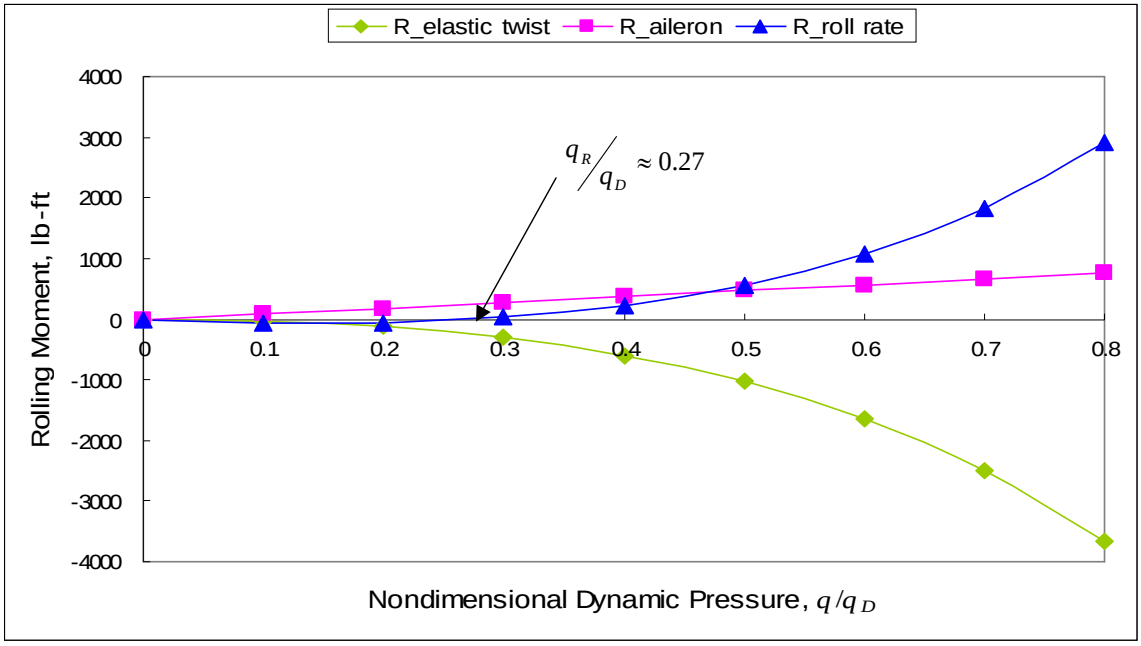

Figure 6.38: Variation of the components of the rolling moment up to 80% divergence dynamic pressure (horizontal hinge location at 70% chord)

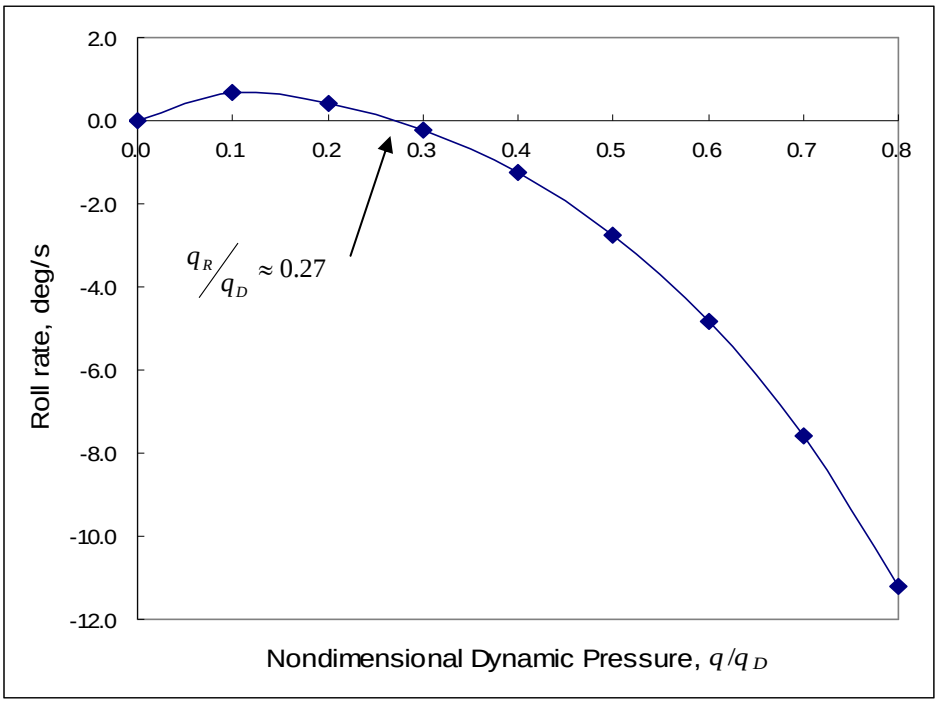

Figure 6.39: Steady roll rate versus nondimensional dynamic pressure (horizontal hinge location at 70% chord)

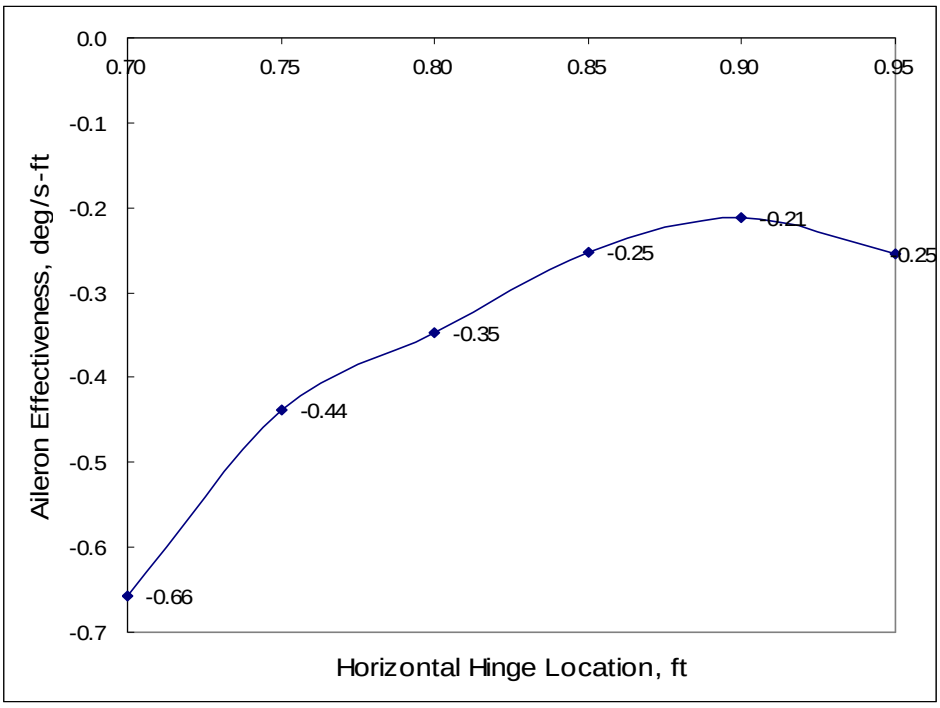

Figure 6.40: Aileron effectiveness versus horizontal hinge locations for rolling aircraft (operating dynamic pressure = 1000 lb/ft^2)

6.2.3 Airfoil Dimension

More lift will be generated for larger planform area, which tends to create more rolling moment for a flying aircraft while deflecting ailerons antisymmetrically. Same as cantilevered wing case, to investigate the effects of airfoil dimension to the aeroelastic problems, three different section dimensions are evaluated, which are 1.0, 1.25, and 1.5 foot chord, respectively. For all the rolling aircraft models with solid wing section and 15-foot wing span, the hinge is located at 80% chord line with given Mach number 0.1, Reynolds number 3×10^6, and angle of attack 2 degrees.

Aspect ratio changes due to varying the chord but keeping the wing span constant. Figure 6.41 shows the variation for different rolling moment components up to 80% divergence for the model with 1.25-foot chord, and the resulting roll rate is shown as Figure 6.42. Table 6.10 shows the comparisons between three kinds of chord, resulting in three different aspect-ratio wings. From aerodynamic point of view, the only effect is from the wing's aspect ratio. The more 3-D effects, like downwash velocity, happened at the wing tip, since the chord increases in this case. On the other hand, the sectional properties are updated with varying the chord, and that tends to increase the stiffness for the lower aspect-ratio wing. As the previous conclusion, both reversal and divergence dynamic pressures increase with increasing torsional stiffness. Therefore, there are higher reversal and divergence, and wider post-reversal regime for the model with 1.5-foot chord. In addition, higher negative roll rate per unit length of aileron, which makes the aircraft perform negative rolling with respect to the rolling axis, can be generated for the model with 1.5-foot chord. Note the tip rotations of both wings for three models are acceptable and far below the stall angle of attack.

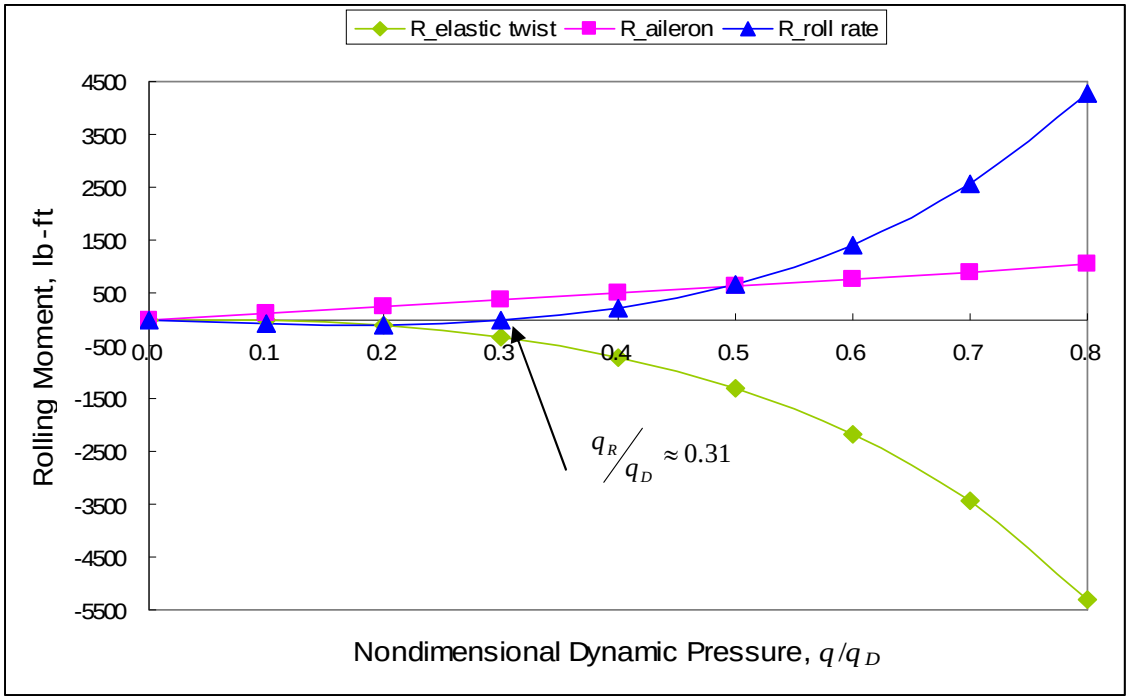

Figure 6.41: Variation of the components of the rolling moment up to 80% divergence dynamic pressure (1.25-foot chord)

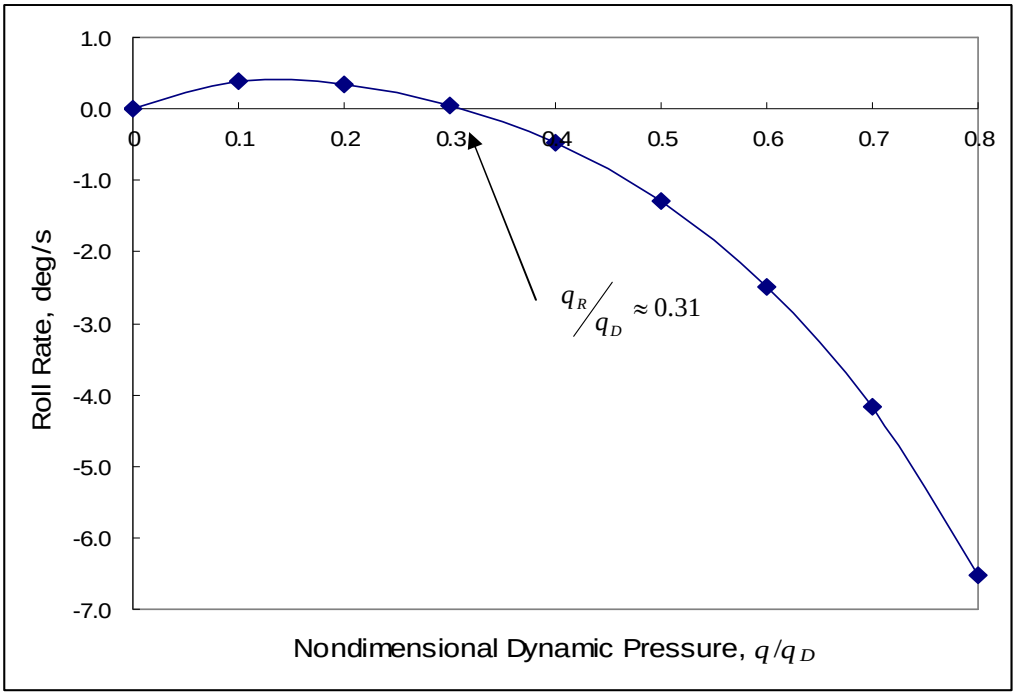

Figure 6.42: Steady roll rate versus nondimensional dynamic pressure (1.25-foot chord)

Table 6.10: Comparisons of airfoil dimension for rolling aircraft

Chord (ft)		1.00	1.25	1.50
$\mathcal{AR}$		15	12	10
Torsional Stiffness (lb-ft^2)		23,900	58,350	121,000
Reversal Dynamic Pressure (lb/ft^2)		99.26	261.66	579.23
Divergence Dynamic Pressure (lb/ft^2)		342.87	840.96	1638.77
80% Divergence Dynamic Pressure	**Tip Rotation, deg (right wing)**	3.419	3.456	3.215
	Trim Angle of Attack (deg)	5.718	5.773	5.370
	Aileron Effectiveness (deg/s-ft)	-0.068	-0.103	-0.105

6.2.4 Wing Section Inner Structures

So far, the solid wings are used to most of the rolling aircraft models, except for the simple inner design of the wing discussed in Section 4.2.4. To simulate more realistic wings, the same cases of inner design for the cantilevered wing model are investigated. In addition, isotropic materials are used to reduce the weight but increase the stiffness [16, 20, 78]. Aluminum alloy 7075-T6 is used for the skin and spar. Aluminum 5052 honeycomb is used for the core [49].

Table 6.11 shows the comparisons between three inner designs for two cases of rolling aircraft model, which has 10-foot and 12.5-foot span, respectively. The sectional mass decreases with increasing cells, but the torsional stiffness increases instead due to stiffer material used in the locations of the spar. Results show both reversal and divergence dynamic pressures increase with increasing torsional stiffness. Unlike the cantilevered cases, at 80% divergence, the model with one cell has higher negative roll

rate per unit length of aileron due to larger tip rotation. But by comparing the same inner design between two spans, the magnitude of aileron effectiveness for the 10-foot case, which is structurally stiffer, is higher, and this agrees well with the previous results. To check if the models will encounter stall, the tip rotations for the right wing at 80% divergence dynamic pressure are listed in Table 6.11.

Active Aeroelastic Wing Technology turns wing aeroelastic flexibility into a net benefit through use of multiple leading- and trailing-edge control surfaces. The main objective of this idea is to alleviate the weight penalty for the traditional design with the reinforcement of the wing structures. The weight of the wings can be dramatically decreased by multiple cells inner design, but the stiffness could be reduced in the meantime. To maintain the required stiffness of the wings, even higher, composite skin design, such as material choosing and layup design, will be discussed in the next section.

Table 6.11: Comparisons of wing section inner design for rolling aircraft

		10 ft			**12.5 ft**		
		1 Cell	**2 Cells**	**3 Cells**	**1 Cell**	**2 Cells**	**3 Cells**
Sectional Mass (slug/ft)		0.28	0.18	0.08	0.28	0.18	0.08
Torsional Stiffness (lb-ft^2)		14,060	17,060	24,340	14,060	17,060	24,340
Reversal Dynamic Pressure (lb/ft^2)		164.61	202.27	290.85	93.63	114.34	163.67
Divergence Dynamic Pressure (lb/ft^2)		351.87	418.11	556.28	214.76	255.99	342.87
80% Divergence Dynamic Pressure	**Tip Rotation, deg (right wing)**	-1.500	-1.467	-1.360	-1.875	-1.736	-1.575
	Trim Angle of Attack (deg)	2.742	2.886	2.931	3.215	3.386	3.438
	Aileron Effectiveness (deg/s-ft)	-0.0313	-0.0308	-0.0239	-0.0227	-0.0181	-0.0128

6.2.5 Composite Skin

To evaluate the influence of composite materials to the aeroelastic problems, the reinforcement of wing stiffness by layup design of the skin for the rolling aircraft model is investigated. Use the same composite materials and the same composite skin designs shown in Table 6.5.

First, comparing between Cases 1 and 2 in Table 6.12, both reversal and divergence dynamic pressures increase with increasing the torsional stiffness, although the difference is small because only six layup angles changed. Comparing between Cases 2, 3, and 4, the torsional stiffness increases significantly by adding more layers, and results in dramatic increases in both reversal and divergence dynamic pressure. The post-reversal regime which can be utilized has widened a lot as well. Here the aileron effectiveness is defined as how much roll rate can be generated for unit length of aileron. Results up to 70% divergence show Case 3 can provide highest roll rate within the four cases, although its torsional stiffness is not highest. To evaluate if the structural design can sustain such high airloads generated during the post-reversal regime, the stress distribution for the four cases is shown in Figure 6.43. Although the highest stress happened in the four cases is below the yield stress of aluminum alloy 7075-T6, the highest stress for Case 4 is extremely close to the yield stress. It is a dangerous structural design, and the better choice of composite material should be investigated in the future.

Table 6.12: Comparisons of composite skin design for rolling aircraft

		10-foot Span Rolling Aircraft			
		Case 1	**Case 2**	**Case 3**	**Case 4**
Torsional Stiffness (lb-ft^2)		16,880	17,000	43,830	72,530
Reversal Dynamic Pressure (lb/ft^2)		205.02	206.61	552.79	951.10
Divergence Dynamic Pressure (lb/ft^2)		423.77	425.19	1100.35	1608.20
Post-Reversal Regime (lb/ft^2)		218.75	218.58	547.56	657.10
70% Divergence Dynamic Pressure	**Trim Angle of Attack (deg)**	2.664	2.657	2.659	2.457
	Aileron Effectiveness (deg/s-ft)	-0.048	-0.047	-0.066	-0.035

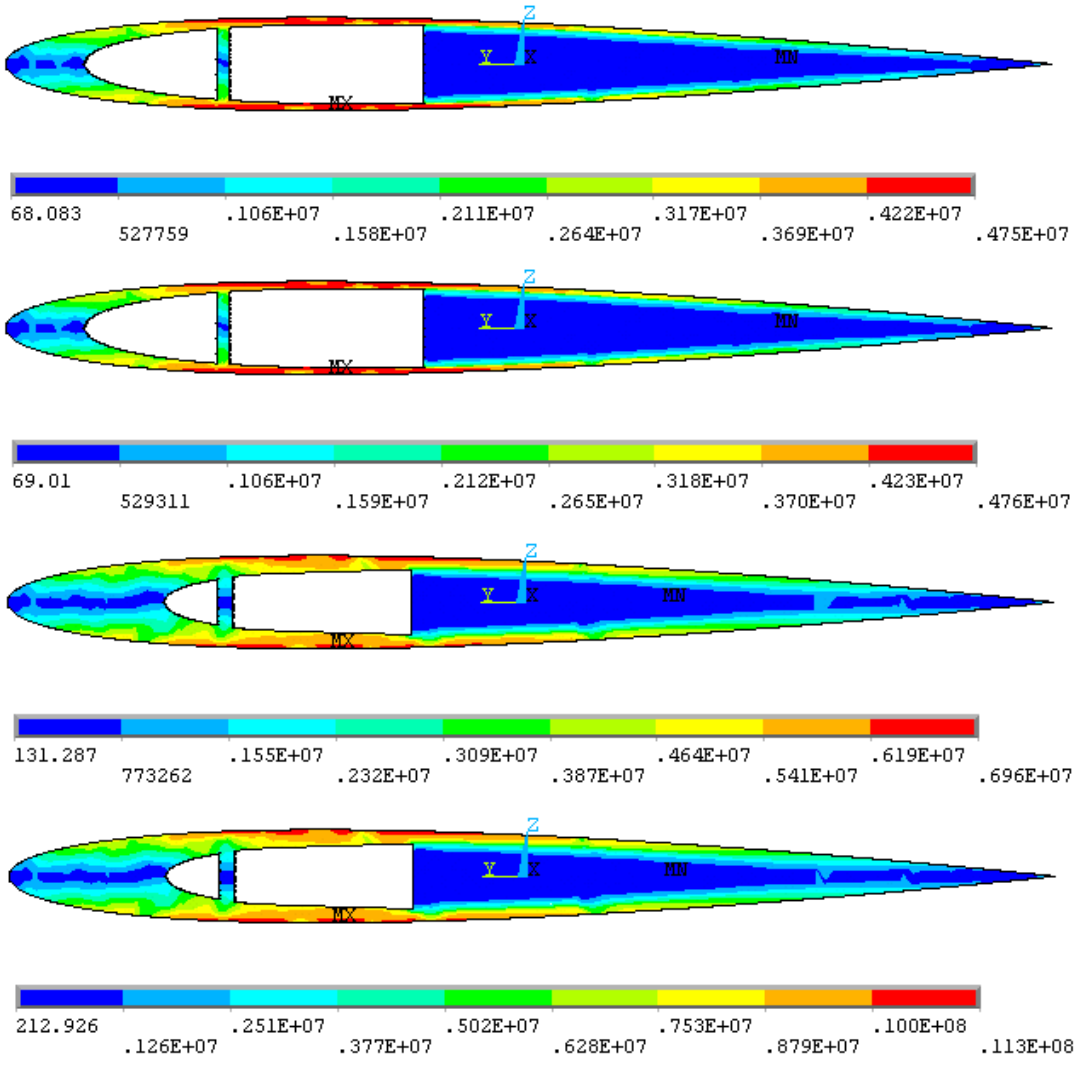

Figure 6.43: Stress distribution for different composite skin designs

6.2.6 Aeroelastic Tailoring

To achieve the more realistic case, the flying aircraft model in Section 4.2.2 is evaluated again by involving the bending-torsion coupling. Figures 6.44 and 6.45 show the numerical results for the aeroelastic phenomena and the aileron effectiveness versus the elastic coupling. Note that, same as before, the aileron effectiveness is defined as how much roll rate can be generated for unit length of aileron.

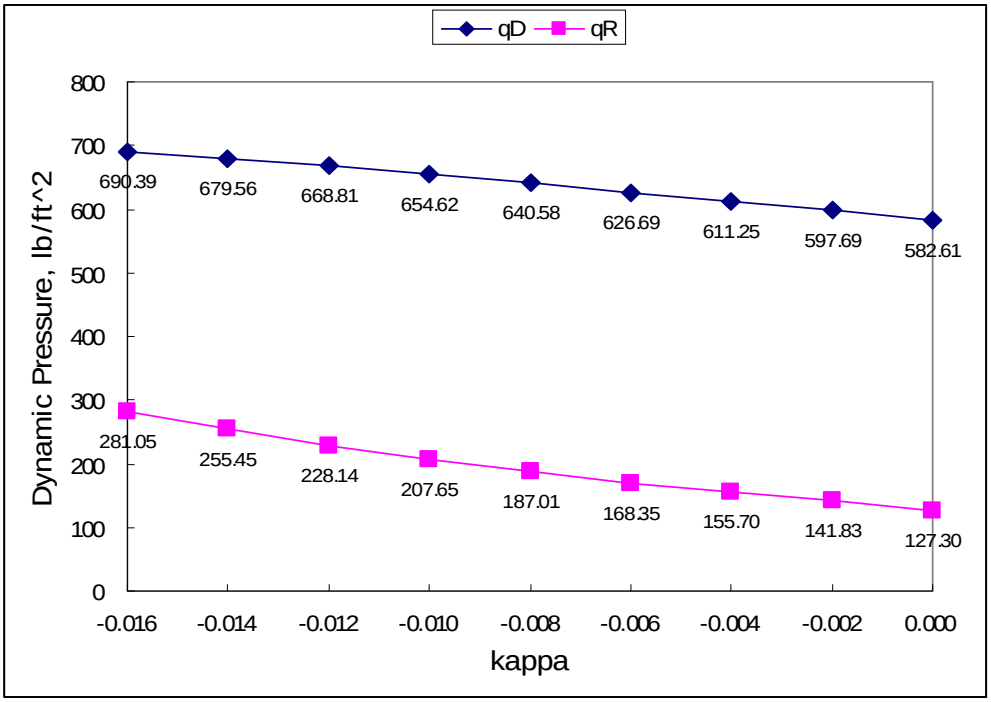

Figure 6.44: The aeroelastic phenomena versus the bending-torsion coupling for rolling aircraft

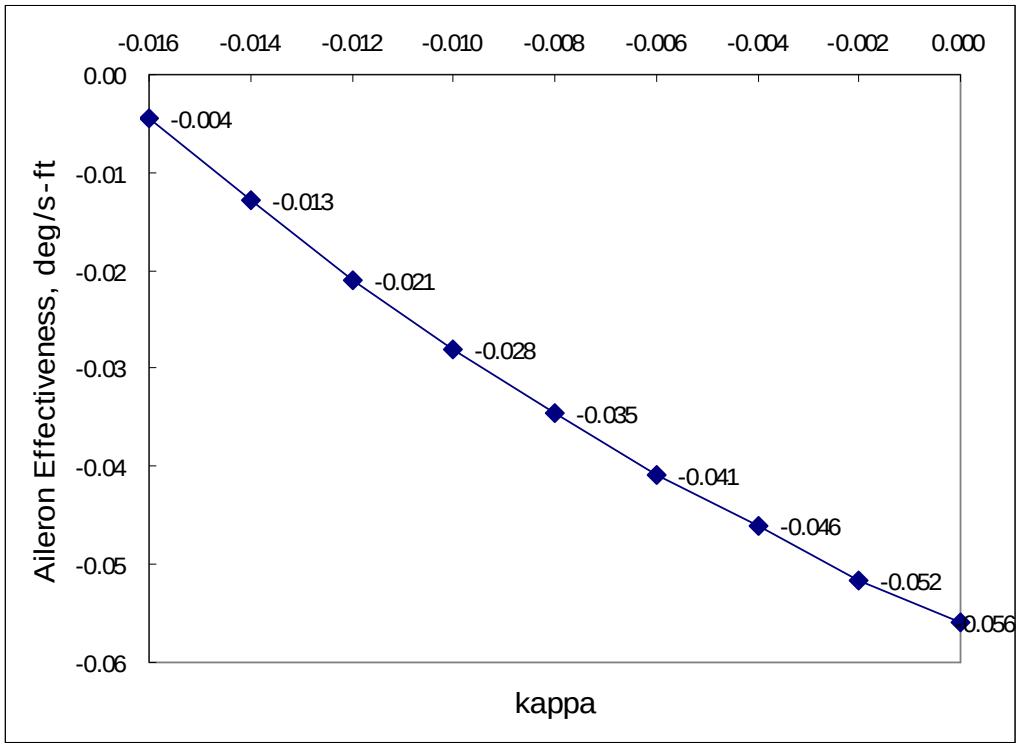

Figure 6.45: The aileron effectiveness versus the bending-torsion coupling for rolling aircraft (at 70% divergence)

Results show that both the divergence and reversal dynamic pressures changed significantly with varying the elastic coupling. Unlike the cantilevered wing case, the post-reversal regime shrank with increasing negative value of κ. To well explain the results, the rolling moment caused by the elastic twist for different negative value of κ is recorded as shown in Figure 6.46. The total rolling moment caused by the elastic twist decreases with increasing the negative value of κ. During the rolling, the bending-torsion coupling did improve the performance on one wing but deteriorate the performance on the other wing instead, since both the wings have the same structural properties. For certain rolling moment caused by the aileron deflection, the lower negative rolling moment caused by the elastic twist results in the higher negative moment caused by the roll rate required for the rolling, and tends to delay the occurrence of the aileron reversal.

Although delaying the occurrence of the aileron reversal is good for the conventional aircraft design, it is not the purpose for this dissertation. Indeed, the higher reversal dynamic pressure shrank the post-reversal regime, and tends to decrease the magnitude of aileron effectiveness after reversal.

The results here provide insight into aeroelastic tailoring wings. Although aeroelastic tailoring can improve the aeroelastic instability significantly, its benefit to delay the reversal may disobey the objective of AAW technology. The designers should be careful to involve the aeroelastic tailoring into the wings design, since both wings of an aircraft have the same structural design, and the antisymmetric design for an aircraft is not realistic and allowable for the conventional aircraft design.

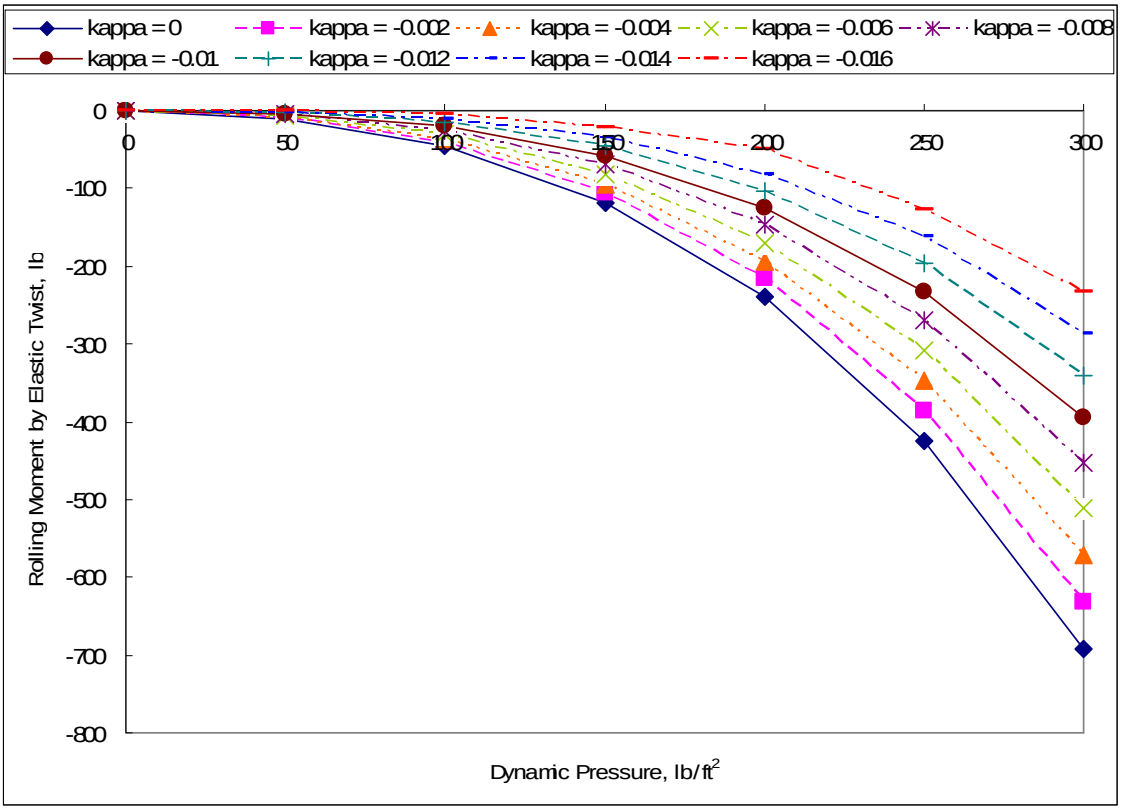

Figure 6.46: The rolling moment caused by the elastic twist for various values of bending-torsion coupling

6.2.7 Airfoil Selection

Similarly, to evaluate the effects of airfoil shape to the aeroelastic problems [19, 68, 96], the same airfoils as Section 6.1.7 are chosen as the wing section in the 10-foot rolling aircraft model. To ensure the consistency between the aerodynamic and structural models, aerodynamic data from XFOIL and structural properties from VABS are put into DYMORE together to build up the aeroelastic model. The aerodynamic data is generated based on single airfoil with 3 degrees of aileron deflection, where the hinge location is at 80% chord. The structural properties are generated based on the associated airfoils with solid wing section.

Results shown in Table 6.13 consist of aerodynamic characteristics and the investigations of aeroelastic phenomena for the different airfoils. Note that the aileron effectiveness here is defined as how much roll rate can be generated with 3 degrees of antisymmetric aileron deflection normalized by the span of aileron. The aileron effectiveness with respect to two kinds of bases is discussed, that are at certain dynamic pressure and at 90% divergence of each airfoil, respectively. For the purpose of this dissertation, the lower reversal dynamic pressure and the higher divergence dynamic pressure are to be explored, which means the wider post-reversal regime and higher roll rate can be utilized. First, comparing NACA 0009 and NACA 0012, the latter has high lift-curve slope and smaller magnitude of C_{M_β}, so it has wider post-reversal regime, which implies that it fits well with the objective. Second, NACA 2415 and NACA 63215 airfoils are not suitable choices for the purpose of this study. Although both of them have higher divergence dynamic pressure, their reversal dynamic pressures are higher as well. While operating the aircraft at 730 lb/ft^2 of dynamic pressure, the aircraft with these two

airfoils has not encountered the roll reversal, which means the associated roll rates still make the aircraft roll positively and that contradicts the purpose of this research. On the other hand, operating the aircraft at 90% divergence, the aircraft with these two airfoils cannot get enough roll rate, even for the case with NACA 2415 airfoil, the magnitude of roll rate is less than that before reversal. Third, comparing between two airfoils used for F/A-18, NACA 65A005 and NACA 65A003.5, they have similar post-reversal regime, but the former one has higher divergence and reversal dynamic pressures. Fourth, RAE 2822 airfoil has the smallest magnitude of C_{M_β} within all the airfoils here, and the aircraft with RAE 2822 airfoil can get highest roll rate (though negative) at 730 lb/ft^2 of dynamic pressure. Lastly, at 90% divergence, NACA 0012, RAE 2822, S 813, and NACA 65A003.5 airfoils are better choices for the present study, since they can generate higher aileron effectiveness. Note that the comparison with respect to 90% divergence is a better option to investigate the post-reversal behavior, since a couple of airfoils have not encountered reversal at 730 lb/ft^2 of dynamic pressure. Although to investigate the post-reversal behavior for the two airfoils, the desired operating dynamic pressure can be increased, some of the airfoils may encounter aeroelastic instability instead.

Table 6.13: Comparisons between airfoil selections for rolling aircraft

Airfoil			**NACA 0009**	**NACA 0012**	**NACA 2415**	**NACA 6409**	**NACA 63215**	**Eppler 387**
Linear Regime		C_{L_α}	6.23	6.44	6.37	6.26	6.36	6.44
		C_{M_β}	-0.68	-0.63	-0.61	-0.57	-0.61	-0.60
Reversal Dynamic Pressure (lb/ft^2)			590.96	725.24	922.86	670.60	785.89	686.77
Divergence Dynamic Pressure (lb/ft^2)			836.96	1032.79	1278.61	933.36	1077.60	937.58
Dynamic Pressure 730 lb/ft^2	**Trim Angle of Attack (deg)**		4.007	4.548	4.964	4.254	4.603	4.304
	Aileron Effectiveness (deg/s-ft)		-0.194	-0.007	0.103	-0.066	0.042	-0.047
90% Divergence	**Trim Angle of Attack (deg)**		4.314	4.085	3.902	4.138	4.007	4.173
	Aileron Effectiveness (deg/s-ft)		-0.103	-0.115	-0.091	-0.095	-0.086	-0.080
Airfoil			**RAE 2822**	**S 813**	**SC 1094r8**	**SC 1095**	**NACA 65A005**	**NACA 65A003.5**
Linear Regime		C_{L_α}	6.09	5.43	6.57	6.54	6.55	6.41
		C_{M_β}	-0.53	-0.63	-0.67	-0.66	-0.63	-0.63
Reversal Dynamic Pressure (lb/ft^2)			490.06	500.81	607.85	679.56	587.61	562.81
Divergence Dynamic Pressure (lb/ft^2)			738.30	995.46	832.98	927.05	821.08	809.26
Dynamic Pressure 730 lb/ft^2	**Trim Angle of Attack (deg)**		3.719	4.312	4.074	4.302	4.046	3.987
	Aileron Effectiveness (deg/s-ft)		-0.510	-0.217	-0.179	-0.054	-0.216	-0.260
90% Divergence	**Trim Angle of Attack (deg)**		4.620	3.962	5.036	4.211	4.436	4.440
	Aileron Effectiveness (deg/s-ft)		-0.141	-0.325	-0.082	-0.077	-0.096	-0.115

6.3 Chapter Summary

To enhance the roll maneuverability by using post-reversal design, some parameters associated with aeroelastic problems are investigated in this chapter. The parameter choices are based on the capability of tools used in the research reported in this dissertation. The wing section inner structures, composite skin, and aeroelastic tailoring are more related to the structural design, whereas all the other parameters investigated herein are involved with both aerodynamic and structural models. These include aspect ratio, hinge locations, airfoil dimension, and airfoil selection, respectively. Chapter 6 provided some guidance to improve the roll maneuverability by post-reversal design. For further analyses, more advanced aerodynamic models and more realistic and complex aeroelastic models should be involved.

CHAPTER VII

CONCLUSIONS AND FUTURE WORK

The concept of getting higher lift from a reversed control surface is not new. Unfortunately, there is no published work addressing this issue with aerodynamic and structural nonlinearities. In the present research, both aerodynamic and structural nonlinearities are involved in two different models, lifting surface and rolling aircraft. This chapter summarizes the conclusions of the work and suggests possible areas of additional research.

7.1 Conclusions

Unlike most published work, such as Active Aeroelastic Wing (AAW) program, to discuss this problem, the present research proposes to investigate post-reversal behavior of high-aspect-ratio wings with geometrically-exact structural nonlinearities and an appropriate level of aerodynamic nonlinearities. In these approaches, a high-aspect-ratio cantilevered wing-aileron system modeled with geometrically-exact composite beam theory [46] and a static stall model for the aerodynamics is first established to demonstrate that there are configurations that reverse at a relatively low dynamic pressure and fly with enhanced (though backward) controls at a higher level of effectiveness than can be achieved in with the conventional sign of controls. Moreover, and more important, a model for a flying aircraft in a rolling maneuver is used to further investigate the problem. Both models are involved with aerodynamic and structural nonlinearities to

evaluate the post-reversal behavior. These approaches overcome the main shortcomings in AAW program, namely that the wing stalled before it would actually reverse.

To illustrate the aeroelastic phenomena, Chapter 2 introduce the aileron reversal problem through the model of rigid wings with a flexible support. These idealized configurations do give some insight into the aeroelastic stability and response, but practical analyses must take flexibility of the lifting surface into account.

For the purpose of this research, Chapter 3 introduced the tools used for the nonlinear analyses, which are XFOIL, a panel method code, and DYMORE, a finite element based multibody dynamic code. Using XFOIL and with the auxiliary experimental data, aerodynamic nonlinearities are involved in nonlinear aeroelastic model built in DYMORE. This is the main approach used herein to implement the idea of improving roll maneuverability by using post-reversal design.

In Chapter 4, two aeroelastic models are investigated, namely a uniform cantilevered lifting surface with aileron and a rolling aircraft with ailerons. Both aerodynamic and structural nonlinearities are considered in the models to more accurately evaluate the post-reversal regime. In addition, the maneuverability for a flying aircraft is discussed in this chapter, along with effects of aileron deflection, Mach number, Reynolds number, as well as the altitude. Both divergence and reversal boundaries are established. The objective for Chapter 5 is to ensure the practicality of the previous results. Results based on XFOIL, advanced CFD codes, and experimental data for some special cases are obtained and validated therein.

Lastly and most importantly, Chapter 6 investigates some parameters associated with the aeroelastic problems to enhance the roll maneuverability within the post-reversal regime. The parameter choices are based on the capability of tools in this dissertation.

Except for the wing section inner structures, composite skin, and aeroelastic tailoring are more related to the structures, all the other parameters evaluated are involved with both aerodynamic and structural models. These include aspect ratio, hinge locations, airfoil dimension, and airfoil selection. Finally some guidance is provided to improve the roll maneuverability by post-reversal design for the future research.

After a series of systematic approaches, conclusions are made as the following:

1 A higher lever of aileron effectiveness can be achieved in the post-reversal regime.

2 Large aileron deflection influences aeroelastic boundaries a lot due to camber's change with varying aileron deflection. Higher aileron deflection results in dramatic shrinkage of the post-reversal regime.

3 For the high-aspect-ratio wings tested herein, lower aspect ratio can widen the post-reversal regime, and tends to generate higher lever of aileron effectiveness to be utilized.

4 Horizontal hinge location affects aeroelastic phenomena a lot, but vertical hinge location does not, especially for thin airfoils. The optimal hinge location depends on the airfoil. For cantilevered wing case, it is located at 80% chord for NACA 0009 based on the resulting rolling moment normalized by the span of aileron. Instead, for rolling aircraft case, it is located at 70% chord for NACA 0009 based on the resulting roll rate normalized by the span of aileron.

5 Airfoil dimension influences aeroelastic phenomena structurally, not aerodynamically. The major factors are the changes of aspect ratio and torsional stiffness due to the enlargement of the chord but keeping the same length of wingspan.

6 The purpose of reducing weight can be achieved by wing section inner design, but composite skin design must be undertaken to ensure the stiffness is sufficiently large to improve control surface effectiveness.

7 Involving bending-torsion coupling can significantly improve aileron effectiveness for the cantilevered wing model due to the divergence dynamic pressure gets higher, even to infinity.

8 Each airfoil is designed for different purpose based on aerodynamic point of view. For the present study, the airfoil with smaller lift-curve slope and smaller magnitude of C_{M_β} is a good option to enhance roll maneuverability within the post-reversal regime, since smaller lift-curve slope makes divergence higher and smaller magnitude of C_{M_β} makes higher level of aileron effectiveness after reversal.

7.2 Contributions

The main contributions of the present work toward enhancing roll maneuverability by using post-reversal design with sufficient accuracy are the following:

1 Provide insight into aeroelastic problems by introducing the aileron reversal for a typical section with linear aerodynamic and structural analysis.

2 Illustrate that XFOIL and DYMORE are reliable tools to involve both aerodynamic and structural nonlinearities into the aeroelastic problem.

3 Develop the computing scheme for the airfoil with leading-edge flap based on Peters' finite-state induced flow model.

4 Demonstrate configurations that reverse at relatively low dynamic pressures and fly with enhanced controls at a higher level of effectiveness than can be achieved with the conventional sign of controls. The results may have important implications for development of highly maneuverable aircraft.

5 Establish the divergence and reversal boundaries associated with aileron deflection, Mach number, Reynolds number, as well as altitude based on a simple aeroelastic model. The results provide the ideas to improve the maneuverability of a flying aircraft.

6 Verify the practicality of the results from XFOIL, in three different approaches which are executed to compare with CFD codes and experimental data. These approaches consist of comparisons for lift coefficient, lift-curve slope, and aerodynamic characteristics for the wing-aileron system with different aileron deflection. Results show XFOIL is a good option to quickly generate the accurate data in the initial analyses and provide a warning of inaccuracy for larger aileron deflections.

7 Evaluate the effects of some aerodynamic and structural parameters to the aeroelastic problems. The results provide suggestions for follow-on research related to the AAW flight program. The parametric designs include the wing aspect ratio, aileron hinge locations, airfoil dimension, wing section inner structures, composite skin, aeroelastic tailoring, and airfoil selection.

7.3 Recommendations for Future Work

Although much has been investigated based on the nonlinear approach utilized for this work, there are still some additional points that need to be studied. In addition, the aeroelastic models need to be improved by involving more advanced aerodynamic models and more complex structural models. The present work can be considered as the very beginning step of a general construction of aeroelastic models to address the post-reversal behavior of a rolling aircraft. However, because the concept is still under demonstration, some independent work is needed to verify the idea. To complete the present research, which tends to lead more research about this area, a number of future tasks can be performed:

1 To validate the results presented here with more advanced CFD codes instead of XFOIL, although XFOIL can quickly generate the required aerodynamic data. XFOIL is no longer reliable for the models with high aileron deflection due to flow separation, since the code is based on a linear panel method.

2 The urgent work to extend the results for the maneuverability here is to investigate how large aileron deflection can be performed at some specific conditions with more advanced aerodynamic models. Related work consists of increasing the predictive capability and the realism of both aerodynamic and structural models.

3 The trim analysis in this dissertation is not realistic, because not all force and moment equations of equilibrium for the flying aircraft are considered. Although the analysis is sufficient for searching the steady roll rate about the short-term roll, the system may be unstable. To search for the trimmed configuration more precisely, the complete set of equations of equilibrium must be considered.

4 The one significant parametric design is aeroelastic tailoring, which is known as the important factor to improve the aeroelastic instability. The influence of bending-torsion coupling is investigated in Sections 6.1.6 and 6.2.6, but the approach is to involve the elastic coupling by varying the bending-torsion stiffness artificially. To evaluate the real cases, the suitable materials and layup designs should be considered to influence the aeroelastic tailoring in the wing design [115], and turns to check how the elastic coupling affects the aeroelastic phenomena. Note that sweeping a wing is another way to involve bending-torsion coupling. Indeed, all the approaches in this dissertation should be applied to the swept wing model [118] immediately, since most of modern aircrafts have swept wings.

5 To investigate the aircraft with low-aspect-ratio wings requires adding chordwise flexibility of the wings, and turns to require the aerodynamics account for the camber changes. In addition, to simulate the more realistic wings for fighter aircrafts, beam models may not be suitable to describe the structural characteristics, and plate and shell models should be taken into account. Again, the improvement of the aeroelastic models is undoubtedly the most urgent work.

6 Most of the approaches to the aeroelastic phenomena here focus on the static analyses. Although the trim of aircraft belongs to the dynamic analyses in DYMORE, searching for the steady roll rate is the objective in this dissertation. It is obviously a good idea to also investigate the dynamic behavior of the rolling aircraft during the post-reversal regime, such as the roll acceleration. Indeed, the results for dynamic behavior may have important implications for development of highly maneuverable fighter aircraft.

7 The work can also be extended to the investigation of smart materials and active actuation system for trailing-edge control surface. The required power for the actuation system can be dramatically reduced, since such a higher (negative) lift can be generated through small aileron deflection during the post-reversal regime. This may result in weight and fuel saving, and tends to save the cost.

8 The wing cross-sectional distortion can be taken into account in further study. To reach a level of cross-section deformation sufficiently large to measurably affect aerodynamic coefficients, special efforts must be undertaken to design the wing section for such deformation. An example of such a design is the chiral cellular materials discussed in [106].

9 Since both structural and aerodynamic nonlinearities are involved in this research, the traditional approaches [35, 36] with linear analysis to enhance roll maneuvers of an aircraft could be readdressed in the future. For example, the approaches about stiffening the wing structures without the weight penalty by structural designers.

APPENDIX

Appendix A. XFOIL 6.9

A.1 General Description

XFOIL 1.0 is written by Mark Drela in 1986. It is an interactive program for the design and analysis of subsonic isolated airfoils. The main goal is to combine the speed and accuracy of high-order panel methods with the new fully-coupled viscous/inviscid interaction method used in the ISES code developed by Drela and Giles. The ISES code uses the steady Euler equations in integral form to represent the inviscid flow, and a compressible lag-dissipation integral method to represent the boundary layers and wakes. The viscous and inviscid flows are fully coupled through the displacement thickness. The design capabilities of ISES code were described in Drela [32] and in Giles and Drela [40].

A.2 Inviscid Formulation

The inviscid formulation of XFOIL is a simple linear-vorticity stream function panel method. A finite trailing edge base thickness is modeled with a source panel. The equations are closed with an explicit Kutta condition. A high-resolution inviscid calculation with the default 160 panels requires seconds to execute on a RISC workstation. Subsequent operating points for the same airfoil but different angles of attack are obtained nearly instantly.

A Karman-Tsien compressibility correction [4] is incorporated, allowing good compressible predictions all the way to sonic conditions. The theoretical foundation of the Karman-Tsien correction breaks down in supersonic flow, and as a result accuracy

rapidly degrades as the transonic regime is entered. Of course, flows with shocks cannot be predicted with any certainty.

A.3 Inverse Formulation

There are two types of inverse methods incorporated in XFOIL, which are Full-Inverse and Mixed-Inverse. The Full-Inverse formulation is essentially Lighthill's and van Ingen's complex mapping method [32], which is also used in the Eppler code and Selig's PROFOIL code. It calculates the entire airfoil geometry from the entire surface velocity distribution. The Mixed-Inverse formulation is simply the inviscid panel formulation (the discrete governing equations are identical) except that instead of the panel vortex strengths being the unknowns, the panel node coordinates are treated as unknowns wherever the surface velocity is prescribed. Allowing the panel geometry to be a variable results in a nonlinear problem, but this is solved in a straightforward manner with a full-Newton method [40].

A.4 Viscous Formulation

The boundary layers and wake are described with a two-equation lagged dissipation integral boundary-layer formulation and an envelope e^n transition criterion [33]. The entire viscous solution (boundary layers and wake) is strongly interacted with the incompressible potential flow via the surface transpiration model. This permits proper calculation of limited separation regions. The drag is determined from the wake momentum thickness far downstream. A special treatment is used for a blunt trailing edge which fairly accurately accounts for base drag.

The total velocity at each point on the airfoil surface and wake, with contributions from the freestream, the airfoil surface vorticity, and the equivalent viscous source distribution, is obtained from the panel solution with the Karman-Tsien correction [4] added. This is incorporated into the viscous equations, yielding a nonlinear elliptic system which is readily solved by a full-Newton method. Execution times are quite rapid. For a sequence of closely spaced angles of attack, the calculation time per point can be substantially smaller.

If lift is specified, then the wake trajectory for a viscous calculation is taken from an inviscid solution at the specified lift. If the angle of attack α is specified, then the wake trajectory is taken from an inviscid solution at that value of α. This is not strictly correct, since viscous effects will in general decrease lift and change the trajectory. This secondary correction is not performed, since a new source influence matrix would have to be calculated each time the wake trajectory is changed. This would result in unreasonably long calculation times. The effect of this approximation on the overall accuracy is small, and will be felt mainly near or past stall, where accuracy tends to degrade anyway. In attached cases, the effect of the incorrect wake trajectory is imperceptible.

Appendix B. DYMORE: A Finite Element Based Tool for the Analysis of Nonlinear Flexible Multibody Systems

Multibody dynamics analysis is originally developed as a tool for modeling mechanisms with simple tree-like topologies composed of rigid bodies, but has considerably evolved to the point where it can handle nonlinear flexible systems with arbitrary topologies. It is now widely used as a fundamental design tool in many areas of mechanical engineering. For example, in the automotive industry multibody dynamics analysis is routinely used for optimizing vehicle ride qualities, a complex multidisciplinary task that involves the simulation of many different sub-components. Modern multibody codes can deal with complex mechanisms of arbitrary topologies including sensors, actuators and controls, are interfaced with CAD solid modeling programs that allow directly importing the problem geometry, and have sophisticated graphics, animation and post-processing features [2, 77, 97]. The success of multibody dynamics analysis tools stems from their flexibility: a given mechanism can be modeled by an idealization process that identifies the mechanism components from within a large library of elements implemented in the code. Each element provides a basic functional building block, for example a rigid or flexible member, a hinge, a motor, etc. Assembling the various elements, it is then possible to construct a mathematical description of the mechanism with the required level of accuracy.

Multibody systems fall into the following categories

1. *Rigid multibody systems* consist of an assemblage of rigid bodies in arbitrary motion with respect to each other. Various efficient formulations have been developed for the modeling of such systems [2, 77].

2. *Linear elastic multibody systems* consist of an assemblage of elastic bodies in arbitrary motion with respect to each other. However, it is assumed that the "elastic displacements and rotations" remain very small at all times. The elastic displacements and rotations of an elastic body are those viewed by an observer confined to a material frame attached to the elastic body. Here again, numerous formulations have been proposed for the dynamic analysis of such systems [101]. More often than not, the elastic behavior of the bodies is represented in an approximate manner by an expansion in terms of representative deformation mode shapes, such as the eigenmodes of the elastic body, for instance.
3. *Nonlinear elastic multibody systems* consist of an assemblage of nonlinear elastic bodies in arbitrary motion with respect to each other. In such systems, the elastic displacements and rotations cannot assume to remain small at all times, i.e. the elastic behavior is inherently nonlinear. In this regime, the representation of elastic deformations through modal expansion becomes questionable [12], and the accuracy of the procedure cannot be guaranteed. The finite element approach appears to provide a solid basis for the dynamic analysis of such systems [22, 23].

DYMORE is a finite element based tool for the analysis of nonlinear elastic multibody systems. Despite its generality and flexibility, multibody dynamics analysis is not yet widely used when dealing with nonlinear elastic systems. Historically, the classical approach to the analysis of these systems has been the modal reduction approach, despite its shortcomings. The equations of motion are derived for the specific configuration of the system at hand, and ordering schemes used to decrease the number of nonlinear terms. If more detailed models of the system are needed to improve accuracy or account for various design complexities, new equations of motion are re-derived. In

fact, various codes have been derived for the analysis of specific machines. For example, rotorcraft manufacturers have developed in-house codes that are geared towards the modeling of the specific configuration of rotorcraft they produce. Different codes are developed for the analysis of windmills or satellites with flexible appendages. This approach severely limits the generality and flexibility of the resulting codes. Developing a new simulation tool for each novel configuration of a specific system is a daunting task, and software validation is an even more difficult issue. Furthermore, the requirement for ever more accurate predictions calls for increasingly detailed and comprehensive models.

Clearly, a more general and flexible paradigm for modeling of nonlinear elastic multibody systems is needed. In particular, the ability to model novel configurations of arbitrary topology through the assembly of basic components chosen from an extensive library of elements is highly desirable. In fact, this approach is at the heart of the finite element method which has enjoyed, for this very reason, an explosive growth in the last few decades. This analysis concept leads to new comprehensive simulation software tools that are modular and expandable. Modularity implies that all the basic building blocks can be validated independently, easing the more challenging task of validating complete simulation procedures. Because they are applicable to configurations with arbitrary topologies, including those not yet foreseen, such simulation tools will enjoy a longer life span, a critical requirement for any complex software tool.

As an example of this approach, Figure A.1 depicts the conceptual representation of a rotorcraft system as a flexible multibody system. The various mechanical components of the system are associated with the elements found in the library of typical multibody analysis tools.

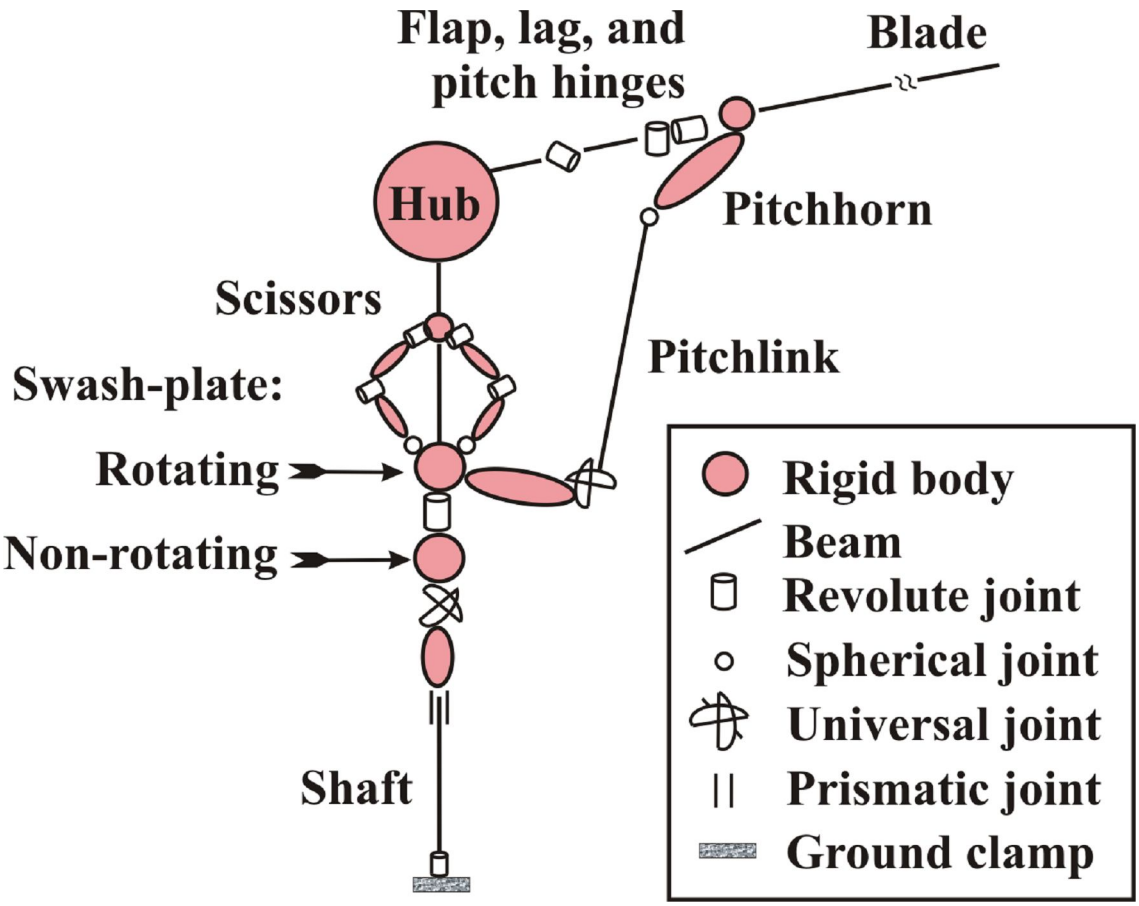

Figure A.1: Detailed multibody representation of a rotor system. At right, a typical articulated blade. At left, a bearingless blade design.

The picture shows a classical configuration for the control chain, consisting of a swash-plate with rotating and non-rotating components. The lower swash-plate motion is controlled by actuators that provide the vertical and angular control inputs. The upper swash-plate is connected to the rotor shaft through a scissors-like mechanism, and controls the blade pitching motions through pitch-links. This familiar control linkage configuration can be modeled using the following elements: rigid bodies, used to model the lower and upper swash-plate components and scissors links, and beams for modeling the flexible shaft and pitch-link. These bodies are connected through standard mechanical

joints: a hinge, called a revolute joint in the terminology of multibody dynamics [2, 77], connects the upper and lower swash-plates, allowing the former to rotate at the shaft angular velocity while the latter is non-rotating. Revolute joints also connect the scissors links to each other and to the upper swash-plate, thereby synchronizing the shaft and upper swash-plate. Other types of joints are required for the model. For example, the lower swash-plate is allowed to tilt with respect to an element that slides along the shaft, but does not rotate about the shaft direction. The universal joint, a sequence of two revolute joints whose mutually orthogonal axes of rotation lie in a common plane, serves this purpose. Similarly, the pitch-link is connected to the pitch-horn by means of a spherical joint that allows the connected components to be at an arbitrary orientation with respect to each other.

Figure A.1 also shows two different rotor configurations: a classical, fully articulated design on the right and a bearingless design on the left. The articulated blade is connected to the hub through three revolute joints, which model the flap, lag and pitch hinges. Possible offsets between these joints could be modeled by means of rigid or flexible bodies. The blade itself is modeled by an appropriate beam element that should account for the inertial and elastic couplings that arise from the use of composite materials [13]. The bearingless design is a multiple load path configuration, involving a flex-beam and a torsion cuff assembled in parallel and connected by a snubber. It is important to note that the two designs, fully articulated or bearingless, can be modeled by assembling different sets of elements from the multibody library of elements. There is no need to derive and validate two different sets of equations for the two configurations. Of course, the level of detail presented in Figure A.1 is not always needed: some of the control chain components could be omitted, and the blade could be represented by rigid bodies rather

than beam elements, if a crude model is desired.

DYMORE implements a finite element based multibody dynamics analysis of nonlinear elastic multibody systems. The proposed approach provides the level of generality and flexibility required to solve complex problems such as those described in the above conceptual examples. The multibody dynamics analysis is cast within the framework of nonlinear finite element methods, and the element library includes rigid and deformable bodies as well as joint elements. Deformable bodies are modeled with the finite element method, in contrast with the classical approach to multibody dynamics, which predominantly relies on rigid bodies or introduces flexibility by means of a modal representation [97, 101]. With today's advances in computer hardware, very inexpensive PC's provide enough computational power to run full finite element models of complex, nonlinear elastic systems. Hence, resorting to modal reduction in order to save CPU time is no longer a valid argument, especially when considering the possible loss of accuracy associated with this reduction [12].

In the proposed approach, the formulations of beams and shells are geometrically exact, i.e. they account for arbitrarily large displacements and finite rotations, but are limited to small strains. The equations of equilibrium are written in a Cartesian inertial frame. Constraints are modeled using the Lagrange multiplier technique. This leads to systems of equations that are highly sparse, although not of minimal size. This approach can treat arbitrarily complex topologies. Furthermore, because it is an extension of the finite element method to multibody systems, the algorithms such as sparse solvers, and data structures developed for FEM analyses are directly applicable to the present approach.

REFERENCES

[1] Abbott, I. H. and Von Doenhoff, A. E., *Theory of Wing Sections*, Dover Publications, Inc., 1959.

[2] Amirouche, F. M. L., *Computational Methods in Multibody Dynamics*, Prentice-Hall, Englewood Cliffs, New Jersey, 1992.

[3] Andersen, G., Forster, E., Kolonay, R., and Eastep, F., "Multiple control surface utilization in active aeroelastic wing technology," *Journal of Aircraft*, Vol. 34, No. 4, 1997, pp. 552-557.

[4] Anderson, Jr., J. D., *Fundamentals of Aerodynamics*, Mcgraw-Hill, Inc., 2nd ed., 1991.

[5] Anderson, Jr., J. D., *Introduction to Flight*, Mcgraw-Hill, Inc., 3rd ed., 1989.

[6] Angeles, Jorge, *Spatial Kinematic Chains: Analysis, Synthesis, Optimization*, Springer-Verlag, 1996.

[7] Appa, K., Ausman, J., and Khot, N. S., "Feasibility assessment and optimization study of smart actuation systems for enhanced aircraft maneuver performance," *WL-TR-97-3083*, Oct., 1997.

[8] Austin, F., Knowles, G. J., Jung, W. G., Tung, E. C., and Sheedy, E. M., "Adaptive/conformed wing design for future aircraft," *Proceedings of the 1st European Conference on Smart Structures and Materials*, Glasgow, Scotland, May, 1992.

[9] Balakrishnan, A. V., “Nonlinear aeroelasticity: the steady-state theory,” *AIAA Journal*, Vol. 46, No. 1, 2008, pp. 177-184.

[10] Bauchau, O. A., “Computational schemes for flexible, nonlinear multi-body systems," *Multibody System Dynamics*, Vol. 2, No. 2, 1998, pp. 169-225.

[11] Bauchau, O. A., Bottasso, C., and Nikishkov, Y., “Modeling rotorcraft dynamics with finite element multibody procedures," *Mathematical and Computer Modeling*, Vol. 33, No. 10-11, 2001, pp. 1113-1137.

[12] Bauchau, O. A. and Guernsey, D., “On the choice of appropriate bases for nonlinear dynamic modal analysis,” *Journal of the American Helicopter Society*, Vol. 38, Issue 4, 1993, pp. 28-36.

[13] Bauchau, O. A. and Hodges, D. H., “Analysis of nonlinear multibody systems with elastic couplings,” *Multibody System Dynamics*, Vol. 3, No. 2, 1999, pp. 163-188.

[14] Beauchamp, C. H., Nadolink, R. H., Dickinson, S. C., and Dean, L. M., “Shape memory alloy adjustable camber (SMAAC) control surfaces,” *Proceedings of the 1st European Conference on Smart Structures and Materials*, Glasgow, Scotland, May, 1992, pp. 189-192.

[15] Ben-Zeev, O. and Chopra, I., “Advances in the development of an intelligent helicopter rotor employing smart trailing-edge flaps," *Smart Materials and Structures*, Vol. 5, No. 1, 1996, pp. 11-25.

[16] Bishop, J. A., Eastep, F. E., Striz, A. G., and Venkayya, V. B., “Influence of model complexity and aeroelastic constraints on multidisciplinary optimization of wings,” *Journal of Aircraft*, Vol. 35, No. 5, Sept.-Oct., 1998, pp. 784-790.

[17] Bisplinghoff, R. L., Ashley, H., and Halfman, R. L., *Aeroelasticity*, Dover Publications, Inc., 1996.

[18] Boehm, B., Flick, P., Sanders, B., Pettit, C., Reichenbach, E., and Zillmer, S., "Static aeroelastic response predictions of the active aeroelastic wing (AAW) flight research vehicle," *Proceedings of 42nd AIAA/ASME/ASCE/AHS/ASC Structures, Structural Dynamics, and Materials Conference and Exhibit*, Seattle, WA, Apr. 16-19, 2001, AIAA-2001-1372.

[19] Bolonkin, A. and Gilyard, G. B., "Estimated benefits of variable-geometry wing camber control for transport aircraft," *NASA/TM-1999-206586*, Oct., 1999.

[20] Borglund, D., "Aeroservoelastic design optimization with experimental verification," *Journal of Aircraft*, Vol. 38, No. 5, 2001, pp. 958-961.

[21] Bousman, W. G., "Aerodynamic characteristics of SC1095 and SC1094 R8 airfoils," *NASA/TP-2003-212265* and *AFDD/TR-04-003*.

[22] Cardona, A. and Géradin, M., "Time integration of the equations of motion in mechanism analysis," *Computers & Structures*, Vol. 33, Issue 3, 1989, pp. 801-820.

[23] Cardona, A., Géradin, M., and Doan, D. B., "Rigid and flexible joint modelling in multibody dynamics using finite elements," *Computer Methods in Applied Mechanics and Engineering*, Vol. 89, Issues 1-3, 1991, pp. 395-418.

[24] Chen, P. C., Jha, R., Sarhaddi, D., Liu, D. D., Griffin, K., and Yurkovich, R., "Variable stiffness spar (VSS) approach for aircraft maneuver enhancement using ASTROS," *Journal of Aircraft*, Vol. 37, No. 5, 2000, pp. 865-871.

[25] Critzos, C. C., Heyson, H. H., and Boswinkle, R. W., "Aerodynamic characteristics of NACA 0012 airfoil section at angles of attack from 0° to 180°," *NACA-TN-1995-3361*, 1955.

[26] Depailler, G. and Friedmann, P. P., "Alleviation of dynamic stall induced vibrations using actively controlled flaps," *Proceedings of the 58th Annual Forum of the AHS, American Helicopter Society*, Alexandria, VA, 2002.

[27] Depailler, G. and Friedmann, P. P., "Alleviation of dynamic stall induced vibrations using actively controlled flaps with freeplay," *Proceedings of the 28th European Rotorcraft Forum*, Bristol, England, U.K., 2002.

[28] Dowell, E. H., Bliss, D. B., and Clark, R. L., "An adaptive aeroelastic wing with leading- and trailing-edge control surfaces," *Journal of Aircraft*, Vol. 40, No. 3, May-June, 2003, pp. 559-565.

[29] Dowell, E. H. and Hall, K. C., "Modeling of fluid-structure interaction," *Annual Review of Fluid Mechanics*, Vol. 33, 2001, pp. 445-490.

[30] Dowell, E. H. and Tang, D., "Nonlinear aeroelasticity and unsteady aerodynamics," *AIAA Journal*, Vol. 40, No. 9, 2002, pp. 1697-1707.

[31] Drela, M., "Transonic low-Reynolds number airfoils," *Journal of Aircraft*, Vol. 29, No. 6, 1992, pp. 1106-1113.

[32] Drela, M., "Two-dimensional transonic aerodynamic design and analysis using the Euler equations," Massachusetts Institute of Technology, Gas Turbine Laboratory Rept. 187, Feb., 1986.

[33] Drela, M. and Giles, M., "Viscous-inviscid analysis of transonic and low Reynolds number airfoils," *AIAA Journal*, Vol. 25, No. 10, 1987, pp. 1347-1355.

[34] Etkin, B. and Reid, L. D., *Dynamics of Flight: Stability and Control*, John Wiley & Sons, Inc., New York, 3rd ed., 1996.

[35] Friedmann, P. P., "Renaissance of aeroelasticity and its future," *Journal of Aircraft*, Vol. 36, No. 1, Jan.-Feb., 1999, pp. 105-121.

[36] Friedmann, P. P., "Rotary-wing aeroelasticity: Current status and future trends," *AIAA Journal*, Vol. 42, No. 10, Oct., 2004, pp. 1953-1972.

[37] Garcia, J. A., "Numerical investigation of nonlinear aeroelastic effects on flexible high-aspect-ratio wings," *Journal of Aircraft*, Vol. 42, No. 4, 2005, pp. 1025-1036.

[38] Garcia, J. A. and Guruswamy, G. P., "Static aeroelastic characteristics of an advanced wing with a control surface using Navier-Stokes equations," *Proceedings of the 37th AIAA Aerospace Sciences Meeting and Exhibit*, Reno, NV, Jan. 11-14, 1999, AIAA-1999-796.

[39] Giles, M. and Drela, M., "Two-dimensional transonic aerodynamic design method," *AIAA Journal*, Vol. 25, No. 9, 1987, pp. 1199-1206.

[40] Giles, M., Drela, M., and Thompson, W. T., "Newton solution of direct and inverse transonic Euler equations," *Proceedings of the 7th Computational Fluid Dynamics Conference*, New York, 1985, AIAA -1985-1530.

[41] Giurgiutiu, V., "Active-materials induced-strain actuation for aeroelastic vibration control," *The Shock and Vibration Digest*, Vol. 32, No. 5, Sept., 2000, pp. 355-368.

[42] Gomes, A. A. and Suleman, A., "Topology optimization of a reinforced wing box for enhanced roll maneuvers," *AIAA Journal*, Vol. 46, No. 3, 2008, pp. 548-556.

[43] Gribbs, R. and Friedmann, P. P. “Actuator saturation and its influence on vibration reduction by actively controlled flaps,” *Proceedings of the 42nd AIAA/ASME/ASCE/AHS/ACS Structures, Structural Dynamics and Materials Conference*, Seattle, WA, April, 2001, AIAA -2001-1467.

[44] Hall, J. W., “Executive summary AFTI/F-111 mission adaptive wing,” *WRDC-TR-89-3083*, Sept., 1989.

[45] Hassan, A. A. and Straub, F. K., “Evaluation of a flapped airfoil configuration for an advanced rotor,” *Proceedings of the 1995 AHS Aeromechanics Specialists Conference*, Stratford, CT, Oct., 1995.

[46] Hodges, D. H., *Nonlinear Composite Beam Theory*, AIAA, Washington, D.C., 2006.

[47] Hodges, D. H. and Pierce, G. A., *An Introduction to Structural Dynamics and Aeroelasticity*, Cambridge Aerospace Series, Cambridge University Press, New York, 2002.

[48] Hodges, D. H., Pierce, G. A., Bauchau, O. A., and Smith, M. J., *AE 6200: Aeroelasticity*, Class Notes, The Daniel Guggenheim School of Aerospace Engineering, Georgia Institute of Technology, 2004.

[49] Jen, Y. and Chang, L., “Evaluating bending fatigue strength of aluminum honeycomb sandwich beams using local parameters,” *International Journal of Fatigue*, Vol. 30, 2008, pp. 1103-1114.

[50] Khot, N. S., Appa, K., Ausman, J., and Eastep, F. E., "Deformation of a flexible wing using an actuating system for a rolling maneuver without ailerons," *Proceedings of the 39th AIAA/ASME/ASCE/AHS/ASC Structures, Structural Dynamics, and Materials Conference and Exhibit, and AIAA/ASME/AHS Adaptive Structures Forum*, Long Beach, CA, April 20-23, 1998, AIAA-1988-1802.

[51] Khot, N. S., Appa, K., and Eastep, F. E., "Actuating system for enhancement of rolling maneuver of a wing with ailerons," *Proceedings of the 40th AIAA/ASME/ASCE/AHS/ASC Structures, Structural Dynamics, and Materials Conference and Exhibit, AIAA/ASME/AHS Adaptive Structures Forum and AIAA Forum on Non-Deterministic Approaches*, St. Louis, MO, 1999, AIAA-1999-1397.

[52] Khot, N. S., Eastep, F. E., and Kolonay, R. M., "A method for enhancement of the rolling maneuver of a flexible wing," *Proceedings of the 37th AIAA/ASME/ASCE/AHS/ASC/Adaptive Structures, Structural Dynamics, and Materials Conference*, Salt Lake City, UT, 1996, AIAA-1996-1391.

[53] Khot, N. S., Eastep, F. E., and Kolonay, R. M., "Optimization of a composite wing structure for enhancement of the rolling maneuver," *Proceedings of the 6th AIAA/NASA/ISSMO/Symposium on Multidisciplinary Analysis and Optimization*, Bellevue, WA, 1996, AIAA-1996-3998.

[54] Khot, N. S., Eastep, F. E., and Kolonay, R. M., "Optimization of a flexible wing without ailerons for the rolling maneuver," *Journal of Aircraft*, Vol. 37, No. 5, 2000, pp. 892-897.

[55] Khot, N. S., Eastep, F. E., and Kolonay, R. M., “Wing twist and camber for the rolling maneuver of a flexible wing without aileron,” *Proceedings of the 38th AIAA/ASME/ASCE/AHS/Adaptive Structures Forum*, Kissimmee, FL, 1997, AIAA-1997-1268.

[56] Khot, N. S., Kolonay, R. M., and Eastep, F. E., “Composite wing optimization for enhancement of the rolling maneuver in subsonic flow,” *Structural and multidisciplinary optimization*, Vol. 17, 1999, pp. 95-103.

[57] Kim, C., *Static and Dynamic Aeroelastic Simulation of Wings with State Space Aerodynamic Models*. Master Thesis, Georgia Institute of Technology, April, 2000.

[58] Kim, D., Park, Y., Lee, I., and Kwon, O. J., “Nonlinear aeroelastic computations of a wing/pylon/finned-store using parallel computing,” *AIAA Journal*, Vol. 43, No. 1, 2005, pp. 53-62.

[59] Koratkar, N. A. and Chopra, I., “Analysis and testing of Mach-scaled rotor with trailing-edge flaps,” *AIAA Journal*, Vol. 38, No. 7, 2000, pp. 1113-1124.

[60] Koratkar, N. A. and Chopra, I., “Testing and validation of a Froude-scaled helicopter rotor model with piezo-bimorph actuated trailing edge flaps," *Smart Structures and Integrated Systems, SPIE*, June, 1997, pp. 183-205.

[61] Kudva, J. N., “Overview of the DARPA smart wing project,” *Journal of Intelligent Material Systems and Structures*, Vol. 15, 2004, pp. 261-267.

[62] Lazarus, K. B., Crawley, E. F., and Bohlmann, J. D., “Static aeroelastic control using strain actuated adaptive structures,” *Journal of Intelligent Material Systems and Structures*, Vol. 2, No. 3, 1991, pp. 386-410.

[63] Lee, T. and Chopra, I., "Design of piezostack-driven trailing-edge flap actuator for helicopter rotors," *Smart Materials and Structures*, Vol. 10, 2001, pp. 15-24.

[64] Leishman, J. G., *Principles of Helicopter Aerodynamics*, Cambridge University Press, Cambridge, UK, 2000.

[65] Lemnios, A. Z. and Jones, R., "The servo flap – an advanced rotor control system," *Proceedings of AHS and NASA Ames Research Center Vertical Lift Aircraft Design Conference, American Helicopter Society*, Alexandria, VA, 1990, pp. 1-41.

[66] Lyon, C. A., Broeren, A. P., Giguere, P., and Selig, M. S., *Summary of Low-Speed Airfoil – Volume 3*, SoarTech Aero Publications, Virginia Beach, VA , March, 1998.

[67] Makeev, A., *Geometrically Nonlinear Analysis of Laminated Composites with Extension-Twist Coupling*. Ph.D. Thesis, Georgia Institute of Technology, Nov., 1997.

[68] Maute, K. and Reich, G. W., "An aeroelastic topology optimization approach for adaptive wing design," *Proceedings of the 45th AIAA/ASME/ASCE/AHS/ASC Structures, Structural Dynamics & Materials Conference*, Palm Springs, California, April, 2004, AIAA-2004-1805.

[69] Maute, K., Nikbay, M., and Farhat, C., "Conceptual Layout of aeroelastic wing structures by topology optimization," *Proceedings of the 43rd AIAA/ASME/ASCE/AHS/ASC Structures, Structural Dynamics, and Materials Conference*, Denver, Colorado, April 22-25, 2002, AIAA-2002-1480.

[70] Mavris, D. N., Flick, P. M., and Love, M. H. “Development of wing structural weight equation for active aeroelastic wing technology,” *SAE/AIAA World Aviation Congress and Exposition*, San Francisco, CA, October 19-21, 1999, SAE-1999-01-5640.

[71] McCroskey, W. J., “A critical assessment of wind tunnel results for the NACA 0012 airfoil,” *Proceedings of AGARD Fluid Dynamics Panel Symposium on “Aerodynamic Data Accuracy and Quality; Requirements and Capabilities in Wind Tunnel Testing,”* Naples, Italy, Sept.-Oct., 1987.

[72] Mendenhall, M. R. and Perkins Jr., S. C., “Predicted high-alpha aerodynamic characteristics of maneuvering aircraft,” *Proceedings of the 14th AIAA Applied Aerodynamics Conference*, New Orleans, LA, June 17-20, 1996, AIAA-1996-2433.

[73] Miller, G. D., “Active flexible wing (AFW) technology,” *AFWAL-TR-87-3036*, Feb., 1988.

[74] Miller, G. D., “An active flexible wing multi-disciplinary design optimization method,” *Proceedings of 5th AIAA Symposium on Multidisciplinary Analysis and Optimization*, Panama City, Florida, Sept., 1994, AIAA-1994-4412.

[75] Mittal, S. and Saxena, P., “Prediction of hysteresis associated with the static stall of an airfoil,” *AIAA Journal*, Vol.38, No.5, 2000, pp. 933-935.

[76] Munteanu, S., Rajadas, J., Nam, C., and Chattopadhyay, A., “Reduced-order-model approach for aeroelastic analysis involving aerodynamic and structural nonlinearities,” *AIAA Journal*, Vol. 43, No. 3, 2005, pp. 560-571.

[77] Nikravesh, P. E., *Computer-Aided Analysis of Mechanical Systems*, Prentice-Hall, Englewood Cliffs, New Jersey, 1988.

[78] Österheld, C. M., Heinze, W., and Horst, P., "Influence of aeroelastic effects on preliminary aircraft design," *ICAS Congress*, International Council of the Aeronautical Sciences, 2000, pp. 146.1-146.10.

[79] Ozbay, S., Extension-Twist Coupling Optimization in Composite Rotor Blades. Ph.D. Thesis, Georgia Institute of Technology, May, 2006.

[80] Palacios, R. and Cesnik, C. E. S., "Geometrically nonlinear theory of composite beams with deformable cross sections," *AIAA Journal*, Vol. 46, No. 2, 2008, pp. 439-450.

[81] Patil, M. J. and Hodges, D. H., "On the importance of aerodynamic and structural geometrical nonlinearities in aeroelastic behavior of high-aspect-ratio wings," *Journal of Fluids and Structures*, Vol. 19, No. 7, 2004, pp. 905-915.

[82] Patil, M. J., Hodges, D. H., and Cesnik, C. E. S., "Limit cycle oscillations in high-aspect-ratio wings," *Journal of Fluids and Structures*, Vol. 15, No. 1, 2001, pp. 107-132.

[83] Patil, M. J., Hodges, D. H., and Cesnik, C. E. S., "Nonlinear aeroelastic analysis of complete aircraft in subsonic flow," *Journal of Aircraft*, Vol. 37, No. 5, 2000, pp. 753-760.

[84] Patil, M. J., Hodges, D. H., and Cesnik, C. E. S., "Nonlinear aeroelasticity and flight dynamics of high-altitude long-endurance aircraft," *Journal of Aircraft*, Vol. 38, No. 1, 2001, pp. 88-94.

[85] Pendleton, E., Bessette, D., Field, P., Miller, G., and Griffin, K., "The active aeroelastic wing flight research program: Technical program and model analytical development," *Journal of Aircraft*, Vol. 37, No. 4, 2000, pp. 554-561.

[86] Pendleton, E., Griffin, K., Kehoe, M., and Perry, B., "A flight research program for active aeroelastic wing technology," *Proceedings of the 37th AIAA/ASME/ASCE/AHS/ASC Structures, Structural Dynamics and Materials Conference and Exhibit*, AIAA, Salt Lake City, UT, April 15-17, 1996, AIAA-1996-1574.

[87] Perry, Boyd, III, Cole, Stanley R., Miller, and Gerald D., "Summary of an active flexible wing program," *Journal of Aircraft*, Vol. 32, No. 1, 1995, pp. 10-15.

[88] Perkins Jr., S. C. and Mendenhall, M. R., "Prediction of post-stall aerodynamic characteristics of maneuvering aircraft," *Proceedings of the 17th Applied Aerodynamics Conference*, Norfolk, VA, June 28-July 1, 1999.

[89] Peters, D. A., "Two-dimensional incompressible unsteady airfoil theory – An overview," *Journal of Fluids and Structures*, Vol. 24, 2008, pp. 295-312.

[90] Peters, D. A. and Barwey, D., "A general theory of rotorcraft trim," AIAA-1995-1451.

[91] Peters, D. A. and He, C. J., "Finite State Induced Flow Models. Part II: Three-Dimensional Rotor Disk," *Journal of Aircraft*, Vol. 32, No. 2, March-April, 1995, pp. 323-333.

[92] Peters, D. A., Barwey, D., and Su, A., "An integrated airloads-inflow model for use in rotor aeroelasticity and control analysis," *Mathematical and Computer Modeling*, Vol. 19, No. 3/4, 1994, pp. 109-123.

[93] Peters, D. A., Hsieh, M. A., and Torrero, A., "A state-space airloads theory for flexible airfoils," *Journal of American Helicopter Society*, Vol. 51, No. 4, October, 2007, pp. 329-342.

[94] Peters, D. A., Karunamoorthy, S., and Cao, W., "Finite State Induced Flow Models. Part I: Two-Dimensional Thin Airfoil," *Journal of Aircraft*, Vol. 32, No. 2, March, 1995, pp. 313-322.

[95] Polhamus, E. C., "A survey of Reynolds number and wing geometry effects on lift characteristics in the low speed stall region," *NASA Contractor Report 4745*, June, 1996.

[96] Prock, B. C., Weisshaar, T. A., and Crossley, W. A., "Morphing airfoil shape change optimization with minimum actuator energy as an objective," *Proceedings of the 9th AIAA/ISSMO Symposium on Multidisciplinary Analysis and Optimization*, Atlanta, Georgia, Sept., 2002, AIAA-2002-5401.

[97] Schiehlen, W. O., Multibody system dynamics: Roots and perspectives. *Multibody System Dynamics*, Vol. 1, No. 2, 1997, pp. 149-188.

[98] Schroeder, E. J. and Baeder, J. D., "Using computational fluid dynamics for micro-air vehicle airfoil validation and prediction," *Proceedings of the 23rd AIAA Applied Aerodynamics Conference*, Toronto, Ontario, Canada, June, 2005, AIAA-2005-4841.

[99] Selig, M. S., Guglielmo, J. J., Broeren, A. P., and Giguere, P., *Summary of Low-Speed Airfoil – Volume 2*, SoarTech Aero Publications, Virginia Beach, VA, May, 1996.

[100] Selig, M. S. and McGranahan, B. D., "Wind tunnel aerodynamic tests of six airfoils for use on small wind turbines," *NREL/SR-500-34515*, Oct., 2004.

[101] Shabana, A. A., Flexible multibody dynamics: Review of past and recent developments. *Multibody System Dynamics*, Vol. 1, No. 2, 1997, pp. 189-222.

[102] Sitaraman, J., Baeder, J. D., and Chopra, I., "Validation of UH-60A rotor blade aerodynamic characteristics using CFD," *Proceedings of the 59th Annual Forum of American Helicopter Society*, Phoenix, AZ, May, 2003.

[103] Smith, J. W., Lock, W. P., and Payne, G. A., "Variable-camber systems integration and operational performance of the AFTI/F-111 mission adaptive wing," *NASA Technical Memorandum 4370*, April, 1992.

[104] Smith, M. J., Patil, M. J., and Hodges, D. H., "CFD-based analysis of nonlinear aeroelastic behavior of high-aspect ratio wings," *Proceedings of the 42nd Structures, Structural Dynamics and Materials Conference*, Seattle, Washington, April 16-19, 2001, AIAA-2001-1582.

[105] Smith, M. J., Potsdam, M., Wong, T., Baeder, J., and Phanse, S., "Evaluation of CFD to determine two-dimensional airfoil characteristics for rotorcraft applications," *Proceedings of the 60th Annual Forum of American Helicopter Society*, Baltimore, MD, June, 2004, *Journal of the American Helicopter Society*, Vol. 51, Issue 1, Jan., 2006, pp. 70-79.

[106] Spadoni, Alessandro, *Application of chiral cellular materials for the design of innovative components*. Ph.D. Thesis, Georgia Institute of Technology, Dec., 2008.

[107] Straub, F. K. and Charles, B. D., "Comprehensive Modeling of Rotors with Trailing Edge Flaps," *Proceedings of 55th Annual AHS Forum*, Montreal, May, 1999.

[108] Straub, F. K., Kennedy, D. K., Domzalski, D. B., Hassan, A. A., Ngo, H., Anand, V., and Birchette, T., "Smart material-actuated rotor technology–SMART," *Journal of Intelligent Material Systems and Structures*, Vol. 15, No. 4, 2004, pp. 249-260.

[109] Straub, F. K., Kennedy, D. K., Stemple, A. D., H., Anand, V., and Birchette, T., "Development and whirl tower test of the SMART active flap rotor," *Proceedings of SPIE: Smart Structures and Materials 2004*, Vol. 5388, July, 2004, pp. 202-212.

[110] Tang, D. M., Li, A., and Dowell, E. H., "Experimental and theoretical study on rolling effectiveness of multiple control surfaces," *AIAA Journal*, Vol. 41, No. 1, 2003, pp. 160-167.

[111] Tang, D. M., Li, A., and Dowell, E. H., "Transient response study of rolling effectiveness of multiple control surfaces," *Journal of Fluid and Structures*, Vol. 19, No. 5, June, 2004, pp. 621-634.

[112] Voracek, D., Pendleton, E., Reichenbach, E., Griffin, K., and Welch, L., "The active aeroelastic wing phase I flight research through January 2003," *NASA/TM-2003-210741*, April, 2003.

[113] Walz, C. and Chopra, I., "Design and testing of a helicopter rotor model with smart trailing edge flaps," *Proceedings of the 35th Structures, Structural Dynamics and Materials Conference, Adaptive Structures Forum*, 1994, AIAA-1994-1767.

[114] Wei, F. S. and Jones, R., "Correlation and analysis for SH-2F 101 rotor," *Journal of Aircraft*, Vol. 25, No. 7, 1988, pp. 647-652.

[115] Weisshaar, T. A., Duke, D. K., and Dobbins, A., "Active aeroelastic tailoring with adaptive continuous control surfaces," *Proceedings of the 41st AIAA/ASME/ASCE/AHS/ASC Structures, Structural Dynamics, and Materials Conference and Exhibit*, Atlanta, GA, April 3-6, 2000, AIAA-2000-1619.

[116] Woods-Vedeler, J. A., Pototzky, A. S., and Hoadley, S. T., "Active load control during rolling maneuver," *NASA Technical Paper 3455*, Oct., 1994.

[117] Woods-Vedeler, J. A., Pototzky, A. S., and Hoadley, S. T., "Rolling maneuver load alleviation using active controls," *Journal of Aircraft,* Vol. 32, No. 1, 1995, pp. 68-76.

[118] Yurkovich, R. N., "An analysis of the integration of active aeroelastic wing technology into a co-planar variable geometry morphing wing," *Proceedings of 50th AIAA/ASME/ASCE/AHS/ASC Structures, Structural Dynamics and Materials Conference*, Palm Springs, CA, May 4-7, 2009, AIAA-2009-2514.

[119] Zink, P. S., Mavris, D. N., and Raveh, D. E., "Integrated structural/trim optimization for active aeroelastic wing technology," *Proceedings of 8th AIAA AIAA/USAF/NASA/ISSMO Symposium on Multidisciplinary Analysis and Optimization*, Long Beach, CA, Sept. 6-8, 2000, AIAA-2000-4827.

[120] Zink, P. S., Mavris, D. N., Love, M. H., and Karpel, M., "Robust maneuver load alleviation using active control," *Proceedings of 7th AIAA AIAA/USAF/NASA/ISSMO Symposium on Multidisciplinary Analysis and Optimization*, St. Louis, MO, Sept. 2-4, 1998, AIAA-1998-4781.

VITA

Wei-En Li was born in Taipei, Taiwan, on Oct. 9th, 1976. He received his Bachelor's degree in Aerospace Engineering in June 1999 from Tamkang University in Taipei, Taiwan. After spending his wonderful four years there to get his Bachelor's degree, he served in the armed forces of Taiwan. He came to the United States in August of 2002 to start his Master of Science degree in School of Aerospace Engineering at Georgia Institute of Technology and obtained it in May 2004. After one summer away from studies, he resumed his pursuit of the Ph.D. degree and obtained it in August 2009 from the School of Aerospace Engineering at Georgia Institute of Technology. His research work presented here includes the fields of aeroelasticity, structural analysis, computational mechanics, and optimal design.